37
58

THE INVESTIGATION OF THE OPTICAL PROPERTIES OF POLYTYPIC MINERALS

by

Brian J. Cooper

Dissertation submitted to the Faculty of the
Virginia Polytechnic Institute and State University
in partial fulfillment of the requirements for the degree of
DOCTOR OF PHILOSOPHY
in
Geological Sciences

APPROVED:

Paul H. Ribbe, Chairman

Silverio P. Almeida

F. Donald Bloss

James R. Craig

Guy J-M. Indebetouw

April, 1988

Blacksburg, Virginia

THE INVESTIGATION OF THE OPTICAL PROPERTIES OF POLYTYPIC MINERALS

by

Brian J. Cooper

Committee Chairman: Paul H. Ribbe

Geological Sciences

(ABSTRACT)

A new approach to the investigation of the optical properties of polytypic minerals that combines spindle stage techniques, X-ray diffraction methods, electron microprobe analysis, and dielectric tensor calculations has been developed and applied to zinc sulfides and chloritoids.

For the first time, X-ray diffraction studies of natural anisotropic zinc sulfides have documented the simultaneous occurrence of twinning and stacking disorder along more than one of the four symmetry equivalent <111> directions of sphalerite. Precession photographs of optically anisotropic zinc sulfides are characterized by twin-equivalent diffraction maxima and diffuse diffraction streaking along lattice rows with $(h-k) \neq 3n$ (equivalent hexagonal indices) in one or two <111> directions. A system of linear equations has been used to calculate the approximate volume fractions of each twin domain and the sphalerite host domain. Dielectric tensor calculations have been performed to illustrate that mixtures of cubic and hexagonal zinc sulfide may be optically biaxial if the intergrowth occurs along more than one of the

symmetry equivalent <111> directions of sphalerite (cubic).

The dependence of the optical properties upon the chemical variation and polytypic intergrowth in the Mg-Fe chloritoids has been investigated. The effects of the variation in chemical composition of specific polytypic compositions were analyzed first. The refractive indices of 10 approximately pure $2M_2$ Mg-Fe chloritoids show strong correlations ($R^2 \geq 0.094$) to the proportion of Mg cations in the M(1B) site, Mg/(Mg + Fe + Mn) = MGN. Correlations between the optical orientation angles and MGN were weaker ($R^2 \leq 0.87$).

The optical orientation is very sensitive to small variations in the polytypic composition, especially orientation angles that have fixed values in $2M_2$ chloritoid. The parameter showing the most sensitivity is $\angle X \wedge b$, which is 0° in an ideal $2M_2$ chloritoid, but increases to about 6° for a chloritoid containing 10% by volume 1Tc polytype. The sum of $\angle Y \wedge c^*$ and $\angle Z \wedge c^*$ for an ideal $2M_2$ chloritoid has a value of 90°, whereas a chloritoid with 10% 1Tc has a sum of 92°. Although not as sensitive as $\angle X \wedge b$, this parameter can be determined with only a spindle stage or universal stage.

The observed dependence of the optical properties on polytypic intergrowth and chemical variation has been modeled using dielectric tensor calculations based on the properties of a 1Tc layer and assuming that the $2M_2$ polytype is derived by twinning the 1Tc polytype about [010] with an (001) composition plane.

PREFACE

This study was inspired by the work of Hauser and Wenk (1976) on the effects of structural intergrowths in minerals upon the optical properties. Their paper only hints at the wider applications and importance of the concept they developed. This dissertation applies the Hauser and Wenk concept to an investigation of the effects of polytypic intergrowths on the optical properties of polytypic minerals. Polytypic minerals were chosen because the geometrical relationships between polytypes are relatively simple and because polytypic materials are relatively common in nature (e.g. sheet silicates) and some are used in industry (e.g. ZnS and SiC). Hauser and Wenk (1976) used the universal stage to collect their optical data, then mounted crystals for X-ray examination. The most important improvement in data acquisition during the present study involves use of spindle stage techniques (Bloss, 1981) which permit the collection of optical, X-ray, and chemical data from one and the same mineral grain. This greatly improves the confidence level in any correlations that may be found among optical properties and crystal chemical data.

Chapter One presents the groundwork for understanding the concepts and techniques used in this study. The first part introduces the working definition of polytypism and the notation used in reference to polytypes. The second part describes the dielectric tensor and the assumptions made when it is applied to minerals. The last part outlines the data collection methods required for a study of this type. These

same methods may be applied to any type of intergrowth in minerals if the geometric relationships can be well established. This is important because transmission electron microscopy studies have illustrated that many crystals show some type of submicroscopic structural intergrowth. The effects of these structural intergrowths on the optical properties must be understood, because a lack of understanding may lead to an incorrect phase identification or compositional estimate based on the optical properties, or it may be decided that a relationship between the optical properties and the chemical composition is too weak to be useful. For example, Halferdahl (1961) reported that there was a general dependence of the refractive indices of chloritoid on magnesium content, but that the relationship could not be used for determinative purposes. All three chloritoid polytypes plus mixtures were plotted on the same diagram versus magnesium composition. As is shown in this study, the refractive indices are dependent upon polytypic intergrowth. If the refractive indices of a set of chloritoids which all have a specific polytype are plotted according to magnesium content a better correlation obtains.

The original purpose of Chapter Two was to test the dielectric tensor program with a simple intergrowth between CCP ZnS (sphalerite) and HCP ZnS (wurtzite) where the close-packed layers are stacked along a single direction. When it was found that the intergrowth was not always simple, I decided to investigate the effects of these more complicated types of intergrowths on the optical properties of zinc sulfides, too. Chapter Two concentrates on the discovery of this new

type of intergrowth, and presents calculations of the potential effects of these newly discovered intergrowths and simpler intergrowths on the optical properties.

Chapter Three presents a complete application of the methods described in Chapter One to the investigation of the dependence of the optical properties on chemical composition and polytypic intergrowth in Mg-Fe chloritoids. This part of the study exemplifies the power of the spindle stage method, especially for the determination of triclinic optical orientations. The first complete optical orientations of triclinic chloritoids were determined during this study. Although more data are required to establish determinative curves relating the optical properties to chemical and polytypic variations, the procedures and a path towards the establishment of determinative curves have been discovered.

This investigation is an application of a new, exciting approach to mineral optics. I want to apply this approach to other mineral groups, and would like to see other investigators apply these techniques to minerals and synthetic materials. With the increasing use of optics in industry there should be some importance in understanding the effects of structural intergrowths on the optical properties of materials.

Brian Jay Cooper

April 1988

ACKNOWLEDGMENTS

The author wishes to express his gratitude to his major advisor and friend, Dr. P.H. Ribbe, for his guidance through this study. Dr. F.D. Bloss is acknowledged for his constructive criticisms and helpful suggestions, and especially for all that he has done for the advancement of the spindle stage technique. Thanks go to Dr. J.R. Craig, Dr. S.P. Almeida, and Dr. G. J-M. Indebetouw for their constructive criticisms and helpful suggestions concerning this manuscript. Samples for this study were provided by of the Smithsonian; of the American Natural History Museum; and of Virginia Tech. Additional thanks go to and for their help with the electron microprobe; and for their help with the processing of the optical data; of Sam Houston State University for the photographic work; and of College Station, Texas for the drafting of the figures. Without the computer facilities of Virginia Tech and Sam Houston State University this study could never have been done. Therefore, the computer operators and consultants of both schools are also thanked for their many consultations.

Finally, the author wishes to thank his wife, for her understanding and extraordinary patience throughout this study.

TABLE OF CONTENTS

LIST OF TABLES

LIST OF FIGURES

FIGURE Page

CHAPTER ONE

THE INVESTIGATION OF THE OPTICAL PROPERTIES OF POLYTYPIC MINERALS

Introduction

A new approach to the analysis of the optical properties of polytypic minerals has been developed. This is important for the characterization of polytypic materials which are often found in nature and are used in industry.

This approach requires the collection of chemical, X-ray, and optical data from the same grain in order to develop models relating the chemical composition, polytypic intergrowth, and optical properties to each other. The spindle stage techniques developed and described by Bloss (1981) and the physical optics theory described by Hauser and Wenk (1976) have been applied to polytypic minerals to obtain the desired models.

Included in this chapter are the working definition of polytypism and polytypic notation used in this study, a review of dielectric tensors and the assumptions involved with their use in minerals, and a generalized outline of the experimental procedures required for this approach. This chapter can be thought of as a manual for the investigation of the effects of polytypic intergrowth in minerals on their optical properties. The dielectric tensor section and experimental procedures apply to the investigation into the effects of any type of submicroscopic intergrowth on the optical properties of minerals.

Polytypism

Working definition

The phenomenon of polytypism is more common than once believed. This is due to the increased number of investigations of minerals formed in different environments using X-ray diffraction and TEM techniques. The term itself has been redefined to allow more flexibility in its application.

> Polytypism may be regarded as a special case of crystal polymorphism such that various polymorphs (polytypes) may be regarded as arising through different ways of stacking structurally compatible tabular units or polytype modules. Multidirectional stacking of modules along crystallographically equivalent directions may occur, especially if the crystal structure is based upon a cubic close-packed arrangement because of the occurrence of four symmetry-equivalent close-packed stacking directions.

This is Thompson's (1981) definition, except for the last sentence which was added to cover the present study's findings with regard to the zinc sulfides.

Polytypic notation

A complete discussion of the different notations used to designate polytypes is given in Verma and Krishna (1966). Only those notations found useful in this study are described in this section.

The "ABC" notation is useful for describing the stacking sequences in close-packed structures such as the zinc sulfides. The "A" represents a close-packed layer of ions or atoms with two sets of interstices. The "B" close-packed layer "covers" one set of interstices, and the "C" close-packed layer "covers" the other set of interstices. In a three-dimensional close-packed structure, no two adjacent layers have the same letter. The letters refer to individual close-packed layers of atoms or ions in the original usage of this notation, although some authors use this notation in reference to "polyatomic" layers. For example, each letter may specify a close-packed layer of Zn-S dipoles in the zinc sulfides. Cubic close packing (CCP) is represented by ...ABCABC..., and hexagonal close packing (HCP) by ...ABABAB.... the Ramsdell (1947) zigzag sequence is a pictorial representation of the "ABC" notation (Fig. 2-1, p.22).

The notation used by Pauling (1945), Wyckoff (1948), and Jagodzinski (1949) describes each close-packed layer in terms of the orientation of the adjacent layers. a close-packed layer having identical layers on either side of it is designated by "h" since this

arrangement is characteristic of hexagonal close packing:

...ABABAB...

....hhhh....

A close-packed layer having different layers on either side of it is designated by "c" or "k" (German) because this arrangement is characteristic of cubic (Kubik or kubische) close packing:

...ABCABC...

....kkkk....

This notation was necessary to derive the equations used to calculate the volume fractions in the case of multidirectional stacking disorder, and to understand the relationship between twinning in cubic close-packed domains and the amount of hexagonal close-packed domains produced by the twinning.

The Ramsdell (1947) notation and modified Gard notation (Bailey, 1977) are useful when referring to entire unit cells because the number of unit-modules in the unit cell and the symmetry of the unit cell are stated in the symbol. The Ramsdell notation is useful for the zinc sulfides in referring to the ordered polytypes. For example, cubic close-packed sphalerite is the 3C polytype while 2H is the symbol of wurtzite, the hexagonally close-packed polytype. The chloritoid polytypes are often denoted by the same symbolism used for the micas. Triclinic chloritoid is 1Tc, and the two monoclinic polytypes are $2M_1$ and $2M_2$. The modified Gard notation for these would be Aabc (A = anorthic = triclinic), Mba2c, and Mab2c, respectively (assuming the 2M chloritoid in Table 1 of Bailey (1977) refers to the most common

polytype, $2M_2$). The modified Gard notation gives one an immediate understanding of the crystallographic relationships between the respective polytypes. The Ramsdell symbols and Gard notations are useful when referring to the basic modules of minerals like chloritoids because the modules are polyatomic layers which are not treated in terms of close packing.

Physical Optics

To model and analyze the optical properties of polytypic minerals requires the use of physical optics. Geometrical optics is limited to describing the interaction of light with domains larger than the wavelength of light, whereas physical optics can be used to describe the interaction of light with domains as small or smaller than a unit cell. The latter case is most appropriate for the treatment of the optical properties of polytypic intergrowths where at least one dimension of the "unit" polytypic module is much less than the wavelength of visible light (approximately two orders of magnitude smaller).

The optical properties to be considered in this study are those characteristic of the optical indicatrix. If submicroscopic module types are uniformly distributed within the composite grain, then a single optical indicatrix will describe the homogeneous optical properties of the composite grain. Unfortunately, the spatial average of the indicatrices is not the spatial average of the parameters of the indicatrix. This is where physical optics is applied. The optical

indicatrix and its orientation relative to the crystal structure can be expressed in terms of a dielectric tensor. If the dielectric tensor of each module type is multiplied by the volume fraction of that module type, then the dielectric tensor representing the composite optical indicatrix will be the sum of these products. Before going any further, it is necessary to review the derivation given in Hauser and Wenk (1976) to illustrate the "hows" and "whys" of this approach.

The derivation first assumes that the material is a dielectric. Even though minerals are not perfect dielectrics, most silicates and even the zinc sulfides have conductivities that are low enough that their properties may be described in terms of dielectrics.

Electric charges do not move freely through dielectrics but may be displaced relative to each other when an electrical field is applied. The displacement produced by the applied electric field is a function of the binding energy between the electrons and the nucleus which in turn depends on the internal structure of the dielectric. For an anisotropic mineral this is expressed as

$$\mathbf{P} = \chi\mathbf{E}, \qquad (1\text{-}1)$$

where **P** is the polarization which is defined as the vector sum of the dipole moments per unit volume, χ is the electric susceptibility tensor of the mineral, and **E** is the macroscopic electric field strength which is the volume average of the microscopic electric field strengths.

The electric displacement vector, **D**, is defined as:

$$\mathbf{D} = \mathbf{E} + 4\pi\mathbf{P}, \qquad (1\text{-}2)$$

assuming the Gaussian system of units.

Substituting (1-1) into (1-2) gives the following expression:

$$D = (I + 4\pi\chi)E, \tag{1-3}$$

where I is the identity tensor. The dielectric tensor, ε , is defined as

$$\varepsilon = I + 4\pi\chi, \tag{1-4}$$

so that (1-3) can be written as

$$D = \varepsilon E. \tag{1-5}$$

Any tensor which describes a physical property has an associated three-dimensional surface called the representation quadric. The representation quadric of the inverse of the dielectric tensor, ε^{-1} , is equivalent to the optical indicatrix. Therefore, the eigenvectors of ε correspond to the principal directions of the optical indicatrix, and the eigenvalues of ε correspond to the principal refractive indices squared.

The derivation of the expression for dielectric tensors of composite grains requires returning to Equation (1-1). A small volume element of a grain consisting of two module types will be considered first. Monochromatic light is assumed so as to eliminate the additional complexities of including dispersion in the derivation. The two module types occur as two lamellae that are thinner than the wavelength of light so that the volume element is optically homogeneous. The lamellae must also be thicker than a unit cell in order to avoid consideration of the individual atomic electric fields.

Light passing through the volume element will produce a macroscopic electric field in each module. The two fields, E_1 and E_2, differ

because of the surface charge density, σ , induced at the interface. Therefore,

$$E_2 = E_1 + 4\pi\sigma N, \tag{1-6}$$

where N is a unit vector normal to the interface. Hauser and Wenk (1976) temporarily ignore the surface charge density so that

$$E_1 = E_2 = E. \tag{1-7}$$

The polarization within the two modules is written as

$$P_1 = \chi_1 E_1 \quad \text{and} \quad P_2 = \chi_2 E_2 \ . \tag{1-8}$$

The macroscopic electric field strength and the polarization of the entire volume element are obtained by calculating the volume average:

$$E = f_1 E_1 + f_2 E_2, \tag{1-9}$$

$$P = f_1 P_1 + f_2 P_2, \tag{1-10}$$

where $f_1 = \Delta V_1/\Delta V$ and $f_2 = \Delta V_2/\Delta V$, and where ΔV, ΔV_1 and ΔV_2 represent the volumes of the volume element and the two lamellae, respectively. Note that

$$\Delta V_1 + \Delta V_2 = \Delta V \tag{1-11}$$

so that

$$f_1 + f_2 = 1 \ . \tag{1-12}$$

Considering Equation (1-7) and substituting Equations (1-8) into Equation (1-10) gives

$$P = (f_1\chi_1 + f_2\chi_2)E \ . \tag{1-13}$$

Therefore, the electric susceptibility tensor of the volume element can be written as

$$\chi = f_1\chi_1 + f_2\chi_2 \ , \tag{1-14}$$

and with substitutions based on Equation (1-4), the dielectric tensor of

the volume element is

$$\varepsilon = f_1\varepsilon_1 + f_2\varepsilon_2 \quad . \tag{1-15}$$

This equation can be generalized for any number of module types n so that

$$\langle\varepsilon\rangle = \sum_{i=1}^{n} f_i\varepsilon_i \quad , \tag{1-16}$$

where $\langle\varepsilon\rangle$ indicates that this sum is an approximate dielectric tensor because the surface charge density has been ignored. However, Hauser and Wenk (1976) describe an extensive derivation of an "error approximation" which indicates that the differences between the values obtained by this approximation and those values obtained by the "exact" tensor are "second order." The derivation of the error approximation was repeated for each of the minerals used in this study, assuming that

$$\mathbf{N} = \begin{bmatrix} 0 \\ 0 \\ 1 \end{bmatrix} \tag{1-17}$$

for the basis used in each coordinate system. The equation for the approximation of the error derived for the two-lamellae case is

$$\frac{f_1 f_2(\varepsilon_{331} - \varepsilon_{332})^2}{(f_1\varepsilon_{331} + f_2\varepsilon_{332})} \quad , \tag{1-18}$$

where ε_{331} and ε_{332} are the ε_{33} components of ε_1 and ε_2, respectively. As stated by Hauser and Wenk, the maximum value occurs when f_1 and f_2 = 0.5. The maximum value obtained in this study was 0.0002 in the maximum refractive index, well within the precision attained during this study.

Polytypic intergrowths tend to be in good agreement with the assumptions being made about the shape and size of the modules. Each polytypic layer is tabular, and generally thinner than wavelengths of

visible light and larger than a single unit cell. Since the chemical compositions and crystal structures of the different modules are nearly identical, the macroscopic electric fields produced in the modules would be nearly equal. Therefore, it seems that the approximation given by Equation (1-16) is a reasonable one to use in the modeling of the optical properties of polytypic minerals.

Hauser and Wenk (1976) also demonstrated that Equation (1-16) can be used to model some solid solutions. In this case solid solutions are viewed as composite materials where the modules are unit cells having different chemical compositions. The following assumptions are made:

1. "...lattice strain caused by atomic substitution may be negligible..."
2. "...all atoms must have cubic site symmetry."
3. The dielectric tensors of the end members differ only slightly.

The optical properties of the Mg-Fe join of the chloritoids are modeled in this way. The substitution of ions of similar size and chemical properties in the chloritoids is assumed to cause only minor distortions. Chloritoid's approximately close packed structure has nearly cubic site symmetry. The dielectric tensors of the end members differ only by differences in the refractive indices (~0.01 for the range of compositions used).

Computer Program and Required Input

The dielectric calculations were performed by a computer program coded by Hauser and Wenk with only minor modification by this author. The listing of the program, a description of the calculations performed by the program, a sample input file, and a sample output file are contained in Appendix A.

The program requires stereographic coordinates and refractive indices for each principal direction of the indicatrices of every module type in the composite grain. These data are used to calculate the dielectric tensors of the module types by forming the eigenvalues and eigenvectors of each module type. The volume fractions are also part of the input data so that Equation (1-16) can be used to calculate the approximate dielectric tensor of the composite grain. The program then calculates the eigenvalues and eigenvectors of the composite dielectric tensor to obtain the coordinates of the principal vibration directions and refractive indices of the composite grain. Other optical properties such as the optic axial angle and birefringence can then be calculated for the composite grain.

Experimental Procedures

The procedures described in this section are generalized, but demonstrate the techniques used to obtain the data required for an analysis of the optical properties of polytypic minerals, or other types

of intergrowths.

Optical procedures

The spindle stage methods developed and described by Bloss (1981) are used to characterize the optical indicatrix of each sample. This includes the location of the principal vibration directions, the determination of the optic axial angle, and the measurement of the principal refractive indices. Since all measurements are made at each of at least three different wavelengths, the effects of dispersion are also characterized. The primary advantage of using the spindle stage techniques developed by Bloss and co-workers is the ability to obtain all the optical, X-ray, and chemical data from a single grain. This ability gives credence to correlations made between optical properties and either the structural parameters or the chemical composition. The determination of the optical orientations of monoclinic and triclinic minerals becomes a comparatively simple task.

Extinction data are collected first for the purpose of locating the principal vibration directions and determining the optic axial angle. The "360° option" was used during this study. Extinction positions were determined with a Nakamura plate, a type of half-shade accessory requiring the use of a cap analyzer. The Nakamura plate works extremely well, with good reproducibility of extinction positions except at positions exhibiting very low birefringence. The Nakamura plate is recommended for measurement of grains containing birefringent inclusions

because these produce erroneous extinction positions when the grain is measured with a photometer. The EXCALIBR computer program described in Bloss (1981) was used to determine the coordinates of the principal vibration directions and the value of the optic axial angle from the extinction data. These calculations are performed at each wavelength, and subroutine DISPER evaluates the dispersion of the principal directions and optic axial angle.

In preparation for the measurement of the refractive indices, it is necessary to use the calibration and standardization procedures and computer programs described by Su, Bloss, and Gunter (1987).

All of the refractive index oils used in this study were measured with a Bellingham and Stanley "Abbe 60" refractometer, the temperature of which was controlled by circulating water flow. A thermocouple was used to measure the temperature of the oil between the prisms. The measurements were made using spectral lamp light sources having the following wavelengths: 434.84 nm, 546.07 nm, 589.60 nm, and 643.85 nm.

A glass standard was chosen within the range of the refractive indices being measured in order to evaluate observer and system error. The refractive index of the glass standard was previously determined using the minimum deviation method at six wavelengths. These refractive indices were assumed to be correct and were used to calculate the "true" Cauchy constants and linearized Sellmeier constants for the glass standard. Next, the refractive index of the glass standard was determined using the double-variation method and the calibrated oils. The computer program GLASS was used to calculate the linearized

Sellmeier constants of the glass standard based on the double-variation data. Su (personal communication, 1985) now uses the program SOLID for this step.

The refractive indices of the mineral samples can be determined by orienting each principal vibration direction parallel to the polarizer using the spindle stage coordinates determined by EXCALIBR. At each setting the grain is compared to at least three of the calibrated oils using the double-variation method. A set of temperatures and wavelengths collected for each principal vibration direction is placed in SOLID which then calculates the linearized Sellmeier constants for each direction. The refractive indices at specific wavelengths are included in the output.

X-ray procedures

Upon completion of the optical procedures the entire goniometer-head/sample assemblage is transferred to a precession camera for X-ray study. The grain is examined by X-ray photographic techniques to determine:

1. the location of the crystallographic directions;
2. the geometric relationship and distribution of the polytypic intergrowths; and
3. the approximate volume fraction of each module-type in the composite grain.

The precession method was used because the reciprocal lattice is recorded in an undistorted form, and all the desired orientations could be obtained without remounting grains.

The angle between each crystallographic direction and the dial axis is measured on the X-ray photograph. These angles and the dial axis settings can be converted to spindle stage coordinates, assuming that the correspondence between dial axis settings and spindle axis setting have been determined. The spindle stage coordinates of the crystallographic directions and of the principal vibration direction can be used to calculate the angles between the two sets of directions to specify the optical orientation.

The diffraction patterns are studied carefully to determine what types of intergrowths are present within the grain. The diffraction pattern is usually dominated by diffraction maxima of the host polytype. Fainter diffraction maxima may indicate a different polytype or twinning. Diffuse diffraction streaking along reciprocal lattice rows parallel to specific directions is indicative of stacking disorder along those directions. In some instances two or more unique sets of diffraction maxima and diffuse diffraction streaks have been observed.

Densitometry can be used to obtain approximate intensities required to estimate the volume fractions of each module type. If polytypic intergrowth occurs along only one direction, then there will be some diffraction maxima that are contributed to by all module types. The volume fractions are found by calculating the ratio of the intensity of a reflection due to part of the composite grain to the intensity of a

reflection due to the whole composite grain. Multidirectional stacking of module types is more complex and therefore requires a system of linear equations to determine the volume fractions from the intensity data. Appendix B presents a derivation of the equations for zinc sulfides exhibiting twinning along four symmetry-equivalent directions.

Chemical analyses

Chemical compositional data must be obtained since most mineral groups will have at least some variation in the optical properties due to chemical substitution. The chemical analysis has to be nondestructive. During this study, the samples were analyzed with an automated electron microprobe prior to the final optical and X-ray examination. The samples could have been analyzed after the optical and X-ray data were collected, but this step was considered risky in terms of sample preservation.

The chemical dependence of the optical properties may be difficult to determine, and perhaps impossible at this time if there are large numbers of chemical substituents. As mentioned earlier, the Hauser and Wenk computer program can be used to model the effects of chemical substitution on the optical properties. Such a model would require the assumption of solid solution between end members with previously determined optical properties.

Summary

A new approach capable of giving insight into the effects of polytypic intergrowth on the optical properties of polytypically intergrown minerals has been presented in this chapter. This approach requires knowledge of the optical properties of the individual module types, as well as the observed optical properties of several composite grains having a range of polytypic compositions. This "knowledge" is obtainable using the spindle stage techniques described by Bloss (1981). X-ray and chemical data are also required for this approach. The dielectric tensor calculations described by Hauser and Wenk (1976) are used to aid in the development of models relating the chemical composition, polytypic composition and optical properties to each other. Several assumptions must be made when using the dielectric tensor calculations. Many silicate and oxide systems should be able to satisfy these assumptions. If this new tool is used in conjunction with experimental studies, useful information about the origin of various types of polytypic intergrowths may be obtained.

The procedures presented in this chapter may also be applied to many other types of intergrowths so long as the basic assumptions are satisfied.

CHAPTER TWO

MULTIDIRECTIONAL TWINNING AND STACKING DISORDER IN NATURAL ANISOTROPIC ZINC SULFIDES

Introduction

For the first time, X-ray diffraction studies of natural anisotropic zinc sulfides have documented the simultaneous occurrence of twinning and stacking disorder (TSD) along more than one of the four symmetry equivalent <111> directions or close-packing directions of sphalerite. To demonstrate the significance of this discovery a brief review of zinc sulfide crystal structures and possible causes of TSD will follow.

Crystal structures of zinc sulfides

The crystal structures of the ZnS polytypes, sphalerite and wurtzite, are based on interpenetrating close-packed arrays of sulfur and zinc atoms. It is more convenient to view the structures as close-packed arrays of monolayers of Zn-S dipoles, where successive close-packed monolayers are designated by A, B, or C, depending on their relative location in the stacking sequence. Sphalerite has the cubic close-packed 3C (3 layers in the repeat cell; C=cubic) structure symbolized by the stacking sequence ...ABCABCABC..., with close-packed stacking directions parallel to each of the four symmetry-equivalent <111> directions. Wurtzite has the hexagonal close-packed 2H (2 layers

in the repeat cell; H=hexagonal) structure, ...ABABAB..., with only one close-packed stacking direction parallel to [0001]. The Ramsdell (1947) zigzag representations for each structure are illustrated in Figure 2-1.

Causes of twinning and stacking disorder

The number of distinct stacking sequences between the 3C and 2H "end members" is unlimited. Some sequences are ordered and thus are valid ZnS polytypes, but most are partially disordered or totally disordered. A variety of stacking sequences may be produced during paragenetic events such as crystal growth and chemical substitution, phase transition upon cooling or heating, and mechanical deformation.

Growth defects in zinc sulfides cause twinning and some stacking disorder (Geilikman, 1982). A structural defect may be introduced by the "accidental" omission of an atom during growth or by an impurity such as Cd or Fe. For example, in ZnS Cd stabilizes the hexagonal structure because pure CdS is hexagonal under upper crustal conditions (Geilikman, 1982). The orientation of TSD depends on the conditions during crystal growth. The TSD may occur along a single [111] direction as observed in the sphalerites of the deposit at Elmwood-Gordonsville, Tennessee (Seal et al., 1985), or it may occur along two, three, or all four of the possible <111> directions. It is likely that the TSD would occur along just one direction within any single submicroscopic domain or "block", but in terms of a composite grain (not a true "single crystal") the stacking vectors of the small domains would be parallel to

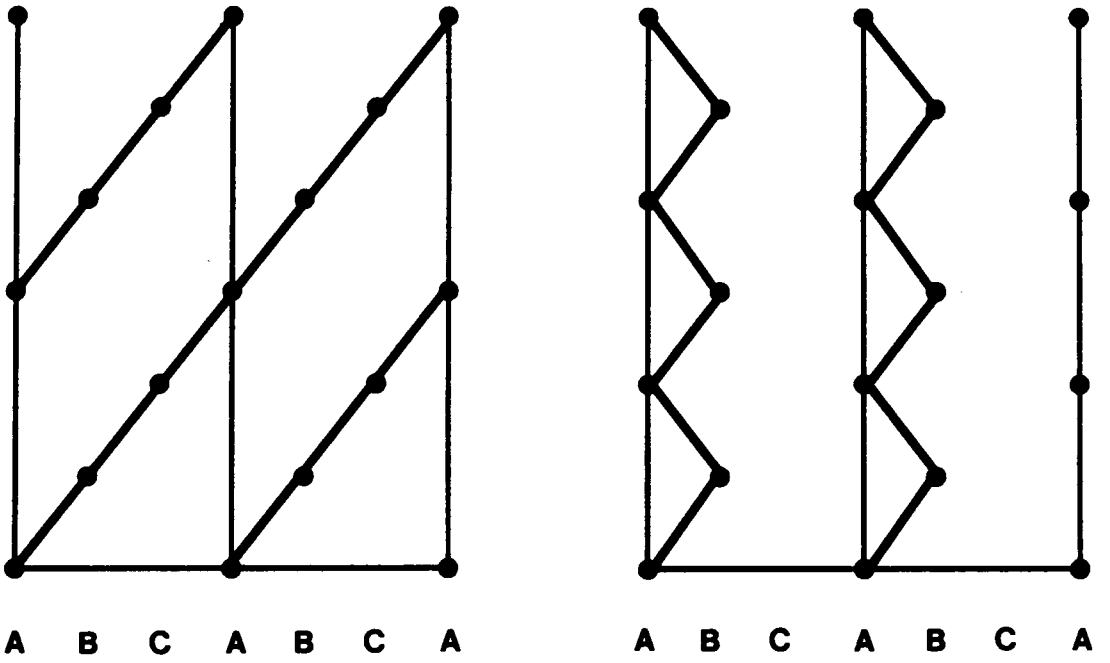

Fig. 2-1. Ramsdell (1947) zigzag representations of the stacking sequences in 3C and 2H zinc sulfides. A, B, and C indicate the close-packed stacking positions; the dots represent individual Zn-S dipoles. The hexagonal [0001] or cubic [111] is vertical.

one of the four <111> directions of the sphalerite host.

Both the 2H→3C and the 3C→2H phase transitions have been investigated by Akizuki (1970, 1981, 1983) and Fleet (1977a, 1977b, 1983). The 2H→3C phase transition produces stacking disorder along a single direction corresponding to the [0001] direction of wurtzite and a <111> direction in each of the 3C domains. Since the phase transition may have started at several points within the crystal at one time, the 3C domains may occur in two crystallographically distinct orientations. The two twin-related 3C orientations within the 2H host domain are thought to occur in approximately equal proportions (M.E. Fleet, personal communication, 1984), which is logical because of the 50% probability for the occurrence of each orientation. The 3C→2H phase transition produces stacking disorder along one of the <111> directions of sphalerite by gliding along one of the four {111} planes (Akizuki, 1970). Akizuki (1970) also found that gliding continued until terminated by other {111} "slip" planes, creating a composite crystal made up of many blocks. Akizuki (1970, 1981) states that the orientation of the gliding in each block is dependent on "local thermal stresses" and is independent of "pre-existing stacking faults, dislocations, or other defects". Therefore, the stacking vector of each of the many blocks in the composite crystal could be oriented along any of the four <111> directions of the sphalerite host.

Mechanical deformation of sphalerite causes twin gliding to occur along the {111} planes within sphalerite, creating submicroscopic 2H domains parallel to the glide plane or deformation fault. This is

illustrated in Figure 2-2. Fleet (1977b) suggested that deformation faults originate the twinning along a single <111> direction observed in a sphalerite from Austinville, Virginia. It seems reasonable that the twinning and attendant stacking disorder may occur along one, two, three, or four <111> directions simultaneously, if the gliding begins at several points within the sphalerite and along different {111} planes.

Therefore, TSD along one, two, three, or four <111> directions of a host sphalerite could possibly occur due to growth defects, the 3C→2H phase transition, or mechanical deformation. The 2H→3C phase transition would probably produce TSD along a single direction parallel to the [0001] direction of the original wurtzite crystal.

Optical anisotropy in zinc sulfides

Twinning and stacking disorder in sphalerite produce optically anisotropic domains such as the 2H domains parallel to glide planes created by mechanical deformation. Anisotropy in zinc sulfides has been mentioned in the literature, but not as often as it would have been if transmitted light microscopy was commonly used in the study of sulfide ore deposits (Lindblom, 1980). Textures ranging from alternating anisotropic and isotropic bands to patchy "cross-hatched" patterns and intersecting anisotropic lamellae have been reported (Akizuki, 1970, 1981; Fleet, 1977a, 1977b; Lindblom, 1980; Roedder, 1968a, 1968b; Seal et al., 1985). Previous studies have shown an approximately linear

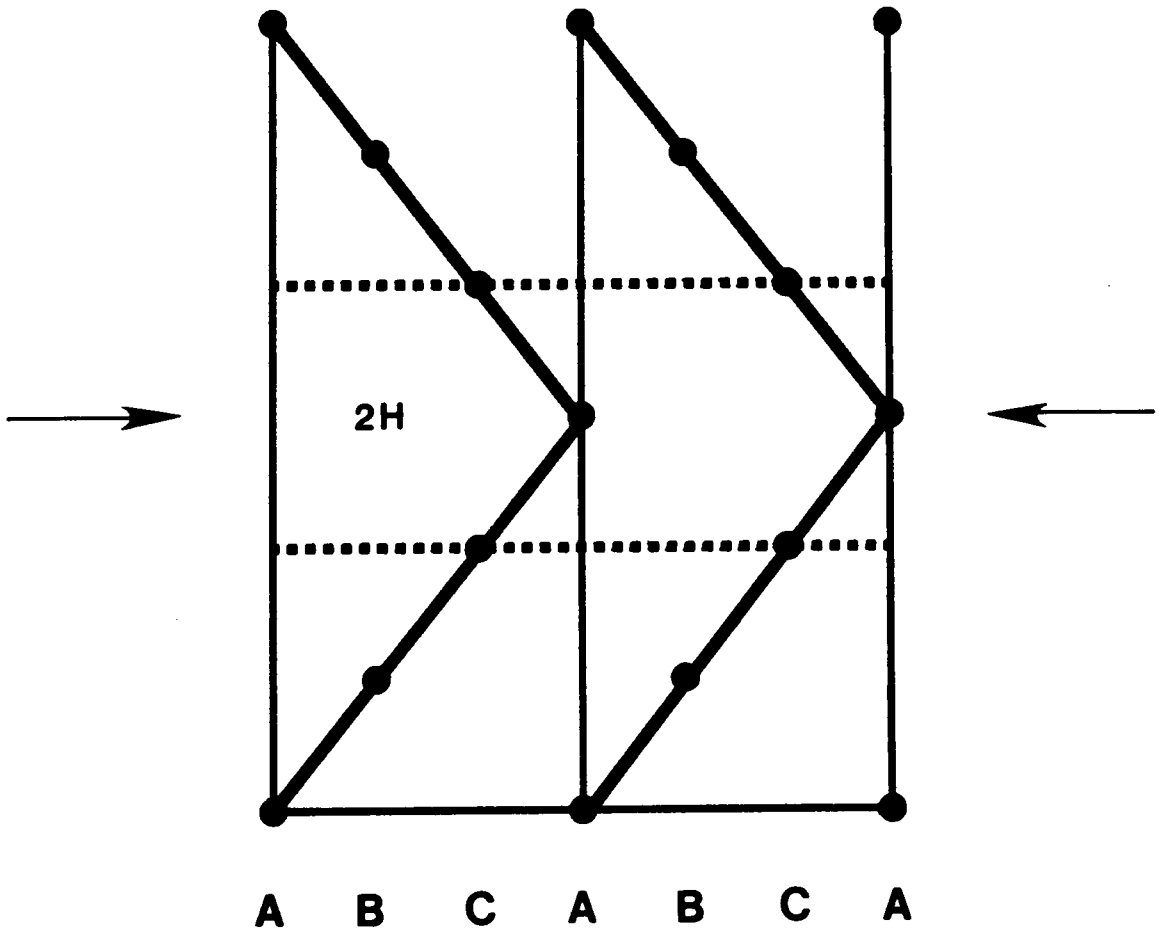

Fig. 2-2. Ramsdell (1947) zigzag representation showing the twinning caused by gliding along a {111} plane in sphalerite. The arrows indicate the position of the composition plane. A 2H layer ("CAC") occurs between the two dashed lines. The hexagonal [0001] or cubic [111] is vertical.

relationship between maximum birefringence (δ) and volume fraction of hexagonal close-packed layers (σ),

$$\delta = \delta_{2H} \times \sigma,$$

where δ_{2H} is the maximum birefringence of pure wurtzite (Nelkowski and Pfützen-Reuter, 1971; Fleet, 1977a). This linear relationship is confirmed by dielectric tensor calculations during this study using the computer program coded by Hauser and Wenk (1976)(see Appendix A) and assuming 2H-3C intergrowth along only one direction. Fleet (1977a) suggested that the relationship among σ and δ may be polynomial because δ is often lower than expected based on the linear equation above (Figure 2-3). He attributed this to error in birefringence determination, in that the maximum possible value was not actually measured. Compositional effects were ruled out on the basis that δ is relatively independent of chemical substitution (Fleet, 1977a; Hurlbut, 1957). Another possible explanation involves TSD along one, two, three, or four <111> directions of a sphalerite host grain. Dielectric tensor calculations predict that such zinc sulfides would be biaxial in some cases and would have lower δ values than would be expected for the given σ values.

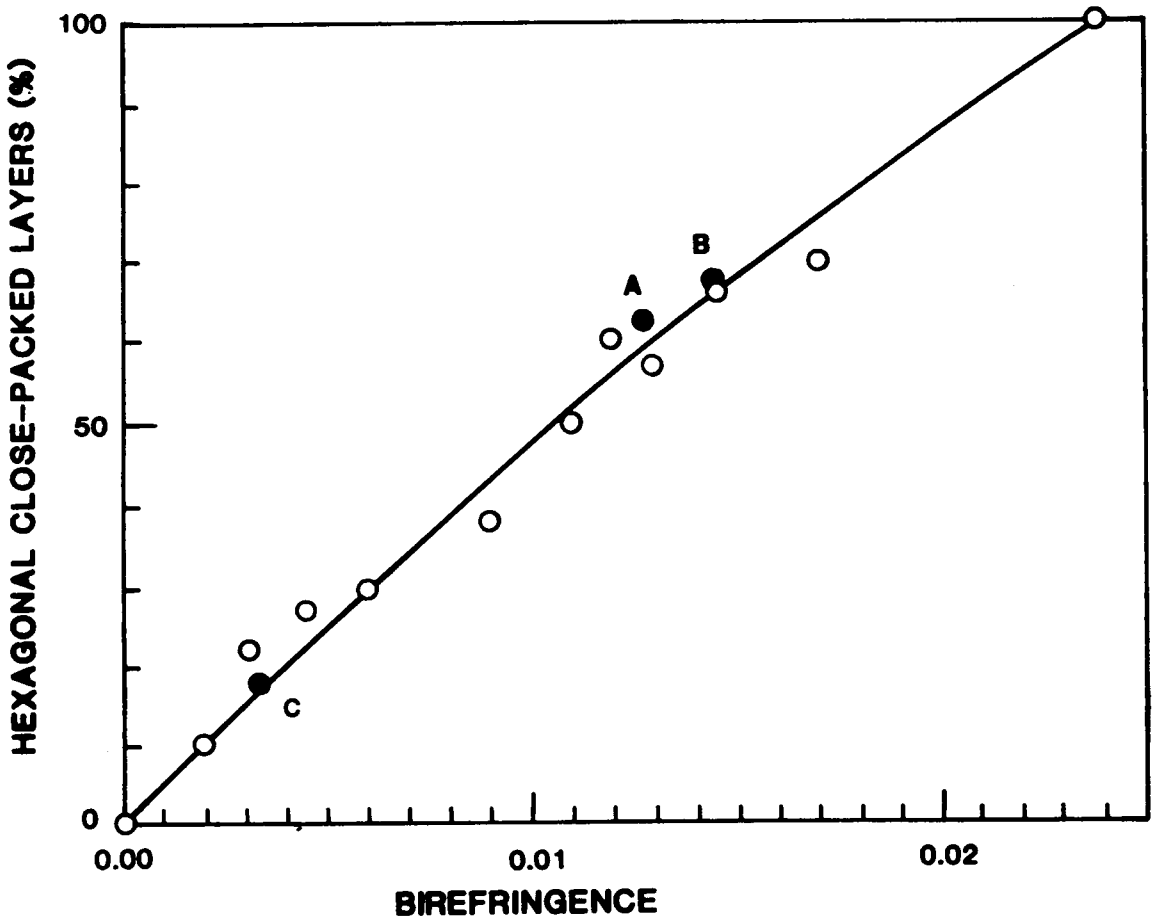

Fig. 2-3. The relationship between the percentage of hexagonal close-packed layers (σ) and the birefringence (δ) for synthetic zinc sulfides (open circles, Nelkowski and Pftuzen-Reuter, 1971) and for natural zinc sulfides (full circles, Fleet, 1977). A and B are disordered 2H wurtzite from Pribram and C is disordered 3C sphalerite from Thomaston Dam (Fleet, 1977). After Fleet (1977).

Purpose

In this chapter, X-ray diffraction methods are used to demonstrate the existence of multidirectional twinning and stacking disorder in zinc sulfides. The potential effects of TSD on the maximum birefringence of anisotropic zinc sulfides are analyzed using dielectric tensor calculations.

Experimental Procedures

Electron microprobe analysis

The zinc sulfides used in this study are listed in Table 2-1. Several grains of each sample were chosen for electron microprobe analysis, their maximum dimension being 0.5 mm or less. Each collection of grains was mounted on a one-inch glass disk using Crystal-Bond as the adhesive. The mounts were ground and polished to produce a smooth surface on as many of the grains as possible without loosing any grains; they were then carbon-coated. (Note: later attempts to vacuum-evaporate a carbon-coating on samples mounted in Crystal-Bond resulted in bubbling and partial vaporization of the Crystal-Bond.)

The analyses were performed with an automated, nine-spectrometer ARL-SEMQ electron microprobe at an operating voltage of 20kV. The standards were synthetic compounds, listed below with the elements

Table 2-1. Zinc sulfide analysis numbers, reference numbers, and localities

Analysis number	Reference number	Locality
1	SPH-I	Austinville, Virginia
2	SPH-II	Austinville, Virginia
3	640-3*	Austinville, Virginia
4	11-10-17*	Austinville, Virginia
5	USNM 113943	Casapedia, Quebec
6	G-4**	Elmwood-Gordonsville, Tennessee
7	USNM 97342	Franklin, New Jersey
8	USNM C419	Schemnitz, Czechoslovakia
9	USNM B1353	Sonora, Mexico
10	USNM 80746	Pribram, Czechoslovakia
11	USNM 135612	Synthetic
12	ThD#	Thomaston Dam, Connecticut

Note: USNM refers to the United States National Museum; samples provided by John S. White.

* Samples provided by N. Foley.

** Sample provided by R. Seal.

\# Sample provided by W. Henderson.

analyzed for, and X-ray line used for each element:

ZnS	ZnKα	SKα
FeS	FeKα	
CdS	CdLα	
HgS	HgMα	
MnSe	MnKα	SeKα

Multiple analyses were performed on each grain, with the intent of analyzing areas of varying anisotropy. This resulted in a total of 7 to 19 analyses per sample. The data were reduced on-line by the MAGIC IV program (Colby, 1971).

X-ray diffraction techniques

Cleavage fragments were removed from the Crystal-Bond with acetone. These grains were then attached to glass fibers in preparation for single-crystal X-ray precession photography. The fragments were mounted with a [111] or [100] direction parallel to the dial axis, and [$\bar{1}$10] as precession axis. Fragments mounted parallel to [111] had to be rotated +120° and -120° on the dial from the initial setting in order to obtain three photographs showing all four <111> directions. Those mounted parallel to [100] required two photographs 90° from each other. Exposure times ranged from 41 to 285 hours per photograph, using Ni-filtered CuKα or Zr-filtered MoKα radiation. The long exposure times

were needed in order to observe weak twin reflections and diffraction streaks along reciprocal lattice rows with h-k ≠ 3n (equivalent hexagonal indices). The CuKα photographs were preferred due to greater intensity and resolution.

A Helena Laboratories "Quick Scan" scanning densitometer was used to obtain relative intensity data. Scans were run along white radiation streaks and through diffraction maxima associated with each of the symmetry-equivalent and twin-equivalent 111 reflections. Scans were also run along lattice rows with h-k ≠ 3n (equivalent hexagonal indices) parallel to the <111> directions on each photograph showing evidence of TSD in both directions.

Optical measurements

The goniometer heads and attached samples were subsequently transferred to a spindle stage on an Ortholux polarizing transmitted light microscope (E. Leitz, Wetzlar, W. Germany). The maximum retardations were measured with a Berek compensator (E. Leitz). Grain thickness was measured perpendicular to the orientation of the maximum retardation with a Vicker's Image Splitting Eyepiece. None of the grains were suitable for examination using the extinction methods of Bloss (1981). Three problems were encountered. First, some of the grains were not homogeneous on a microscopic scale. Second, some grains would not go extinct, even though they appeared to be optically homogeneous. Third, a few of the grains were either too darkly colored

or the retardation was too low to obtain reproducible extinction readings.

Results and Discussion

The chemical analyses, cation proportions, the calculated cell-edge based on chemical composition (Scott, 1974), and the number of twin axes are compiled for each specimen in Table 2-2.

The only significant substituents for Zn in the natural samples are Cd (up to 0.6%) and Fe (up to 9.7%). An attempt to determine the effect of Cd substitution on the optical properties was made using the Hauser and Wenk program and assuming the refractive indices given by Hurlbut (1957). The only changes observed were in the fifth decimal place of the calculated value of the maximum birefringence. Necessary data to determine the effects of Fe substitution were not available.

X-ray diffraction data

Precession photographs ranged from an untwinned sphalerite diffraction pattern (Figures 2-4 and 2-5) to patterns displaying twin-equivalent 111 diffraction maxima, and various amounts of diffuse diffraction streaking and peak broadening along reciprocal lattice rows with $h-k \neq 3n$ (equivalent hexagonal indices) in one or two directions (Figures 2-6 through 2-10). Figure 2-6 is an idealized illustration of the twinning relationships. Samples 3, 6, and 14 show twin-equivalent

Table 2-2. Microprobe analyses, cation proportions, and X-ray data for the zinc sulfides listed in Table 2-1

Analysis number	1	2	3	4	5	6
Zn (wt%)	67.2 (4)	67.2 (4)	66.4 (4)	67.7 (4)	67.2 (4)	n.a.
Fe	0.35(3)	0.35(3)	0.36(3)	0.06(2)	0.28(3)	n.a.
Cd	0.25(4)	0.25(4)	0.30(4)	0.29(4)	0.39(4)	n.a.
S	32.3 (3)	32.3 (3)	32.9 (3)	32.0 (3)	32.1 (3)	n.a.
Total	100.1 (8)	100.1 (8)	100.0 (8)	100.1 (8)	100.0 (8)	n.a.
			Cation proportions			
Zn	0.99 (1)	0.99 (1)	0.99 (1)	1.00 (1)	0.99 (1)	0.987*
Fe	0.0060(1)	0.0060(1)	0.0063(1)	0.0019(3)	0.0049(5)	0.009
Cd	0.0021(4)	0.0021(4)	0.0026(4)	0.0025(4)	0.0033(4)	0.004
			X-ray data			
a_c § (Å)	5.410	5.410	5.410	5.410	5.410	5.410**
Twin axes	3	4	2	0	1	1

Note: Values in parentheses represent esd's for last decimal place.

* Cation proportions provided by J.R. Craig

§ Calculated using the Scott (1974) equation

** Values of 5.411 Å and 5.415 Å were obtained by R. Seal using powder diffraction with an internal standard

Table 2-2. Continued

Analysis number	7	8	9	10	11	12
Zn (wt.%)	66.7 (4)	66.9 (4)	67.7 (4)	64.9 (4)	67.8 (4)	61.7 (4)
Fe	0.26(3)	0.12(2)	0.18(2)	2.15(6)	0.01(2)	5.70(9)
Cd	0.22(4)	0.50(4)	0.30(4)	0.71(5)	---	0.09(4)
S	32.9 (3)	32.5 (3)	31.8 (3)	32.2 (3)	32.2 (3)	32.5 (3)
Total	100.1 (8)	100.0 (8)	100.0 (8)	100.0 (8)	100.0 (8)	100.0 (8)
			Cation proportions			
Zn	0.99 (1)	0.99 (1)	0.99 (1)	0.96 (1)	1.00 (1)	0.90 (1)
Fe	0.0044(5)	0.0021(4)	0.0031(4)	0.037 (1)	0.0001(3)	0.097 (2)
Cd	0.0019(3)	0.0043(4)	0.0025(4)	0.0061(5)	---	0.0008(3)
			X-ray data			
a_c [§] (Å)	5.410	5.410	5.410	5.412	5.409	5.412
Twin axes	0	1	0	2	1	1

Note: Values in parentheses represent esd's for last decimal place.

§ Calculated using the Scott (1974) equation

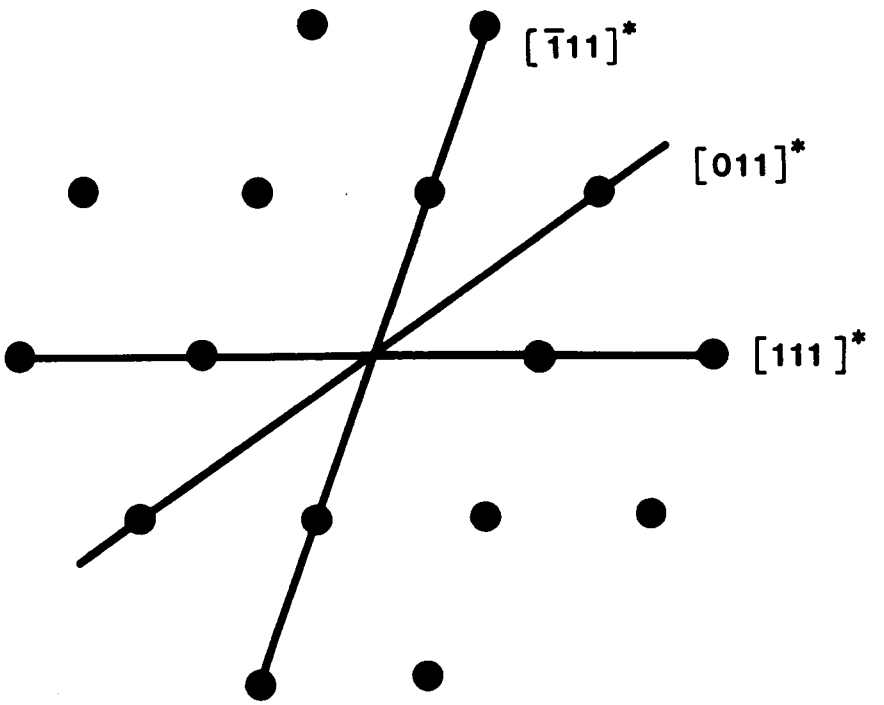

Fig. 2-4. A schematic precession diffraction pattern of an ideal sphalerite showing no sign of twinning. The precession axis is [011].

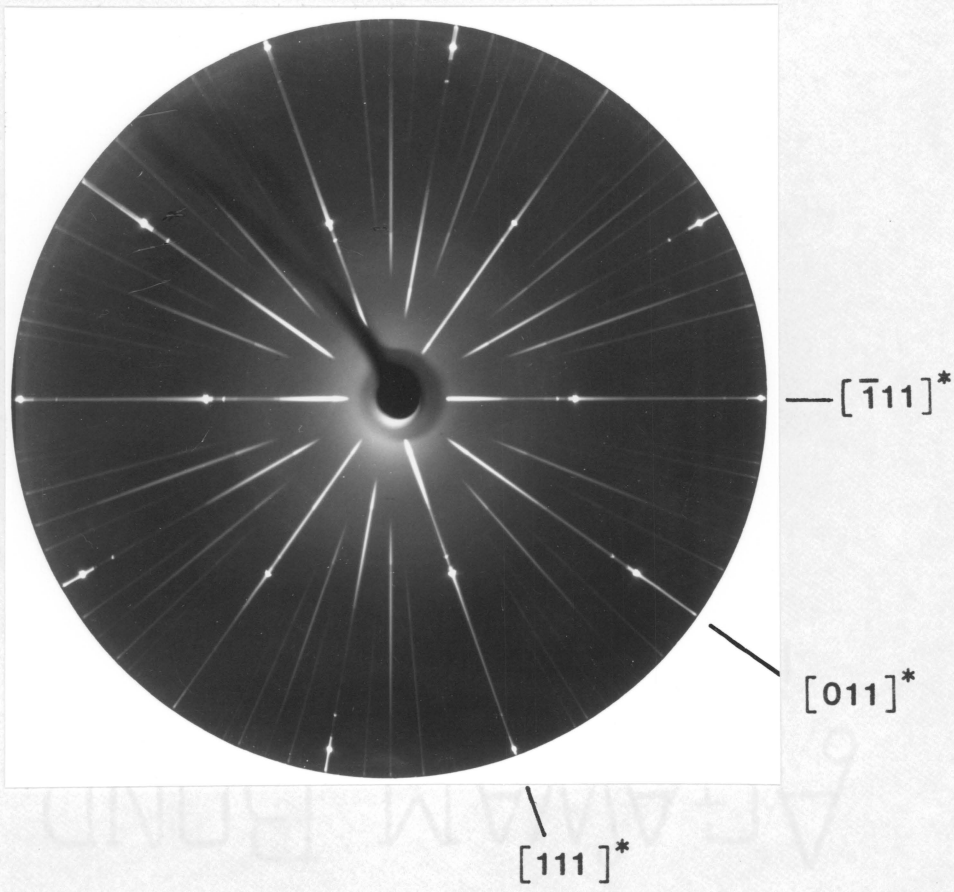

Fig. 2-5. Zero-level, [I10] axis precession photograph of sample 5 from Casapedia, Quebec: CuKα, μ = 30°, 72 hours exposure. This is a diffraction pattern of a sphalerite which is not twinned.

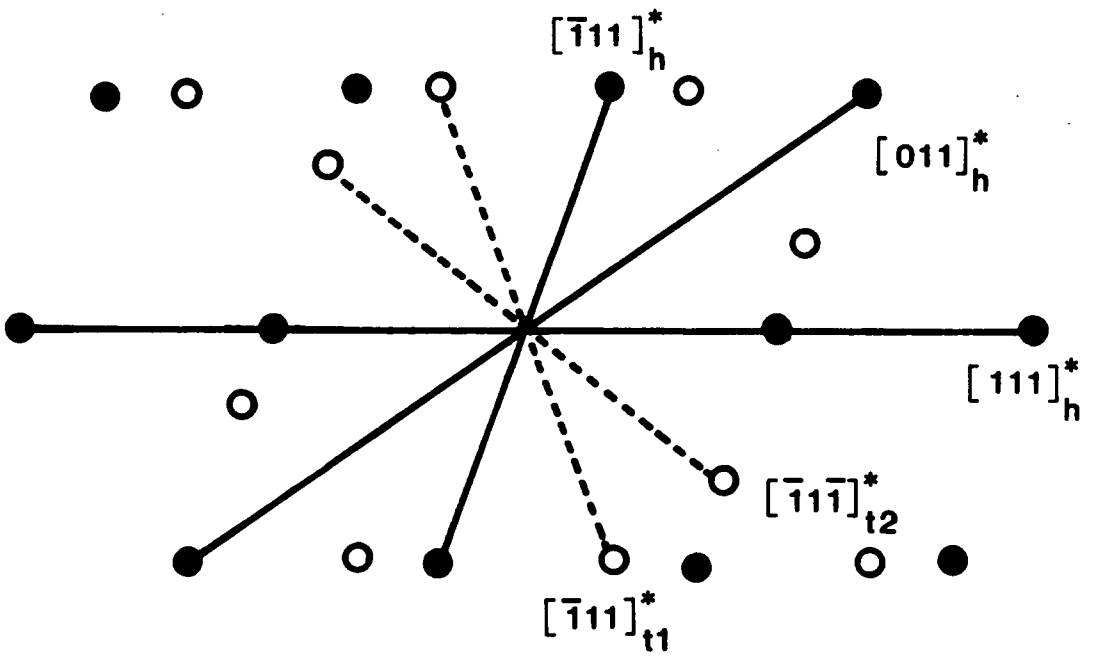

Fig. 2-6. A schematic precession diffraction pattern of a sphalerite twinned along two directions. The directions of the host are represented by the subscript "h", while the directions of the twin domains are indicated by the subscripts "t1" and "t2". The solid circles represent host reflections. The hollow circles represent twin reflections.

111 diffraction maxima and diffuse diffraction streaking along a single direction (Figures 2-7, 2-8, and 2-9). In samples 1 and 2 diffuse diffraction streaks along two directions were observed in more than one orientation (Figure 2-10). Some of the photographs also show radially diffuse reflections due to mosaic spread within the grain (Figures 2-9 and 2-10).

The volume fractions of the sphalerite host domain type and the individual twin domain types (Table 2-3) were calculated using a system of linear equations relating the relative intensities to the respective volume fractions (Appendix B). In general, the number of linear equations required is equal to the number of twinned directions observed in the precession photographs. The twin reflections can be shown to be unique using matrix methods or stereographic projections. The volume fractions calculated from the photometer data using the equations in Appendix B were compared with the relative magnitude of spot size and darkness observed on the precession photographs as a check on the "correctness" of the calculations. This is an approximate, semi-quantitative method, so that the figures quoted in Table 2-3 do not have significance past the decimal point other than relative magnitude of the diffraction maxima recorded on the precession photographs. Values less than one are included because twin reflections were indeed observed on the precession photographs along the direction indicated. Estimated standard deviations were not determined because of the semi-quantitative nature of the values.

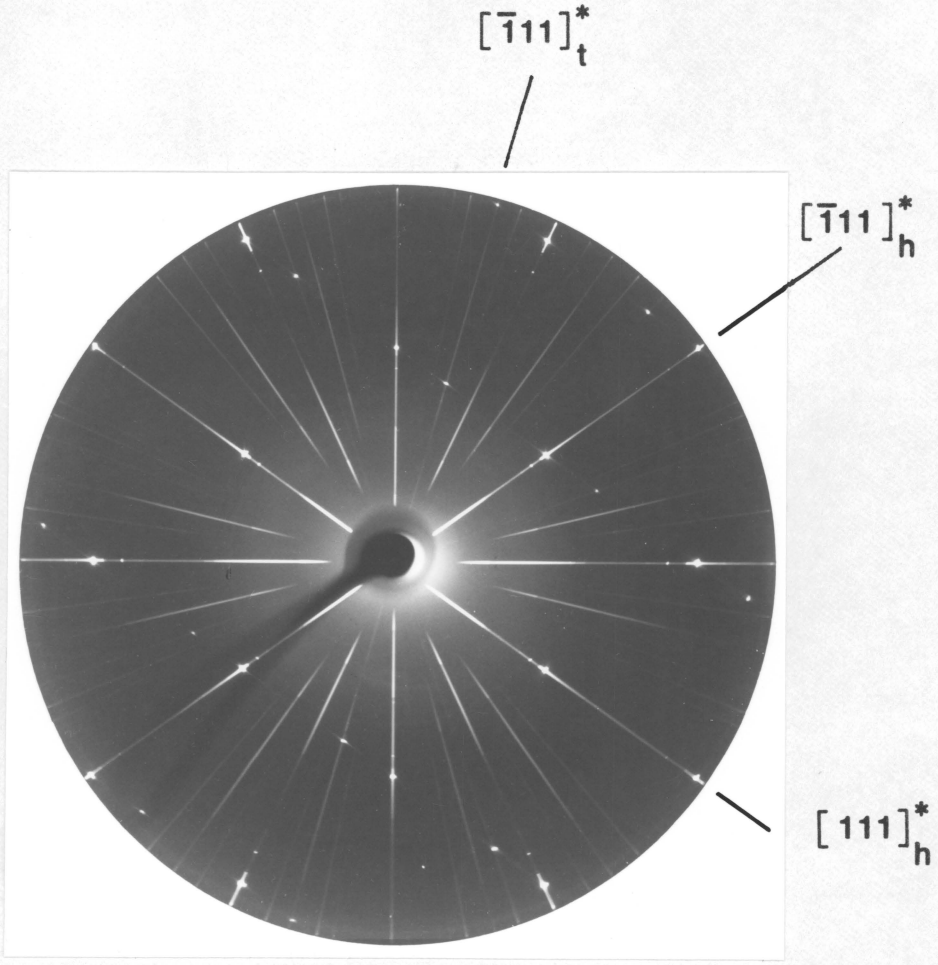

Fig. 2-7. Zero-level, [I10] axis precession photograph of sample 6 from Elmwood-Gordonsville, Tennessee: CuKα, μ = 30°, 96 hours exposure. Diffraction maxima of the host sphalerite (h) and the twin domains (t), and diffuse diffraction streaking are present along a single $[111]_h^*$ direction.

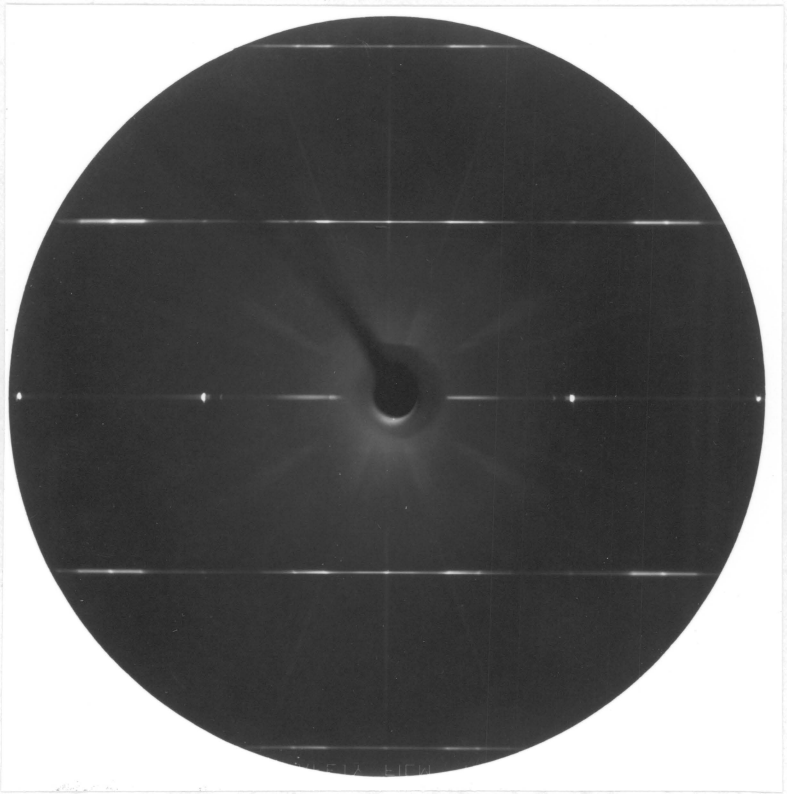

Fig. 2-8. Zero-level, [I10] axis precession photograph of sample 14 from Thomaston Dam, Connecticut: CuKα, $\mu = 30^{o}$, 96 hours exposure. Diffuse diffraction streaking along lattice rows with $h + k \neq 3n$ (equivalent hexagonal indices) in one $[111]^{*}$ direction.

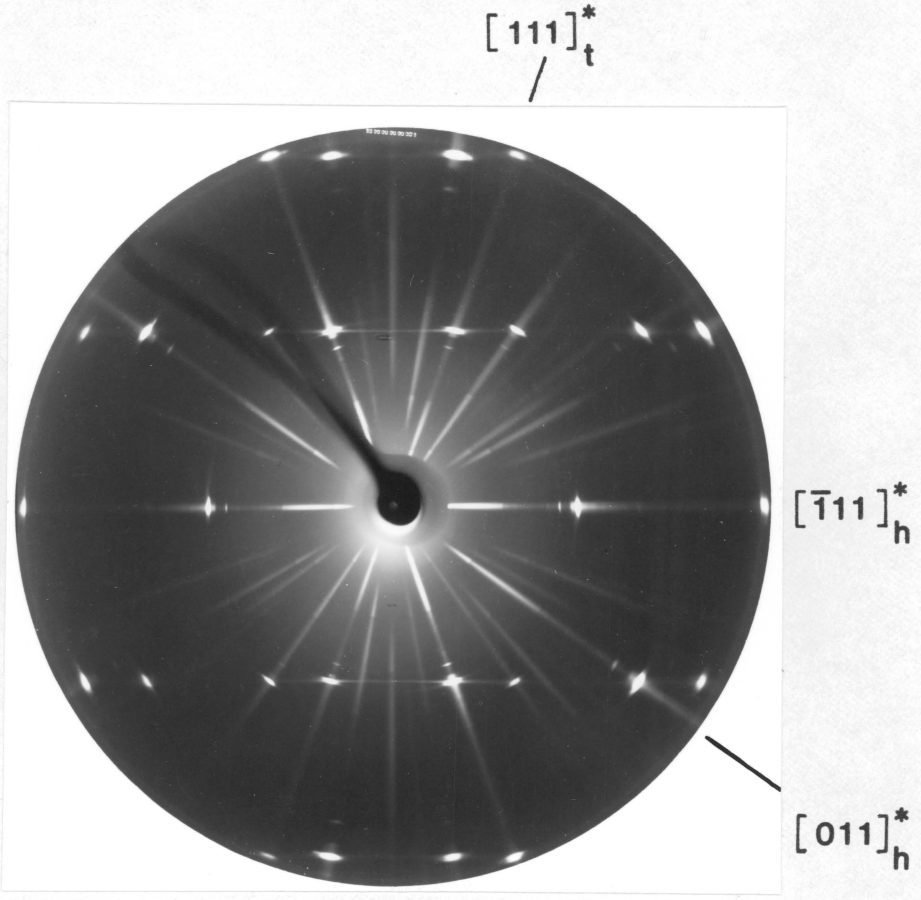

Fig. 2-9. Zero-level, [I10] axis precession photograph of sample 3 from Austinville, Virginia: CuKα, μ = 30°, 72 hours exposure. Radially diffuse diffraction maxima of the host (h) and twin (t) domains are due to mosaic spread. Diffuse diffraction streaking parallel to one [111]* direction is due to TSD.

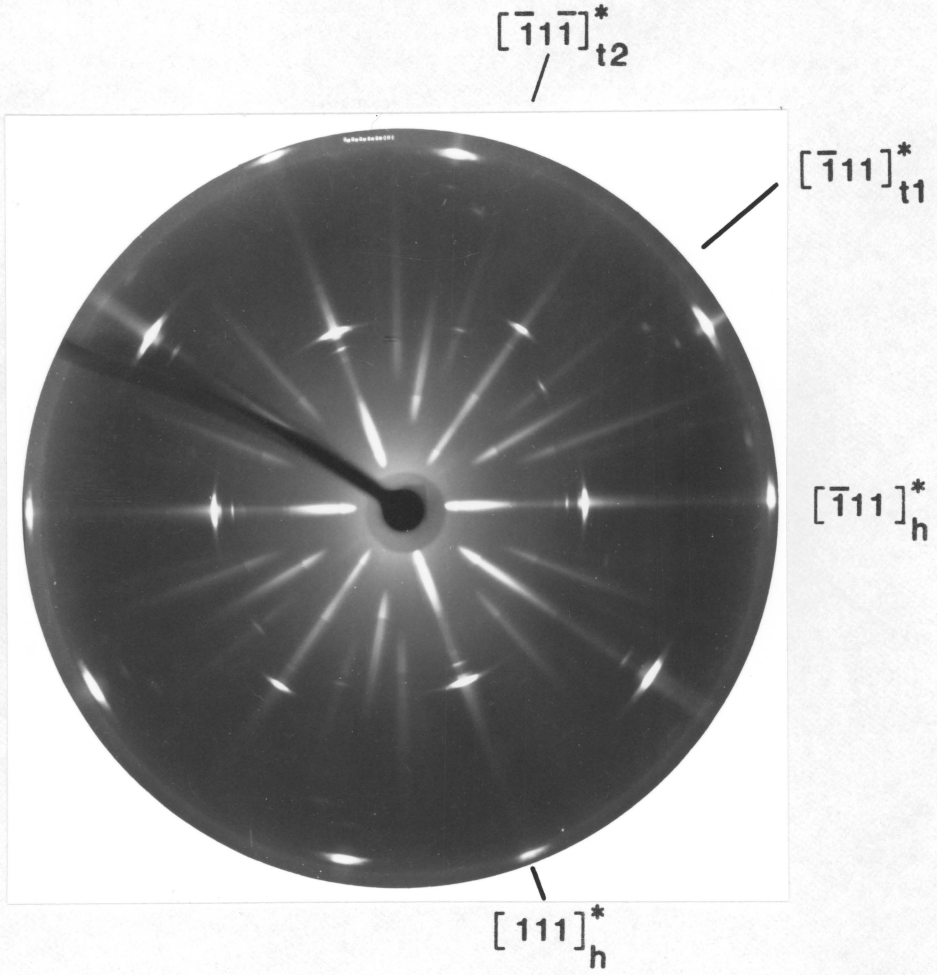

Fig. 2-10. Zero-level, [I10] axis precession photograph of sample 2 from Austinville, Virginia: CuKα, μ = 30°, 72 hours exposure. Radially diffuse diffraction maxima of the host (h) and two twin domains (t_1 and t_2) are due to mosaic spread. Twinning is indicated along two $\langle 111 \rangle^*$ directions.

Table 2-3. Volume fractions of host and twin domain types

Analysis number	Host	T_1	T_2	T_3	T_4
1	69.7	18.5	6.1	5.7	---
2	97.4	1.1	0.8	0.4	0.3
3	86.3	13.5	0.2	---	---
4	100.0	---	---	---	---
5	94.9	5.1	---	---	---
6	85.8	14.2	---	---	---
7	100.0	---	---	---	---
8	92.5	7.5	---	---	---
9	100.0	---	---	---	---
10	89.0	6.2	4.8	---	---
11	50.2	49.8	---	---	---
12	57.0	43.0	---	---	---

Note: Host refers to the volume fraction of the most abundant 3C orientation. T_1, T_2, T_3, and T_4 represent the volume fractions of twinned 3C domains oriented along each of the four symmetry-equivalent <111> directions.

The potential effects of TSD on the maximum birefringence

Precession photographs of optically anisotropic zinc sulfides are characterized by twin-equivalent diffraction maxima and diffuse diffraction streaking along lattice rows with (h-k) $\neq$ 3n (equivalent hexagonal indices) in one or two <111> directions. This has been observed in one or more photographic orientations as shown in Table 2-3. Unfortunately, the volume fractions of twin domain types cannot be used to predict the maximum birefringence because various average "twin-frequencies" may produce the same twin volume fractions, but may result in different percentages of hexagonal layers.

Therefore, dielectric tensor calculations were used to generate the maximum birefringences of zinc sulfides reported in the literature and several hypothetical zinc sulfide intergrowths based on the observed twin volume fractions. The refractive indices in Table 2-4 are those reported for a synthetic sphalerite and a synthetic wurtzite (Winchell and Winchell, 1964). The synthetic wurtzite has a maximum birefringence of 0.022, which is different from the value of 0.024 used by Fleet (1977a). Refractive indices, required for the calculations, were not reported for the 0.024 wurtzite. The stereographic coordinates refer to the orientations of the principal vibration directions of the five indicatrices, oriented so that an optic axis of a wurtzite indicatrix is parallel to each of the <111> directions of the sphalerite host. Table 2-5 reports the results for the literature values, although the calculations are based on values of ε and ω that were increased and

Table 2-4. Hauser-Wenk program input data: zinc sulfides

Domain type	3C	2H1	2H2	2H3	2H4
ρ_1	90°	90°	90°	90°	90°
ϕ_1	90°	90°	-90°	0°	180°
n_1	2.368	2.356	2.356	2.356	2.356
ρ_2	90°	144.73°	144.73°	144.73°	144.73°
ϕ_2	0°	0°	180°	-90°	90°
n_2	2.368	2.356	2.356	2.356	2.356
ρ_3	0°	54.73°	54.73°	54.73°	54.73°
ϕ_3	0°	0°	180°	-90°	90°
n3	2.368	2.378	2.378	2.378	2.378

Note: ρ and ϕ values represent the stereographic coordinates of the principal vibration directions of each indicatrix. The refractive indices are indicated by n_1, n_2, and n_3.

Table 2-5. Observed and calculated maximum birefringences (δ_o and δ_c), percentages of hexagonal layers (σ_o and σ_c), and differences between observed and calculated values ($\Delta\delta$ and $\Delta\sigma$) for zinc sulfides reported in the literature

Sample number	δ_o	δ_c*	$\Delta\delta$	σ_o	σ_c**	$\Delta\sigma$
1	0.024	0.024	0.000	100	100	0
2	0.017	0.017	0.000	70	71	1
3	0.015	0.016	0.001	66	60	6
4	0.012	0.014	0.002	60	50	10
5	0.013	0.014	0.001	57	54	3
6	0.011	0.012	0.001	50	46	4
7	0.009	0.009	0.000	38	38	0
8	0.006	0.007	0.001	30	25	5
9	0.005	0.006	0.001	27	19	8
10	0.002	0.002	0.000	10	8	2
11	0.000	0.000	0.000	0	0	0
12	0.0033	0.0043	0.001	18	14	4
13	0.0126	0.0151	0.0025	63	53	10
14	0.0145	0.0163	0.0018	68	60	8

Note: Samples 1-11 are synthethic zinc sulfides (Nelkowski and Pfutzen-Reuter, 1971). Samples 12-14 are natural zinc sulfides (Fleet, 1977a, 1977b).

* Calculated using dielectric tensors and σ_o

** Calculated assuming $\sigma_c = (\delta_o/0.024) \times 100$

decreased by 0.001, respectively, to obtain a maximum birefringence of 0.024. The calculated maximum birefringence is always greater than or equal to the observed maximum birefringence in Table 2-5. The calculated percentage of hexagonal layers is generally less than or equal to the observed percentage of hexagonal layers. This may be due to an error in birefringence determination as stated by Fleet (1977a). The results for the hypothetical intergrowths are shown in Table 2-6. Note that various intergrowths having the same percentage of hexagonal layers, σ, may have different maximum birefringences and may be biaxial as indicated by the calculated optic axial angle, 2V. Intergrowth along more than one direction would cause a maximum birefringence less than that expected based on the total percentage of hexagonal layers. This is an alternative explanation for some of the $\Delta\delta$'s in Table 2-5.

Paragenesis

The paragenesis of a sample will determine the sample's optical appearance and distribution of the TSD. Therefore, any paragenetic model that is proposed on the basis of field and other data has to be consistent with the observed optical data and the distribution of TSD seen in the precession photographs.

The effects of crystal growth and chemical substitution were discussed earlier. Some of the samples exhibit X-ray and optical results consistent with this type of origin. Seal et al. (1985) reported twinning and stacking disorder along a single direction in a

Table 2-6. Representive calculated maximum birefringences and 2V's for different distributions of hexagonal layers.

3C	2H1	2H2	2H3	2H4	σ	δ	2V
90	10	0	0	0	10	0.0022	0
90	9	1	0	0	10	0.0020	36
90	8	2	0	0	10	0.0018	54
90	5	5	0	0	10	0.0014	90
90	9	0.4	0.1	0.5	10	0.0019	22
70	30	0	0	0	30	0.0066	0
70	29	1	0	0	30	0.0064	20
70	25	5	0	0	30	0.0056	49
70	29	0.2	0.7	0.1	30	0.0069	15

Note: "3C" refers to the volume fraction of the sphalerite host domain. "$2H_1$", "$2H_2$", "$2H_3$", and "$2H_4$" refer to the volume fraction of hexagonal layers along each of the four symmetry-equivalent <111> directions. The value "σ" refers to the total percentage of hexagonal layers in the composite grain. The maximum birefringence, δ, and the optic axial angle, 2V, were calculated with the dielectric tensor program.

sphalerite (sample 6 used in this study) and that optical anisotropy is probably the result of growth defects in the sphalerite and the stabilization of hexagonal domains by Cd and Fe. Two of the other samples in the present study, 5 and 8, have diffraction patterns similar to that of sample 6. They differ in that they have lower birefringence and much less diffuse diffraction streaking. All three samples contain more Cd than most the other samples in this study. It is very probable that these samples are twinned due to growth defects and may contain hexagonal domains associated with impurities such as Cd and Fe.

The 2H→3C transition results in a composite grain dominated by hexagonal domains and containing twin-related 3C domains. The X-ray diffraction patterns are characterized by nearly continuous diffuse diffraction streaks and twin-equivalent diffraction maxima along lattice rows with $(h-k) \neq 3n$ (equivalent hexagonal indices) in a single direction. Optically, the grains show relatively high maximum birefringences. The Pribram and Thomaston Dam samples are typical of this type of intergrowth, and their origin has been discussed previously (Akizuki, 1981, 1983; Fleet, 1977a,b, 1983). The Pribram sample examined in this study shows TSD along two <111> directions of a host sphalerite which may be characteristic of a 3C→2H transition.

Three samples that show multidirectional TSD are from Austinville, Virginia. This area has a documented history of post depositional deformation and recrystallization (Foley, 1982). This would imply that twin gliding and thermal stress produced the multidirectional TSD in these sphalerites. The exact nature of the strain tensor or the thermal

stress tensor is impossible to determine without more data. The frequency of twinnning in the various directions could be used, in theory, to describe the orientation of the strain ellipsoid relative to the crystallographic axes for a given grain. It would take an undetermined number of such measurements on oriented samples to develop any kind of stress regime model.

Conclusions

Multidirectional twinning and stacking disorder occur in some natural optically anisotropic zinc sulfides. Most of the samples showing multidirectional TSD were found in an environment of documented post depositional deformation and recrystallization. One sample showing multidirectional TSD may be indicative of a 3C→2H transition. Multidirectional TSD could possibly be caused by growth defects, but this has not been confirmed by observation during this study. The samples mentioned above probably had a sphalerite precursor and are made of small slightly misoriented blocks producing the radially diffuse diffraction streaks observed on the precession photographs. Each of these small blocks probably only contains TSD along a single direction, but the composite crystal gives X-ray diffraction patterns that indicate twinning and stacking disorder along more than one direction.

Most of the optically anisotropic grains show intergrowth in only one direction. Dielectric tensor calculations confirm that maximum birefringence does vary linearly with the percentage of hexagonal layers

if the intergrowth occurs along only one direction. Similar calculations using hypothetical multidirectional zinc sulfide intergrowths resulted in biaxial optical indicatrices with maximum birefringences which are less than those predicted by the linear model.

CHAPTER THREE

Mg-Fe CHLORITOIDS: OPTICAL PROPERTIES AS A FUNCTION OF POLYTYPIC INTERGROWTH AND CHEMICAL COMPOSITION

Introduction

Optical studies of chloritoid yielded the first information concerning its polymorphism (polytypism). Hietanen (1951) pointed out that the variety of optical orientations cited in the literature and observed in her own studies implied the existence of two monoclinic forms and a triclinic form. The existence of all three forms of chloritoid were eventually confirmed by X-ray studies (Brindley and Harrison, 1952; Harrison and Brindley, 1957; Halferdahl, 1957, 1961; van der Plas et al., 1958; Hanscom, 1975, 1980; Jefferson and Thomas, 1977, 1978; see review by Ribbe, 1982).

Since X-ray diffraction techniques do not give the "exact real-space" relationships between the different forms of chloritoid, Jefferson and Thomas (1978) obtained lattice images by high resolution transmission electron microscopy (HRTEM). Their micrographs indicate various degrees of intergrowths among the different forms and conclusively confirmed the existence of the second monoclinic form and a new trigonal form. Jefferson and Thomas's study has also shown that intergrowths of monoclinic and triclinic chloritoid are the rule rather than the exception.

The present study is an attempt to close the circle by determining the effects of these monoclinic and triclinic intergrowths on the optical properties. The effects of chemical composition on the optical

properties of Mg-Fe chloritoids are presented in a quantitative way for the first time. This is an important first step to determining the effects of structural intergrowth on the optical properties. The first accurate determination of the optical orientation of predominantly triclinic chloritoid is also presented. The optical orientations of the chloritoids are shown to be very sensitive to the structural intergrowth. A physically meaningful model of the compositional and structural effects on the optical properties based on dielectric tensors is developed. Finally, a way to estimate the polytypic composition based on the optical properties is proposed. The "polytypic composition" is defined as being the relative proportions of monoclinic and triclinic chloritoid within a composite grain. The volume-averaged polytypic composition obtained in this manner may be more "meaningful" for some applications than the local polytypic composition obtained by HRTEM studies. For example, the method described in this chapter may allow petrologists to routinely determine polytypic composition because the instrumentation is readily available and inexpensive in comparison to HRTEM.

Chloritoid polytypism

Chloritoids are considered to be polytypic in this study, although there has been some debate on the subject of chloritoid polytypism. The HRTEM studies by Jefferson and Thomas (1978) combined with a versatile definition of polytypism by Thompson (1981) (see Chapter One) should

resolve the debate over whether the various forms of chloritoid are true polytypes and occur as disordered polytypic intergrowths or are simply polymorphs. The micrographs in Jefferson and Thomas (1978) show the polytypic nature of the intergrowths (Fig. 3-1). Slight variations in composition or crystal structure are "allowed" if the chloritoids are thought of as being "different ways of stacking structurally compatible tabular units or polytype modules" following Thompson's definition. Jefferson and Thomas (1978) stated that evidence "for a relationship between chemical composition and polytypism" had not been found "as yet," but that they planned such a study. Such a relationship was not observed during the present investigation. Hanscom (1980) cited the differences between observed monoclinic atomic positions and those calculated by a transformation of triclinic atomic positions to prove that the monoclinic and triclinic forms "cannot be considered polytypes." The differences are all within the maximum 2σ of the triclinic positional parameters.

Those polytypes that have been characterized, plus their lattice parameters, are listed in Table 3-1. The Hanscom (1975, 1980) parameters were obtained during crystal structure refinements of the $2M_2$ and 1Tc polytypes. The $2M_1$ parameters were determined from precession photographs (Jefferson and Thomas, 1978). The two monoclinic polytypes are related to the triclinic polytypes by twinning operations (Jefferson and Thomas, 1977). They state that the $2M_2$ polytype is "derived by twinning the 1Tc form about [010] with a composition plane" (001), while the $2M_1$ polytype is derived by twinning the 1Tc form about [110] with an

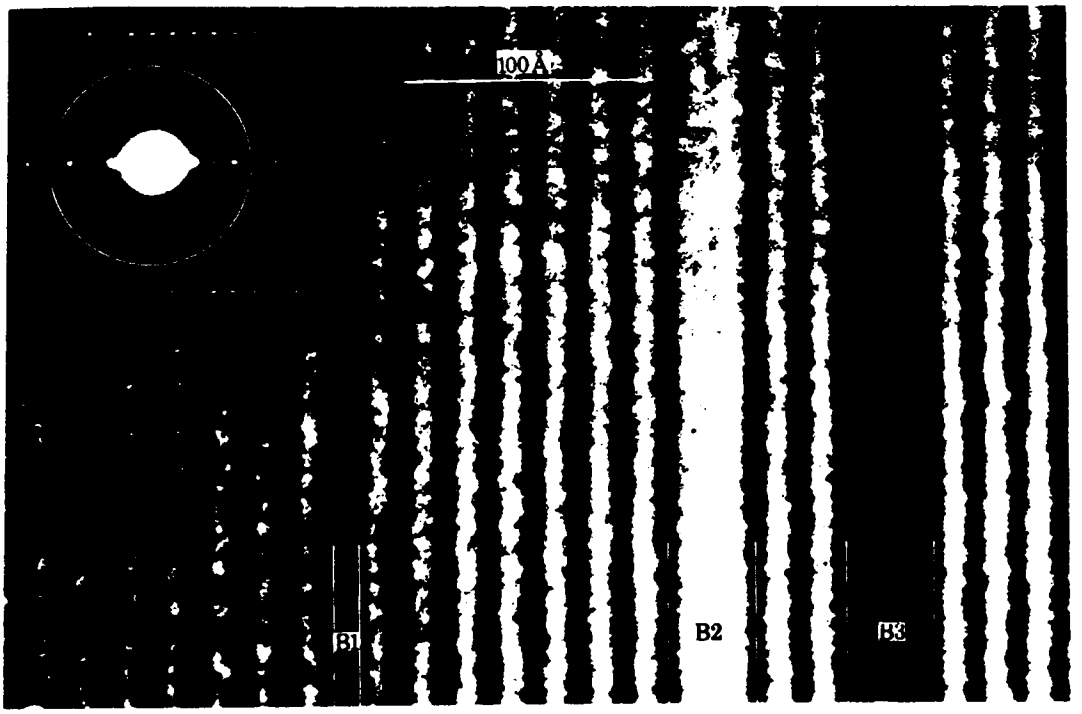

Fig. 3-1. Transmission electron photomicrograph showing a one-dimensional lattice image of a principally $2M_2$ region with triclinic intergrowths at B1 and B3, and a more complex intergrowth at B2. After Jefferson and Thomas (1978).

Table 3-1. Notation and lattice parameters for three chloritoid polytypes

Polytype Reference	1Tc Aabc [1]	2M2 Mab2c [2]	2M1* Mba2c** [3]
a (Å)	9.46	9.48	5.47
b (Å)	5.50	5.48	9.47
c (Å)	9.15	18.18	17.90
α (°)	97.05	90	90
β (°)	101.56	101.74	97.40
γ (°)	90.10	90	90
Z	4	8	8
Space Group	$C\bar{1}$	C2/c	C2/c

* Notation used by Jefferson and Thomas (1978)

** Modified Gard notation reported in Bailey (1977) and described in Chapter 1.

[1] Hanscom (1980)

[2] Hanscom (1975)

[3] Jefferson and Thomas (1978)

(001) composition plane. As will be discussed later, these relationships between the polytypes were assumed during the dielectric tensor calculations of the optical properties of a range of different intergrowths.

Chemistry and crystal structure

The chemical composition of the pure iron chloritoid end member may be represented by $Fe_2AlAl_3Si_2O_{10}(OH)_4$. The crystal structure consists of two kinds of octahedral layers, L_1 and L_2, parallel to (001) and connected by isolated silicate tetrahedra (Fig. 3-2). Chloritoid is an orthosilicate which also has characteristics in common with the phyllosilicates. The trioctahedral L_1 layer consists of two types of octahedral sites, M(1A) and M(1B) (Hanscom, 1975). The two larger symmetry-equivalent M(1B) sites contain ferrous iron and any Mg or Mn substituents (Hanscom, 1975; Tricker et al., 1977; Halenius et al., 1981). The smaller M(1A) site contains Al and may also be occupied by ferric iron (Hanscom, 1975; Tricker et al., 1977; Halenius et al., 1981). The L_2 layer has three-quarters of the possible octahedral sites filled with Al, without any observed substitution (Hanscom, 1975; Halenius et al., 1981). To indicate the chemical substitutions that occur, the formula may be written

$$[(Fe^{2+},Mg,Mn)_2(Al,Fe^{3+})]Al_3Si_2O_{10}(OH)_4.$$

Figure 3-3 shows the approximate relationship of the principal vibration directions to the crystal structure of the $2M_2$ polytype.

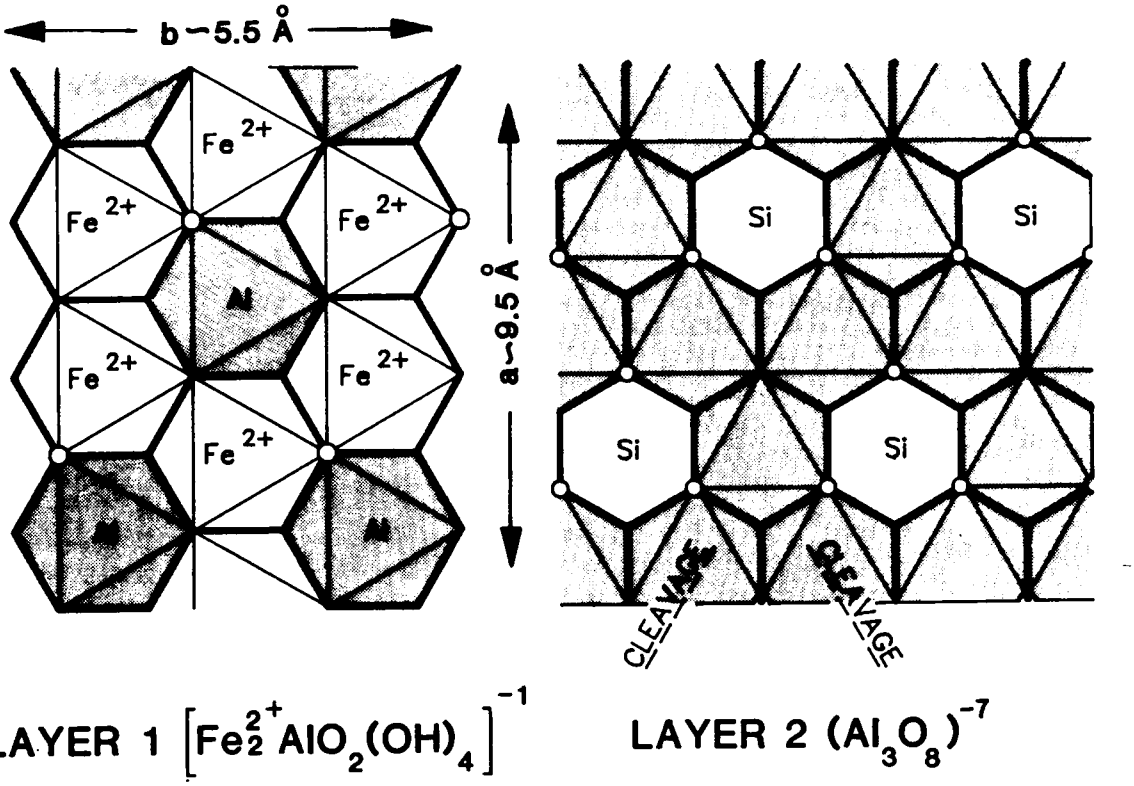

Fig. 3-2. Idealized projections on (001) of the crystal structure of chloritoid. Layer 1: the ordered Fe^{2+}/Al^{3+} cation distribution is depicted, with Fe^{2+} in the M(1B) octahedral site and Al^{3+} in the M(1A) octahedral site. Mg and Mn are assumed to substitute for Fe^{2+} in Layer 1. Layer 2: three-quarters of the octahedral sites are occupied by Al. The (110) and (1$\bar{1}$0) cleavage traces are shown. The three open circles at alternate vertices of the open hexagons labeled "Si" are the basal oxygens of the Si tetrahedra which bond layer 2 to layer 1. The vertices of these tetrahedra are the open circles shown in the drawing of layer 1.

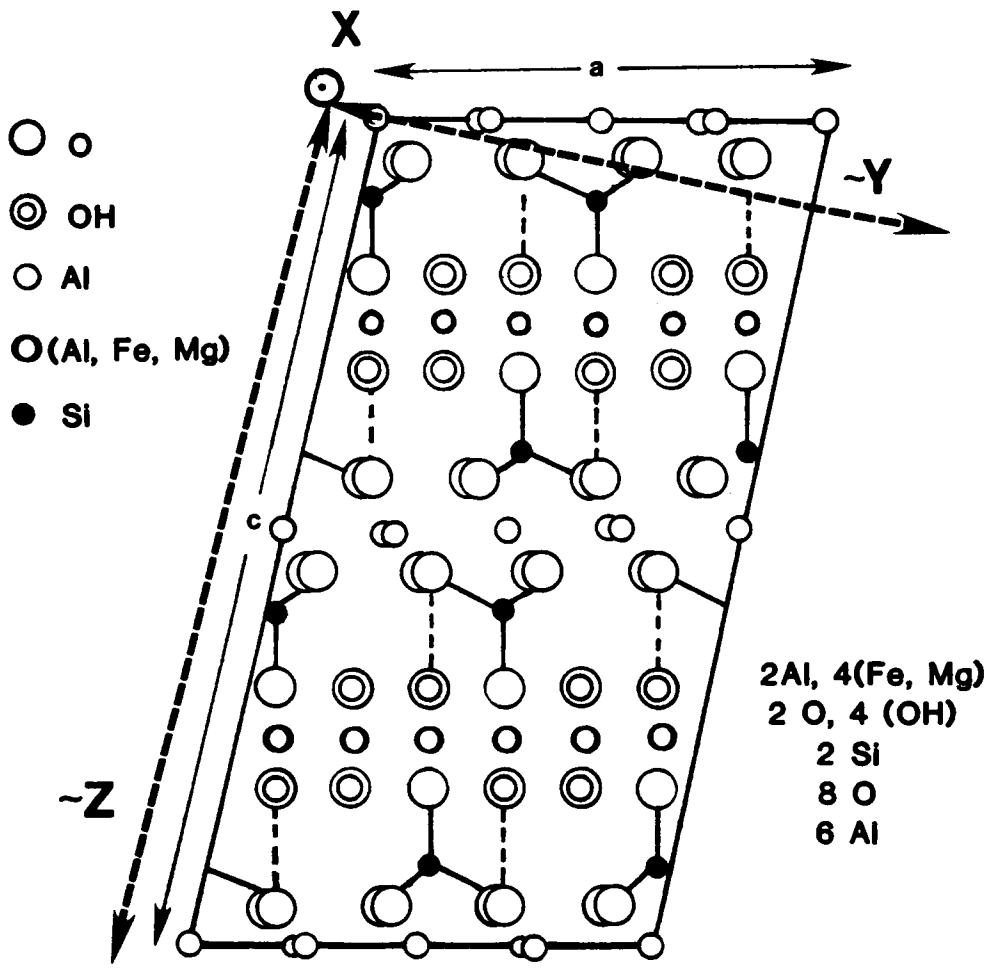

Fig. 3-3. A schematic projection of the $2M_2$ crystal structure viewed along [010] showing the relationship between the principal vibration directions and the crystallographic directions. In an ideal $2M_2$ chloritoid X = b, Z and Y lie in the ac-plane with Z nearly parallel to c. The structural projection is after Harrison and Brindley (1957).

Experimental Procedures

All the chloritoids chosen for this study are listed in Table 3-2. Not all of these samples were used in the final correlations, but all the data that were collected are tabulated because they do contribute to the general pool of information about chloritoid.

Electron microprobe analysis

Several grains of each sample were picked for chemical analysis, their maximum dimension being 0.7 mm or less. Each collection of grains was mounted in one of two possible ways; either on a one-inch glass disk using Crystal-Bond as the adhesive, or on a petrographic glass slide pre-coated with a layer of epoxy, and using epoxy as the adhesive. The first way had the advantages of easy preparation and recovery; using acetone to dissolve the Crystal-bond. This method had the disadvantages of the adhesive crazing in cold water during polishing (warm water works well) and vaporization if the vacuum-evaporator generates too much heat during the carbon-coating process. In the second method, small "pits" are dug into the epoxy already hardened on a petrographic slide. The grains are placed in these "pits" and covered with fresh epoxy. The advantage of this method is the stability of the mount during polishing and carbon-coating. The disadvantage is the difficulty of recovering the grain without damaging or losing it. The grain can usually be "popped" out with a sharp point and will not go too far if the mount is

Table 3-2. Chloritoid analysis numbers, localities, and references

Analysis number	Locality	Reference and/or original number
1	Michigamme, Michigan	EH44*
2	Natick, Rhode Island	NMNH C3708
3	Lynchburg, Virginia	TG189§
4	Leoben, Styria, Austria	NMNH R4495
5	Napo-Pastaza, Ecuador	NMNH 123815
6	Champion Iron Mine, Humbolt, Michigan	NMNH 95631
7	Chibougamau, Quebec	H-1#
8	Vielsalm, Belgium	AMNH 25085
9	Echo Lake, Vermont	AMNH 33549
10	Zlatoust, Ural Mtns., USSR	AMNH 26281
11	Pregratten, Tyrol, Austria	AMNH C85691
12	Fetlar, Shetland, England	AMNH 33341
13	Kossoibrod, Ural Mtns., USSR	AMNH 13588
14	Helen Mine, Michipicoten, Ontario, Canada	AMNH 29438
15	Euriowie, New South Wales, Australia	AMNH 30727
16	Harvey Leeds, Quebec, Canada	AMNH C85335
17	Gumach-Dagh, Turkey	AMNH C85330

Note: NMNH specimens were supplied by John S. White of the National Museum of Natural History. AMNH specimens were supplied by Martin Prinz of the American Museum of Natural History.

* Department of Geological Sciences Museum, Virginia Tech; sample supplied by R.E. Guy, Curator at that time.

§ Department of Energy Project, Virginia Tech; sample was collected by R. Tucker and supplied by F. Wehr.

\# Supplied by R. Hanscom from material he used for his crystal structure refinement of triclinic chloritoid.

covered by a drop of water. Either way the mount is prepared, it is subsequently ground and polished to produce a smooth surface on as many grains as possible. The polished samples are then carbon-coated.

The analyses were performed with an automated, nine-spectrometer ARL-SEMQ electron microprobe at an operating voltage of 15kV. The method of standardization and data collection used in this study is described by Solberg and Speer (1982). Data reduction was by the method of Bence and Albee (1968). At least three points were analyzed on each grain, resulting in a total of 5 to 19 analyses per sample.

The grains were removed from the mounts as described earlier and were cleaned and prepared for optical and X-ray examination.

X-ray procedures

A grain was examined using the precession method only after being checked for optical homogeneity. Each grain was oriented so that c^* was parallel to the dial axis of the precession camera. With this orientation it is possible to record the six "principal reciprocal lattice sections" (h0l), (hhl), (hh$\bar{1}$), (0kl), (3h,h,l), and (3h,h,$\bar{1}$) at 30° intervals; the indices being those of the $2M_2$ polytype (Jefferson and Thomas, 1978). Most of the X-ray precession photographs were taken with Ni-filtered Cu radiation and a precession angle of 30°, although a few photographs were taken using either Zr-filtered Mo radiation or MnO_2-filtered Fe radiation. Exposure times on the order of 72 hours were usually needed to observe weak diffraction streaks along reciprocal

lattice rows parallel to c^*, the stacking direction.

A Helena Laboratories "Quick Scan" scanning densitometer was used to obtain relative intensity data. Scans were run along the white radiation streaks of the 021, 022, $02\bar{1}$, $02\bar{2}$ reflections, the 001 reciprocal lattice row, and along the 021 reciprocal lattice rows.

Optical procedures

Optical measurements were made before and after X-ray examination using the spindle stage methods described by Bloss (1981). Extinction data were collected using the "360° option" and a Nakamura plate at the following wavelengths: 486 nm, 526 nm, and 589 nm. The EXCALIBR computer program described in Bloss (1981) was used to determine the spindle stage coordinates of the principal vibration directions and the value of the optic axial angle from the extinction data.

In preparation for the measurement of the refractive indices, the refractive index oils were calibrated using the procedures described by Su et al. (1987). The refractive index oils used in this study were Cargille oils 1.715, 1.720, 1.725, 1.730, and 1.735; the glass was Corning Glass 8293. The minimum deviation data provided by Corning, the Sellmeier constants calculated from this data, and those calculated from double-variation data are all reported in Table 3-3. The principal vibration directions of each grain were oriented parallel to the polarizer using the spindle stage coordinates calculated by EXCALIBR. The refractive indices were determined using the double-variation method

Table 3-3. Optical glass #8293 calibration data

Linearized Sellmeier Constants

	Minimum Deviation*	Double Variation**
a_0	0.53012(7)	0.5342(2)
a_1	-6607(19)	-8145(67)

Refractive Indices

λ (nm)	Minimum Deviation	Double Variation	Δ
435.800	1.737446	1.7422(4)	0.0048
486.133	1.729575	1.7324(4)	0.0028
546.100	1.723037	1.7242(3)	0.0012
589.290	1.719520	1.7200(3)	0.0005
632.800	1.716658	1.7164(3)	-0.0003
656.300	1.715331	1.7148(3)	-0.0005

* Sellmeier constants based on SAS GLM fit of refractive indices and wavelengths given by Corning Glass Works.

** Sellmeier constants calculated with the computer program GLASS using 100 double variation observations.

and the data reduction procedures described by Su et al. (1987).

Results

Chemical composition

The analyses of the grains examined optically are reported in Table 3-4. Only those components that were statistically significant and could not be attributed to inclusions are listed. Some inclusions that were accidentally analyzed were ilmenite, quartz and possibly magnetite. Halferdahl (1961) discusses the various inclusions that are often present and their effects on the chemical composition. The ferric iron reported in Table 3-4 is an estimate based on aluminum deficiency, where "aluminum deficiency" refers to the difference between the observed formula number of Al and ideal case of 4 Al (Fe^{3+} ~ 4 - Al). Data from 11 wet chemical analyses reported by Halferdahl (1961) were used to obtain a correlation between ferric iron content and aluminum deficiency. The correlation equation is

$$Fe^{3+} = 0.69(5) \times [4 - Al], \quad [F = 231.64, \; r^2 = 0.959]$$

where Fe^{3+} and Al refer to the number of cations based on 12 oxygens. This equation indicates a good correlation between ferric iron content and aluminum deficiency, but is not meant to be used to calculate ferric iron content. If any physical significance was to be placed upon the coefficient of this equation, it would be to suggest that one or both aluminum sites are occasionally vacant.

Table 3-4. Chemical compositions of the chloritoids listed in Table 3-2

Analysis number	Ideal	1	2	3	4	5
SiO_2 (wt. %)	23.85	24.1 (2)	24.2 (2)	24.4 (2)	24.0 (2)	25.0 (2)
Al_2O_3	40.48	40.4 (7)	40.3 (7)	39.6 (7)	40.4 (7)	42.0 (7)
FeO*	28.52	26.5 (1)	27.7 (1)	25.6 (1)	26.1 (1)	22.2 (1)
MnO	0.00	0.31(3)	0.28(3)	1.2 (1)	0.30(3)	0.28(3)
MgO	0.00	0.93(2)	0.23(1)	1.48(3)	1.12(2)	3.51(7)
H_2O**	(7.15)	(7.22)	(7.18)	(7.22)	(7.23)	(7.39)
Total	100.00	99 (1)	100 (1)	99 (1)	99 (1)	100 (1)
		Formulas based on 10 0, 4 OH				
Si	2.00	2.02(5)	2.03(5)	2.04(5)	2.01(5)	2.02(2)
Al	4.00	4.0 (1)	4.0 (1)	3.9 (1)	4.0 (1)	4.0 (1)
Fe^{3+}§	0.00	(0.0 (1))	(0.0 (1))	(0.1 (1))	(0.0 (1))	(0.0 (1))
Fe^{2+}	2.00	1.84(4)	1.91(4)	1.72(4)	1.82(4)	1.50(3)
Mn^{2+}	0.00	0.022(3)	0.020(3)	0.09(1)	0.021(3)	0.019(2)
Mg	0.00	0.116(4)	0.029(1)	0.185(6)	0.140(5)	0.42(1)
$Mg/(Mg+Fe^{2+}+Mn)$	0.00	0.058(3)	0.014(1)	0.089(5)	0.070(4)	0.22(1)

* All iron reported as FeO ** Weight percent water calculated from formulas assuming 4 OH
§ Values for Fe3+ and Fe2+ were determined assuming a total of 4 trivalent cations

Table 3-4. Continued

Analysis number	6	7	8	9	10	11
SiO_2	24.3 (2)	25.0 (2)	24.8 (2)	24.4 (2)	24.9 (2)	25.1 (2)
Al_2O_3	41.0 (7)	40.7 (7)	40.9 (7)	40.6 (7)	41.1 (7)	41.5 (7)
FeO*	27.1 (1)	27.2 (1)	20.7 (1)	24.6 (1)	25.7 (1)	24.2 (1)
MnO	0.11(1)	0.42(5)	5.7 (6)	0.59(7)	0.15(2)	0.20(2)
MgO	0.68(1)	0.78(2)	1.28(3)	2.36(5)	1.87(4)	2.72(6)
H_2O**	(7.22)	(7.20)	(7.25)	(7.27)	(7.26)	(7.31)
Total	100 (1)	101 (1)	101 (1)	100 (1)	101 (1)	101 (1)
	Formulas based on 10 0, 4 OH					
Si	2.01(5)	2.05(5)	2.04(5)	2.02(5)	2.04(5)	2.03(5)
Al	4.0 (1)	3.9 (1)	4.0 (1)	4.0 (1)	4.0 (1)	4.0 (1)
Fe^{3+}§	(0.0 (1))	(0.1 (1))	(0.0 (1))	(0.0 (1))	(0.0 (1))	(0.0 (1))
Fe^{2+}	1.87(4)	1.83(4)	1.39(3)	1.67(3)	1.73(3)	1.62(3)
Mn^{2+}	0.008(1)	0.029(4)	0.40(5)	0.041(5)	0.010(1)	0.014(2)
Mg	0.084(3)	0.095(3)	0.157(6)	0.29(1)	0.228(8)	0.33(1)
$Mg/(Mg+Fe^{2+}+Mn)$	0.043(2)	0.048(3)	0.079(7)	0.143(8)	0.114(6)	0.166(9)

* All iron reported as FeO ** Weight percent water calculated from formulas assuming 4 OH
§ Values for Fe3+ and Fe2+ were determined assuming a total of 4 trivalent cations

Table 3-4. Continued

Analysis number	12	13	14	15	16	17
SiO_2	24.9 (2)	24.5 (2)	24.5 (2)	24.8 (2)	24.8 (2)	24.6 (2)
Al_2O_3	39.7 (7)	40.5 (7)	40.9 (7)	41.0 (7)	40.4 (7)	40.3 (7)
FeO*	25.2 (1)	26.0 (1)	26.0 (1)	23.2 (1)	27.5 (1)	26.9 (1)
MnO	0.42(5)	0.40(5)	0.21(2)	0.54(6)	0.56(6)	0.46(5)
MgO	2.32(5)	2.19(4)	1.77(4)	2.59(5)	1.34(3)	1.11(2)
H_2O**	(7.25)	(7.23)	(7.24)	(7.33)	(7.18)	(7.20)
Total	100 (1)	101 (1)	101 (1)	100 (1)	101 (1)	101 (1)
			Formulas based on 10 0, 4 OH			
Si	2.06(5)	2.01(5)	2.02(5)	2.04(5)	2.04(5)	2.04(5)
Al	3.9 (1)	3.9 (1)	4.0 (1)	4.0 (5)	3.9 (1)	3.9 (1)
Fe^{3+}§	(0.1 (1))	(0.1 (1))	(0.0 (1))	(0.0 (1))	(0.1 (1))	(0.1 (1))
Fe^{2+}	1.66(3)	1.74(3)	1.76(3)	1.58(3)	1.81(4)	1.81(4)
Mn^{2+}	0.029(4)	0.028(4)	0.015(2)	0.038(5)	0.039(5)	0.032(4)
Mg	0.29(1)	0.269(9)	0.217(7)	0.32(1)	0.164(6)	0.137(5)
$Mg/(Mg+Fe^{2+}+Mn)$	0.139(8)	0.129(7)	0.107(6)	0.163(9)	0.079(4)	0.067(4)

* All iron reported as FeO ** Weight percent water calculated from formulas assuming 4 OH
§ Values for Fe3+ and Fe2+ were determined assuming a total of 4 trivalent cations

Precession photographs

A range of polytypic intergrowths is indicated by the diffraction streaking and multiple diffraction patterns observed on the precession photographs (Figs. 3-4, 3-5, and 3-6). The first pair of photographs (Fig. 3-4) are representative of (h0l) and (0kl) diffraction patterns of a $2M_2$ chloritoid with only minor polytypic intergrowth (sharp maxima and faint diffraction streaking). The (h0l) and (0kl) sections of a 1Tc chloritoid show only the 8.9 Å repeat distance in both orientations (Fig. 3-5). Both photographs in Fig. 3-5 contain minor diffraction streaking and the diffraction maxima from a small triclinic domain rotated 60° relative to the host domain. This domain was detected optically under crossed polarized illumination. Relatively high amounts of polytypic intergrowth yield dark, continuous diffraction streaks on the (0kl) section (Fig. 3-6b). The $2M_2$ and 1Tc polytypes have identical (h0l) reciprocal lattice sections, so that a sharp diffraction pattern should be produced even if the grain is polytypically intergrown. If the pattern is not free of diffraction streaks (Fig. 3-6a), there are other triclinic and/or monoclinic orientations present in the composite grain. The volume fractions determined by densitometry are reported in Table 3-5.

Optical parameters

The refractive indices and the orientation angles measured at 589

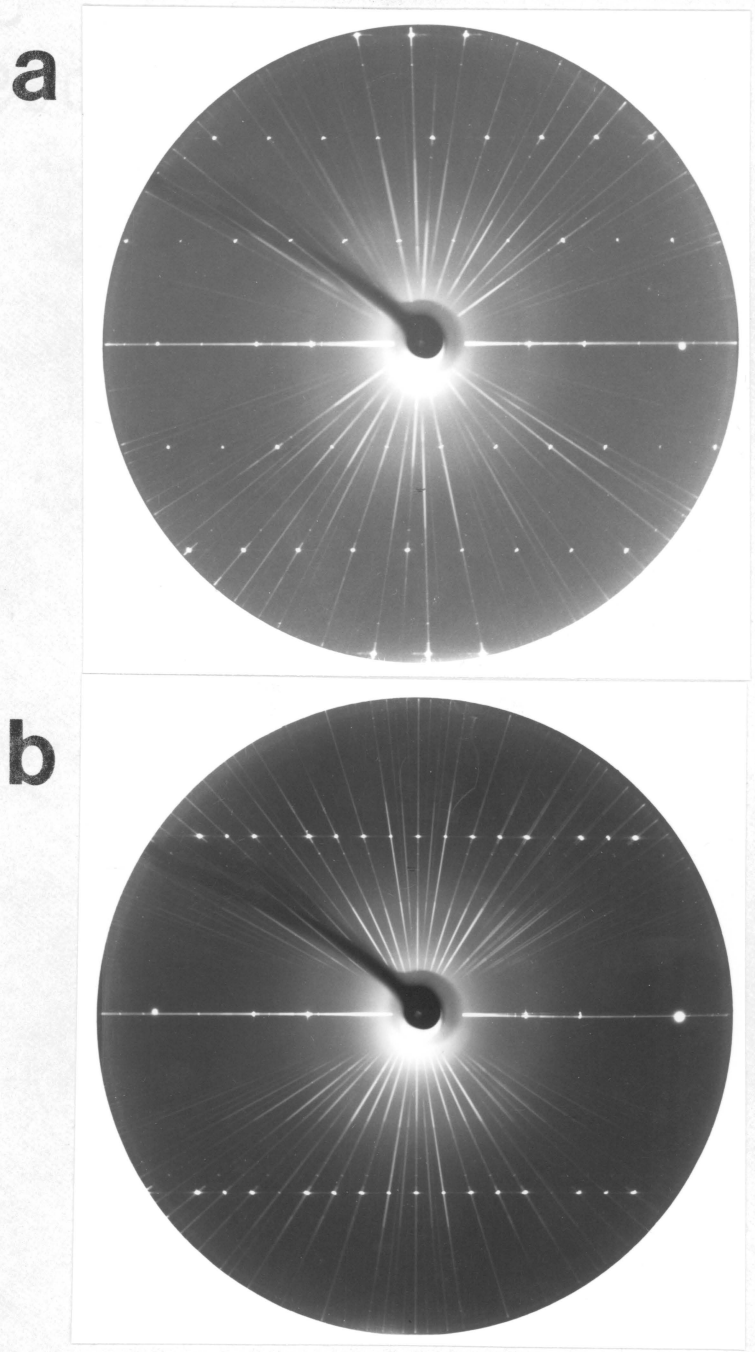

Fig. 3-4. Zero-level precession photographs of sample 5 from Napo-Pastaza, Ecuador, which show the diffraction patterns of relatively pure $2M_2$ chloritoid. (a) hOl orientation, CuKα, μ = 30°, 118 hours exposure. (b) Okl orientation, CuKα, μ = 30°, 96 hours exposure.

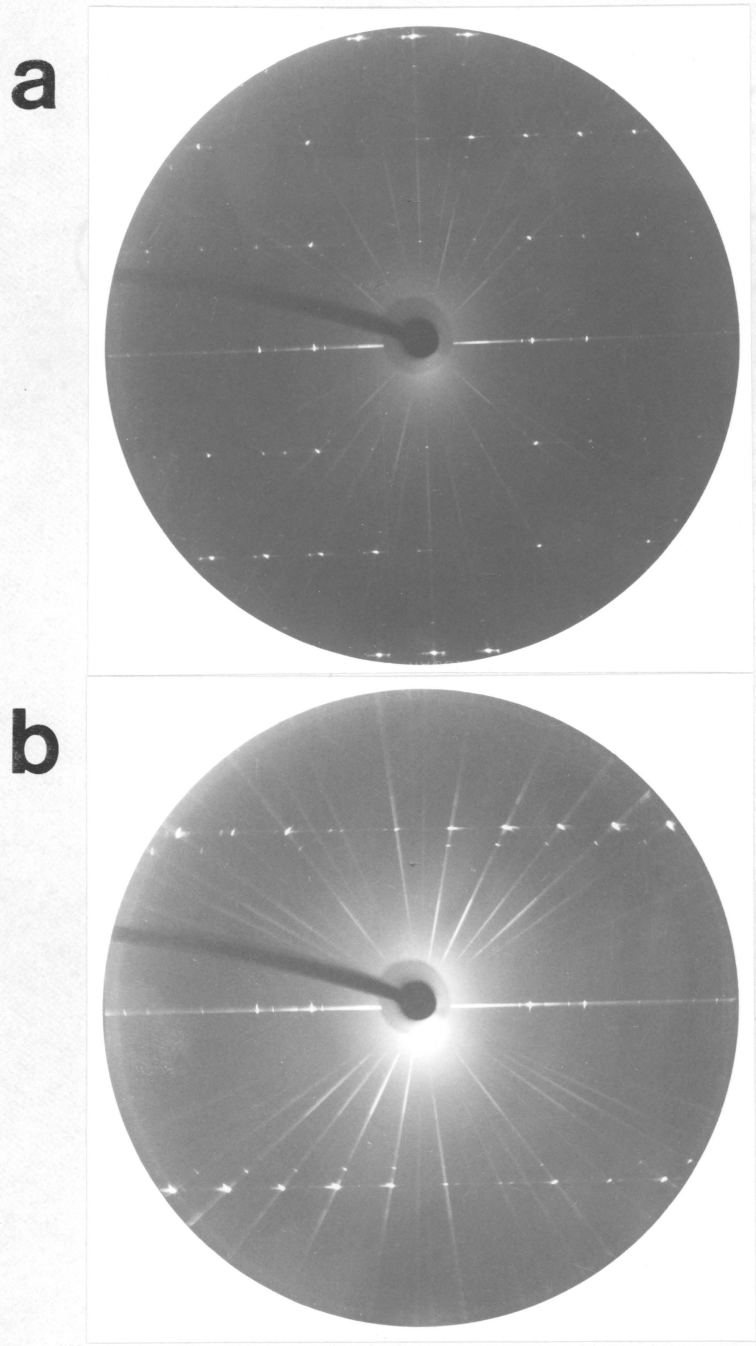

Fig. 3-5. Zero-level precession photographs of sample 7 from Chibougamau, Quebec, which show the diffraction patterns of relatively pure 1Tc chloritoid. (a) h0l orientation, CuKα, μ = 30°, 37 hours exposure. (b) 0kl orientation, CuKα, μ = 30°, 48 hours exposure. Some of the faint diffraction maxima along the lattice rows are caused by a small domain of a different orientation.

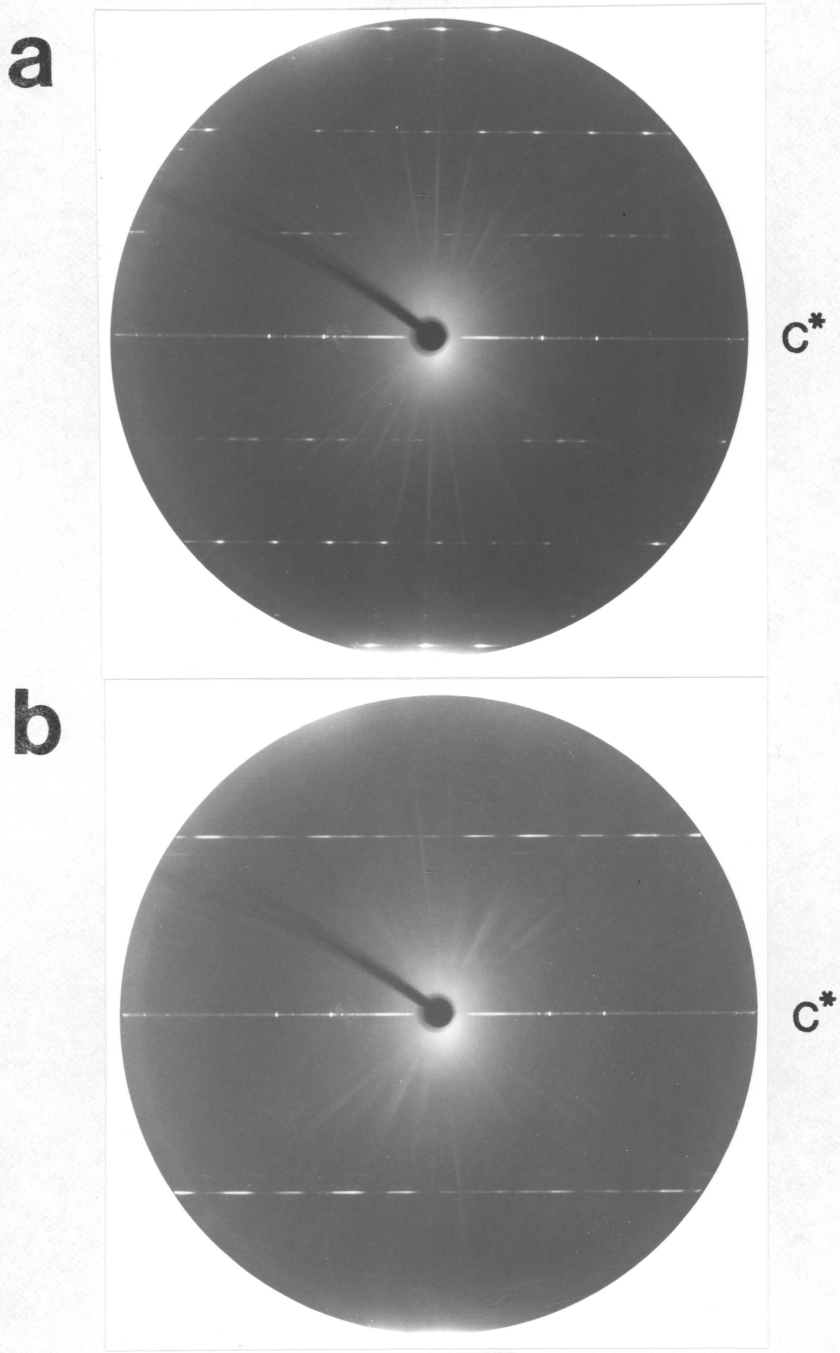

Fig. 3-6. Zero-level precession photographs of sample 9 from Echo Lake, Vermont, which show the diffraction patterns of intergrown $2M_2$ and 1Tc chloritoid. (a) h0l orientation, CuKα, μ = 30°, 76 hours exposure. (b) 0kl orientation, CuKα, μ = 30°, 86 hours exposure.

nm are listed in Table 3-5. The estimated standard deviations on the refractive indices are higher than those obtained in most spindle stage studies because chloritoid is darkly colored in some orientations, and the refractive index oils in the range used are volatile relative to those having lower refractive indices.

The optical orientation is specified relative to the a, b, and c^* directions for all polytypic intergrowths. The stacking direction of the polytypic intergrowths is parallel to c^*, so that c^* and the perpendicular to (001) of all the polytypes are parallel. Since γ is 90.1° for the triclinic polytype, the a and b directions of the triclinic polytype approximately correspond to a and b of the monoclinic polytypes. Therefore, the a, b, and c^* directions provide a very useful basis for expressing the optic orientation. The angles between the principal vibration directions and c^* do not satisfactorily describe the optical orientations of the triclinic polytype or submicroscopic polytypic intergrowths. The optical orientations recorded in Table 3-5 represent the first accurate optical orientations reported for the triclinic polytype and polytypic intergrowths.

Data Analysis and Discussion

Optical properties versus chemical composition

Numerous attempts were made during this study to correlate the optical properties of chloritoids to all compositional variables simultaneously. Various Statistical Analysis System (Helwig and

Table 3-5. Optical parameters and volume fractions

Analysis number	1	2	3	4	5	6	7	8
α	1.727(1)	1.728(1)	1.724(1)	1.725(1)	1.721(1)	1.725(1)	1.725(1)	1.724(1)
β	1.728(1)	1.729(1)	1.730(1)	1.726(1)	1.722(1)	1.727(1)	1.730(1)	1.725(1)
γ	1.733(1)	1.732(1)	1.732(1)	1.730(1)	1.726(1)	1.733(1)	1.732(1)	1.730(1)
$2V_z$	54.9(5)	57 (1)	123 (1)	69 (1)	58 (1)	66 (1)	114.0(8)	85 (1)
				Angles defining the optic orientation				
$\angle X \hat{} a$	87 (1)	84 (2)	89 (1)	84 (2)	85 (1)	81 (2)	54.9(6)	59 (1)
$\angle Y \hat{} a$	22.5(9)	27 (1)	22 (1)	18 (1)	15 (1)	28 (1)	39.1(7)	42 (1)
$\angle Z \hat{} a$	112.3(6)	116.1(6)	112.3(7)	107.0(6)	104.4(7)	116.3(8)	105.1(8)	118.5(8)
$\angle X \hat{} b$	10 (1)	8 (2)	4 (1)	6 (2)	5 (1)	11 (2)	38.8(7)	33 (1)
$\angle Y \hat{} b$	96.0(8)	98 (2)	93 (2)	96 (2)	95 (1)	101 (2)	128 (1)	123 (1)
$\angle Z \hat{} b$	97.4(6)	91.8(6)	92.9(7)	90.5(6)	90.1(7)	90.4(8)	97 (1)	90.2(8)
$\angle X \hat{} c^*$	80.9(9)	84.9(9)	86 (1)	88.7(7)	88.7(9)	85 (1)	75.6(7)	74.8(8)
$\angle Y \hat{} c^*$	68 (1)	64.4(9)	67.8(8)	73.0(8)	75.6(9)	64.3(8)	82 (1)	66.5(9)
$\angle Z \hat{} c^*$	23.6(8)	26.2(6)	22.5(7)	17.0(6)	14.4(7)	26.3(8)	16.5(8)	28.5(8)
				Volume fractions				
$2M_2$ (%)	<100 (5)	90 (5)	n.d.	n.d.	90 (5)	n.d.	>0	50 (5)

Note: Values in parentheses represent esd's for last decimal place.
"n.d." = not determined (see text)

Table 3-5. Continued

Analysis number	9	10	11	12	13	14	16	17
α	1.724(1)	1.724(1)	1.724(1)	1.723(1)	1.726(1)	1.723(1)	1.727(1)	1.726(1)
β	1.728(1)	1.726(1)	1.725(1)	1.725(1)	1.728(1)	1.728(1)	1.730(1)	1.728(1)
γ	1.730(1)	1.730(1)	1.728(1)	1.730(1)	1.733(1)	1.731(1)	1.736(1)	1.732(1)
$2V_z$	108 (2)	45 (2)	58 (1)	60 (2)	34 (2)	103 (1)	54 (1)	54 (2)
				Angles defining the optic orientation				
$\angle X \wedge a$	69 (3)	75 (3)	82 (2)	75 (3)	81 (3)	56.7(8)	52 (1)	70 (3)
$\angle Y \wedge a$	21 (3)	27 (3)	19 (2)	22 (3)	9 (3)	38.3(9)	46 (1)	34 (3)
$\angle Z \wedge a$	94 (2)	112 (1)	108 (9)	105 (1)	90 (1)	103 (1)	105.4(6)	116 (1)
$\angle X \wedge b$	21 (3)	16 (3)	8 (2)	16 (3)	9 (3)	38.3(8)	46 (1)	22 (3)
$\angle Y \wedge b$	111 (3)	106 (3)	98 (2)	106 (3)	99 (3)	128 (1)	135 (1)	112 (3)
$\angle Z \wedge b$	92 (2)	91 (1)	91.5(9)	91 (1)	92 (1)	96 (1)	97.9(6)	91 (1)
$\angle X \wedge c^*$	83 (1)	85 (2)	89 (1)	84 (1)	89 (1)	77.4(8)	73.5(9)	82 (2)
$\angle Y \wedge c^*$	80 (1)	73 (1)	73 (1)	76 (1)	89 (1)	84 (1)	85 (1)	71.5(8)
$\angle Z \wedge c^*$	14 (1)	18 (1)	17.2(9)	15 (1)	2 (1)	14.4(9)	17.4(6)	20.1(8)
				Volume fractions				
$2M_2$ (%)	16 (5)	n.d.	<100 (5)	<100 (5)	n.d.	>0 (5)	>0 (5)	n.d.

Council, 1979) procedures have been used to test several models of the effects of chemistry on the optical parameters. Models were designed to correlate formula numbers, oxide weight percentages, ratios of formula numbers, or ratios of weight percents with optical properties such as the refractive indices, the optic axial angle, optical orientation angles, and the dispersive power. Other models involved different weighting schemes based on polarizability or the Gladstone-Dale relationship (Lasaga and Cygan, 1982; Mandarino, 1976, 1978, 1979, 1981; Bloss et al., 1983). Weighting schemes generally diminished the correlation they were supposed to enhance because they predetermined the correlation. Using oxide weight percentages as compositional variables is not recommended because they are not independent variables. Correlations based on the dispersion of the refractive indices were attempted but resulted in low correlation parameters. Relatively high correlations were obtained using ratios of formula numbers. The proportion of Mg to other cations in the M(1B) sites shows the highest correlation, which is to be expected because of the polarizability difference between Mg (0.48 $Å^3$) and Fe^{2+} (1.66 $Å^3$) (Lasaga and Cygan, 1982). A similar correlation was previously suggested by Halferdahl (1961).

The data available during this study do not satisfactorily cover the entire compositional range of the chloritoids. The polytypic composition affects several of the optical parameters, accounting for much of the scatter in Halferdahl's Figure 8 (1961, p. 89). Therefore, a stepwise approach was employed to determine the chemical dependence of

the optical parameters. The first step was a correlation based on the chemical and optical parameters of approximately pure $2M_2$ chloritoids along the Mg-Fe join having less than 4 atomic percent Mn^{2+} in M(1B) and less than 19 atomic percent Fe^{3+} in M(1A). Strong correlations between the refractive indices and Mg/(Mg + Fe + Mn) were obtained (Table 3-6)(Figure 3-7). The correlations between the proportion of Mg and the variable orientation angles (unrestricted by symmetry) were weaker (Table 3-6)(Figure 3-8). The next step was to determine a similar correlation for approximately pure 1Tc chloritoids along the Mg-Fe join which have less than 2 atomic percent Mn in M(1B) and less than 19 atomic percent Fe^{3+} in M(1A). The correlations obtained were very weak due to the limited amount and range of data available. There were not enough samples with intermediate polytypic compositions to determine the chemical effects on the optical properties of varying ratios of polytypic intergrowths.

Optical properties versus polytypic composition

Several statistical models comparing the polytypic composition to individual optical parameters and combinations of optical parameters were examined. None of the models resulted in physically meaningful correlations, although some important trends were observed.

The refractive indices α and β are dependent upon the polytypic composition, because the X and Y principal vibration directions of the triclinic polytypes do not lie in the (001) plane and are in a position

Table 3-6. Regression-derived equations relating optical parameters of $2M_2$ chloritoids to Mg/(Mg + Fe + Mn) (MGN) (10 observations)

Equation number	Equation	R^2	F	PR > F
3-1	α = 1.7279(4) - 0.034(3)MGN	0.96	181	0.0001
3-2	β = 1.7290(3) - 0.034(2)MGN	0.97	292	0.0001
3-3	γ = 1.7339(5) - 0.036(3)MGN	0.94	125	0.0001
3-4	YA = 27(2) - 58(16)MGN	0.76	13	0.0232
3-5	YC = 65(2) - 55(8)MGN	0.85	41	0.0004
3-6	ZA = 116(2) - 57(15)MGN	0.78	14	0.0193
3-7	ZC = 26(1) - 57(8)MGN	0.87	55	0.0001

Note: "YA", "YC", "ZA", and "ZC" refer to optic orientation angles which do not have positions that are fixed due to symmetry restrictions in $2M_2$ chloritoids.

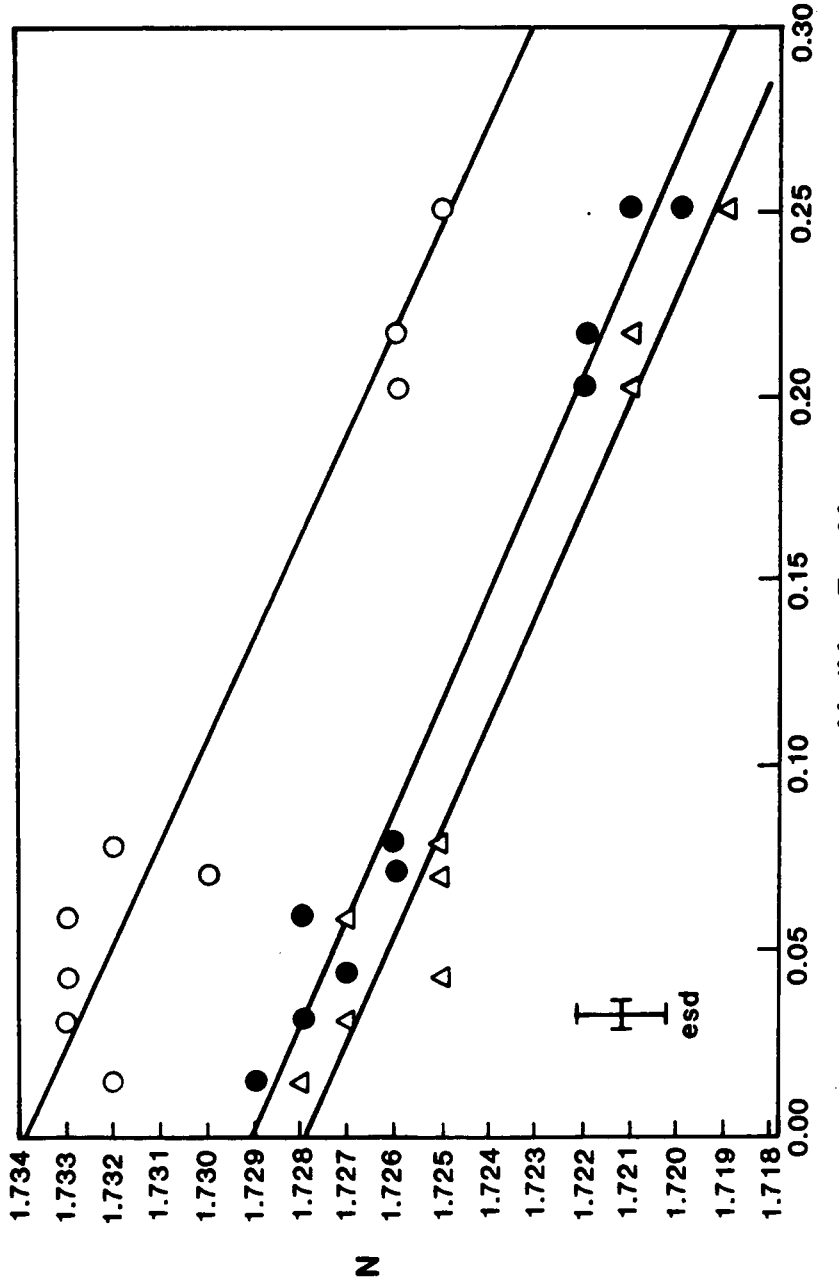

Fig. 3-7. Variation of refractive indices of $2M_2$ chloritoid with the proportion of magnesium, Mg/(Mg + Fe + Mn), in the M(1B) octahedral site. The regression lines correspond to the equations given in Table 3-6. The "esd" symbol represents an estimated standard deviation of 0.001 in the refractive index, and the maximum estimated standard deviation (0.009) determined for the proportion of magnesium in the M(1B) site. Hollow circles = γ, solid circles = β, and triangles = α.

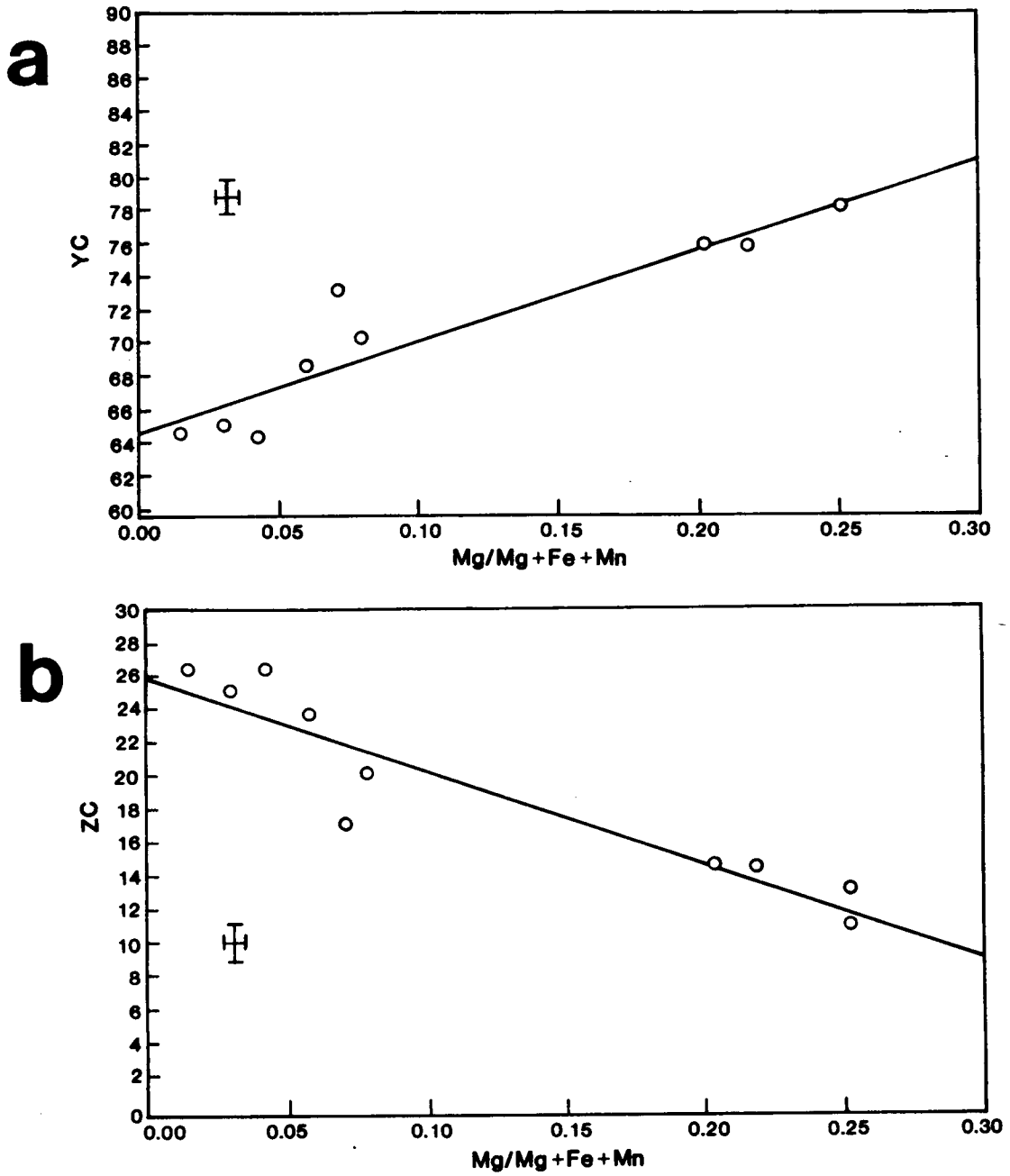

Fig. 3-8. The relationship of optical orientation parameters and the proportion of magnesium in the M(1B) octahedral site of $2M_2$ chloritoid. (a) ∠ Y ^ c* versus Mg/(Mg + Fe + Mn), (b) ∠ Z ^ c* versus Mg(Mg + Fe + Mn). The regression lines correspond to the equations given in Table 3-6. The "esd" symbol represents the highest observed esd (±1°) for the orientation angles, and the maximum esd (±0.009) determined for Mg/(Mg + Fe + Mn).

such that α increases and β decreases due to the "averaging" that occurs in intergrowths containing increasing amounts of the $2M_2$ polytype (Figure 3-11). There is also an increase in $(\gamma - \beta)$ with a corresponding decrease in $(\beta - \alpha)$ as the polytypic composition becomes increasingly monoclinic, accounting for the range of observed optic axial angles ($2V_z$: 34° to 123°) and the change in optic sign (monoclinic is positive, triclinic is negative). The refractive index γ is essentially independent of polytypic composition since Z is close to c^* (the stacking direction) and is therefore hardly affected by intergrowth.

Qualitatively, the orientation angles are more sensitive to variation in polytypic intergrowth than are the refractive indices. Those orientation parameters that have fixed values in $2M_2$ chloritoids are the most responsive to the presence of small amounts of 1Tc chloritoid. For example, X=b in $2M_2$ chloritoids, but the angle between X and b increases rapidly with increased amounts of 1Tc chloritoid (Figure 3-9). Another example would be the sum of the orientation angles $\angle Y \wedge c^*$ and $\angle Z \wedge c^*$. In $2M_2$ chloritoids Y, Z, and c^* are co-planar so that the sum of the orientation angles is 90°. As the amount of 1Tc chloritoid in the composite grain increases X rotates away from b, the YZ-plane rotates away from c^*, and the sum of the orientation angles increases (Figure 3-10). This is a very useful parameter for the estimation of the polytypic composition because it is only slightly dependent on chemical composition, and it can be easily measured using a "360°" spindle stage, a detent spindle stage, or a

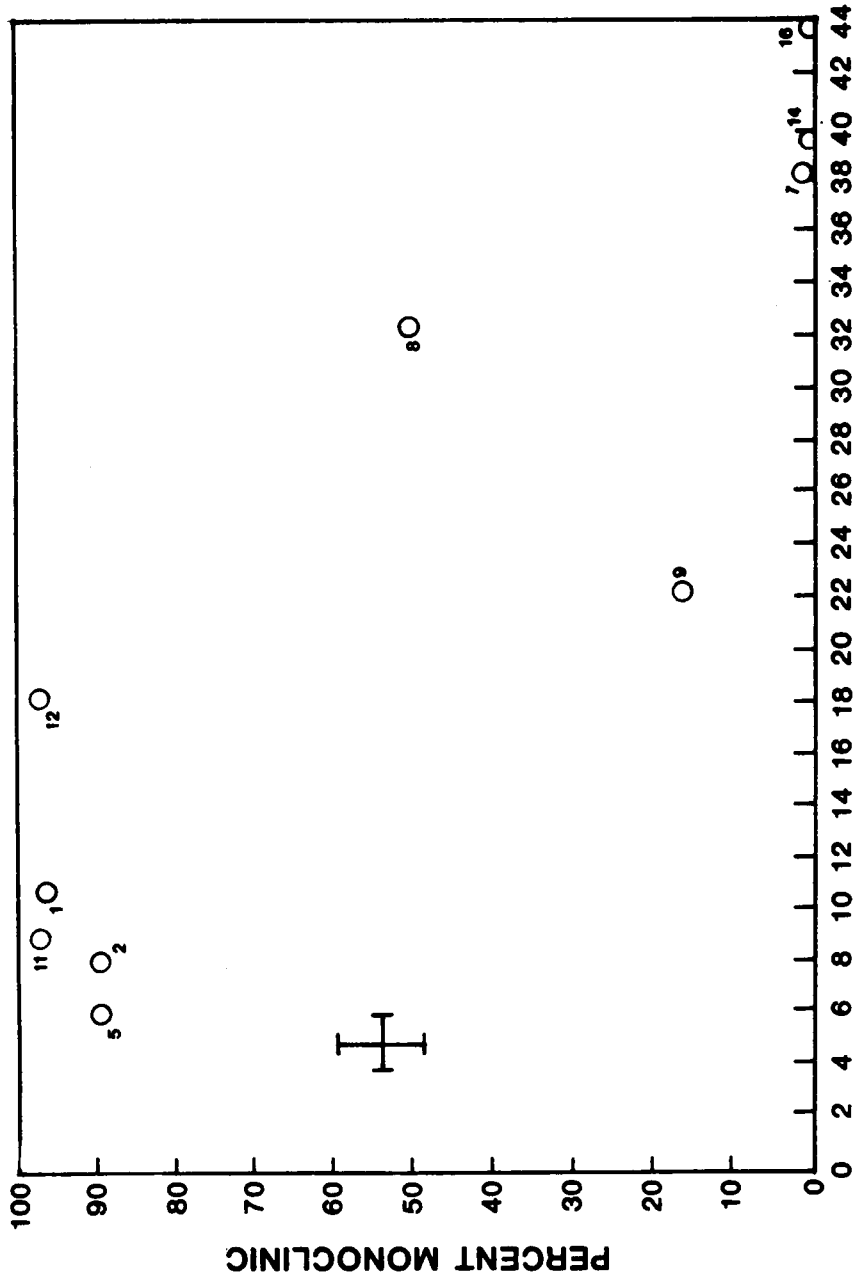

Fig. 3-9. Variation of $\angle X \hat{} b$ with the volume percentage of $2M_2$ chloritoid in the composite grain. The "esd" symbol represents the maximum observed esd for $\angle X \hat{} b$ ($\pm 3^0$) and the percentage of monoclinic chloritoid (~±5%).

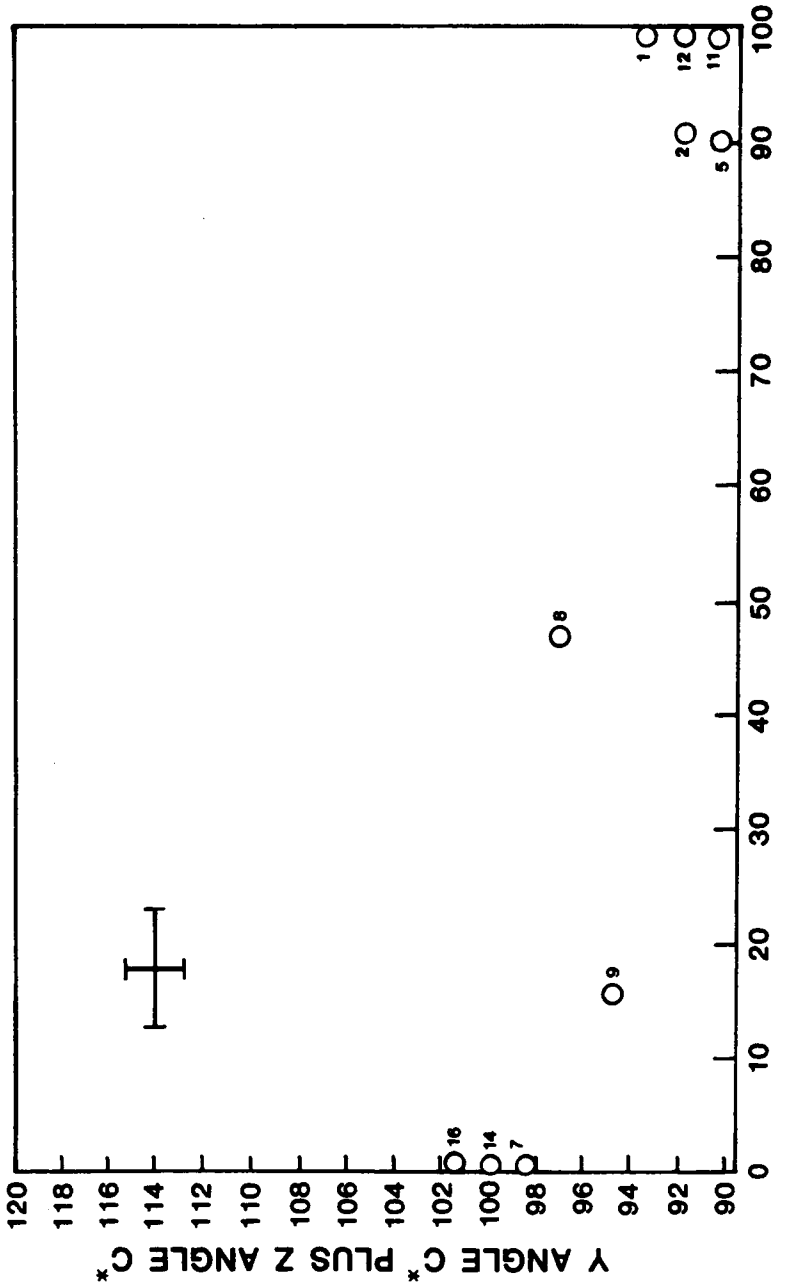

Fig. 3-10. Variation of ($\angle Y \hat{} c^*$) + ($\angle Z \hat{} c^*$) with the volume percentage of $2M_2$ chloritoid in the composite grain. The "esd" symbol represents the maximum observed esd for the sum ($\pm 2^0$) and the percentage of monoclinic chloritoid (~±5%).

universal stage without the use of X-ray diffraction techniques.

The model

To understand the dependence of optical properties on variations in polytypic composition requires the Hauser and Wenk (1976) dielectric tensor calculations described in Chapter One and Appendix A. The only kind of polytypic intergrowth considered in this study is an intergrowth between the 1Tc and $2M_2$ polytypes. The $2M_2$ polytype is assumed to be related to the 1Tc polytype by a 2-fold rotation about [010] with an (001) composition plane. One layer of the 1Tc chloritoid was used as the basic polytype module. The input data consisted of the refractive indices and stereographic coordinates of the principal vibration directions for a 1Tc chloritoid and for its twin-equivalent module (Table 3-7). The optical properties of hypothetical mixtures of 1Tc and $2M_2$ were calculated at intervals of 4% $2M_2$ over the entire range of intergrowth. These calculations were performed using the optical properties of two nearly pure triclinic chloritoids with Mg/(Mg + Fe + Mn) = 0.05 and 0.11. Dominantly monoclinic chloritoids having similar proportions of Mg possess optical properties comparable to those yielded by these calculations (Figure 3-11). Calculations were also performed using the extrapolated optical properties of the pure Fe-$2M_2$ and Fe-1Tc obtained during the compositional correlations mentioned earlier in this discussion.

Graphs illustrating the hypothetical relationships between the

Table 3-7. Dielectric tensor program input parameters for chloritoid.

Domain type	ρ_1	ϕ_1	n_1	ρ_2	ϕ_2	n_2	ρ_3	ϕ_3	n_3
$1Tc_1$	75.63	36.44	1.725	82.02	128.44	1.730	16.52	-113.3	1.732
$1Tc_2$	75.63	143.56	1.725	82.02	51.56	1.730	16.52	-66.7	1.732

Note: ρ and ϕ are the stereographic coordinates of each principle vibration direction. "n" is the refractive index associated with each principal vibration direction.

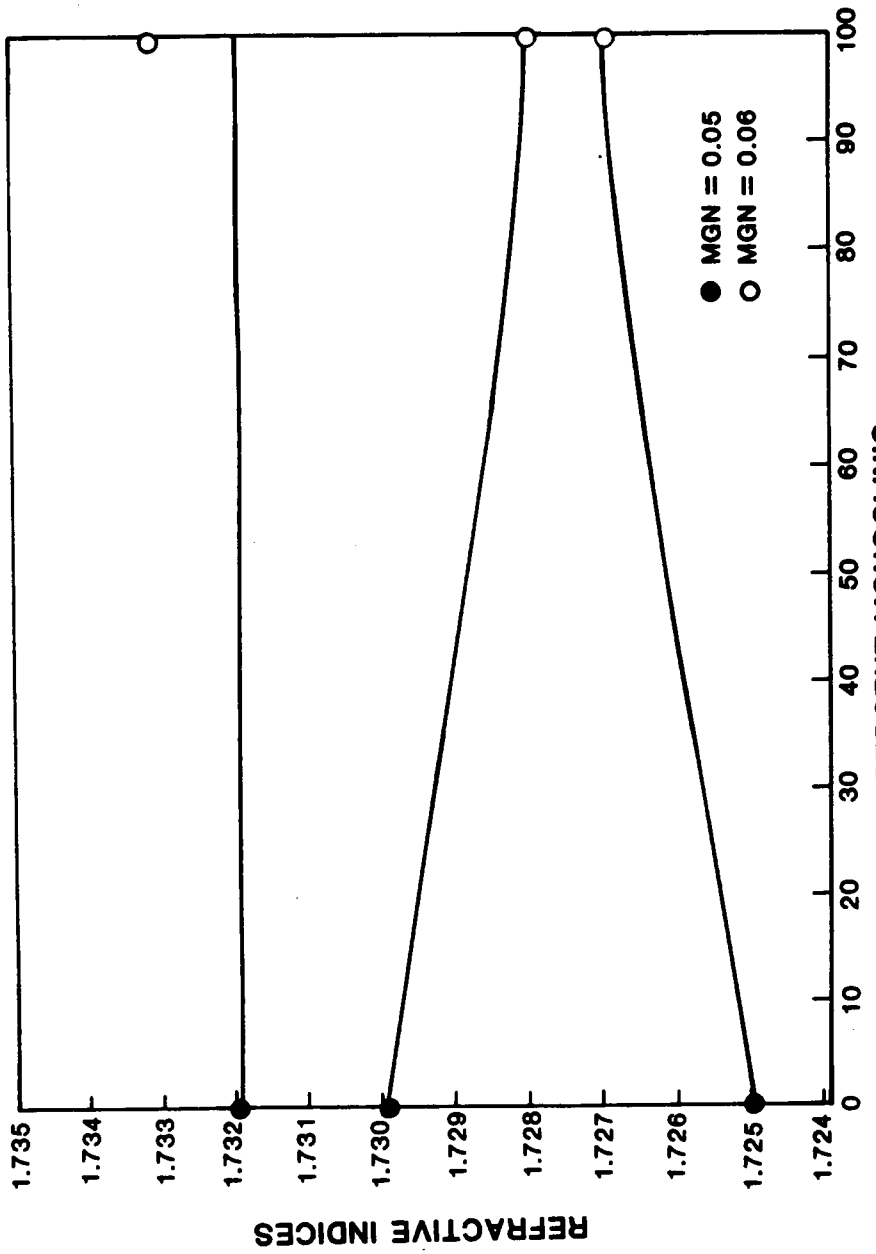

Fig. 3-11. Variation of refractive indices with the volume percentage of $2M_2$ chloritoid in the composite grain. The curves on this plot represent a spline fit to the values calculated with the dielectric tensor program using the data in Table 3-7. The 1Tc parameters used in this model correspond to those of sample 7 with Mg/(Mg + Fe + Mn) or "MGN" = 0.05 (solid dots). The circles represent the refractive indices of an approximately structurally pure $2M_2$ chloritoid, sample 1, with "MGN" = 0.06.

optical properties and the polytypic composition were produced using the SASGRAPH GPLOT procedure (SAS, 1981) and applying a spline fit to the calculated points. Figures 3-12 and 3-13 show the theoretical curves superimposed upon Figures 3-9 and 3-10. The fit of the theoretical curves to the observed data is not perfect but does suggest that these calculations are on the right track. In particular, the calculations confirm the observed sensitivity of the orientation angles to polytypic intergrowth. More data are required in the area of intermediate polytypic composition.

Estimating polytypic composition

The proposed method of estimating the polytypic composition, assuming that the chemical composition and the optical properties are known, requires the use of the correlation equations and theoretical curves established in the previous two sections. Contoured graphs were produced using the SASGRAPH GCONTOUR procedure (Figs. 3-14 and 3-15). These graphs show the form of the determinative curves that could eventually develop. Figure 3-14 illustrates how $\angle X \wedge \underline{b}$ is dependent on the polytypic composition and relatively independent of chemical composition. The data points on this plot are located according to their chemical composition and $\angle X \wedge \underline{b}$. Figure 3-15 illustrates how the sum of the orientation angles $\angle Y \wedge \underline{c}^*$ and $\angle Z \wedge \underline{c}^*$ is primarily dependent upon the polytypic composition, although slightly more dependent on the chemical composition than $\angle X \wedge \underline{b}$. The data points on

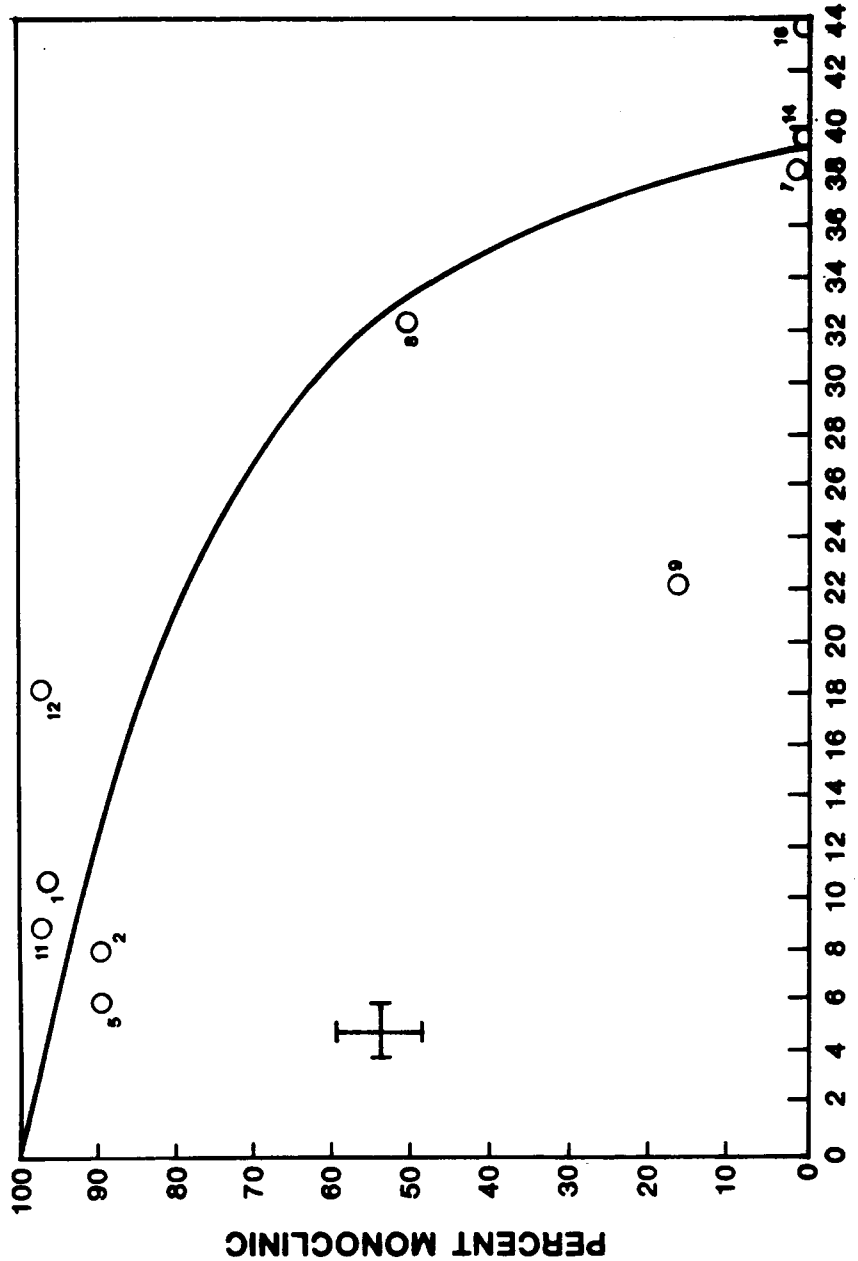

Fig. 3-12. Variation of $\angle X \hat{} b$ with the volume percentage of $2M_2$ chloritoid in the composite grain. The curve is formed by a spline fit to the values calculated with the dielectric tensor program using the data in Table 3-7. The "esd" values are the same as in Fig. 3-9.

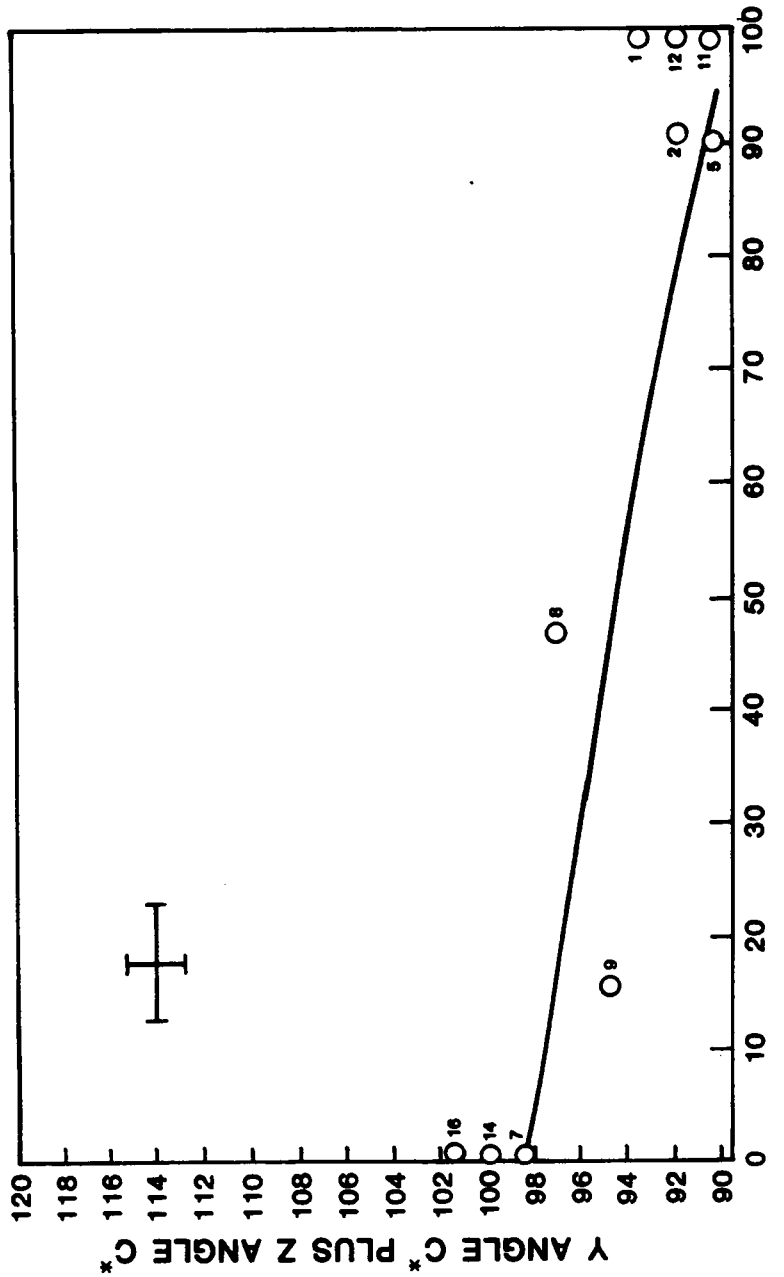

Fig. 3-13. Variation of ($\angle$ Y ^ c*) + ($\angle$ Z ^ c*) with the volume percentage of $2M_2$ chloritoid in the composite grain. The curve is formed by a spline fit to the values calculated with the dielectric tensor program using the data in Table 3-7. The "esd" values are the same as in Fig. 3-10.

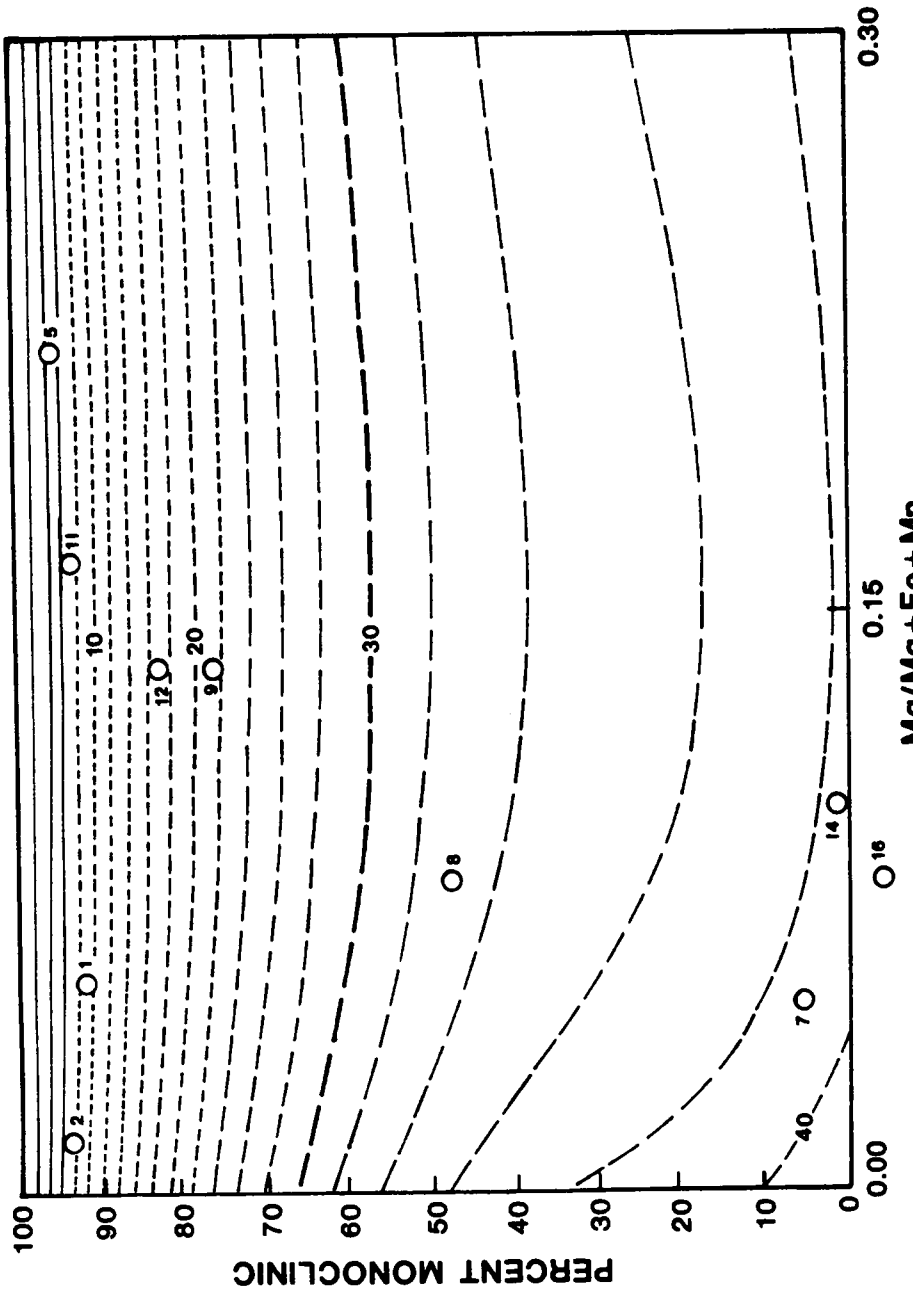

Fig. 3-14. Dependence of $\angle X \hat{} b$ on changes in chemical composition and polytypic composition. The samples are plotted according to the observed $\angle X \hat{} b$ and Mg/(Mg + Fe + Mn) values. The plot is contoured according to $\angle X \hat{} b$, with a contour interval of 2^{0}.

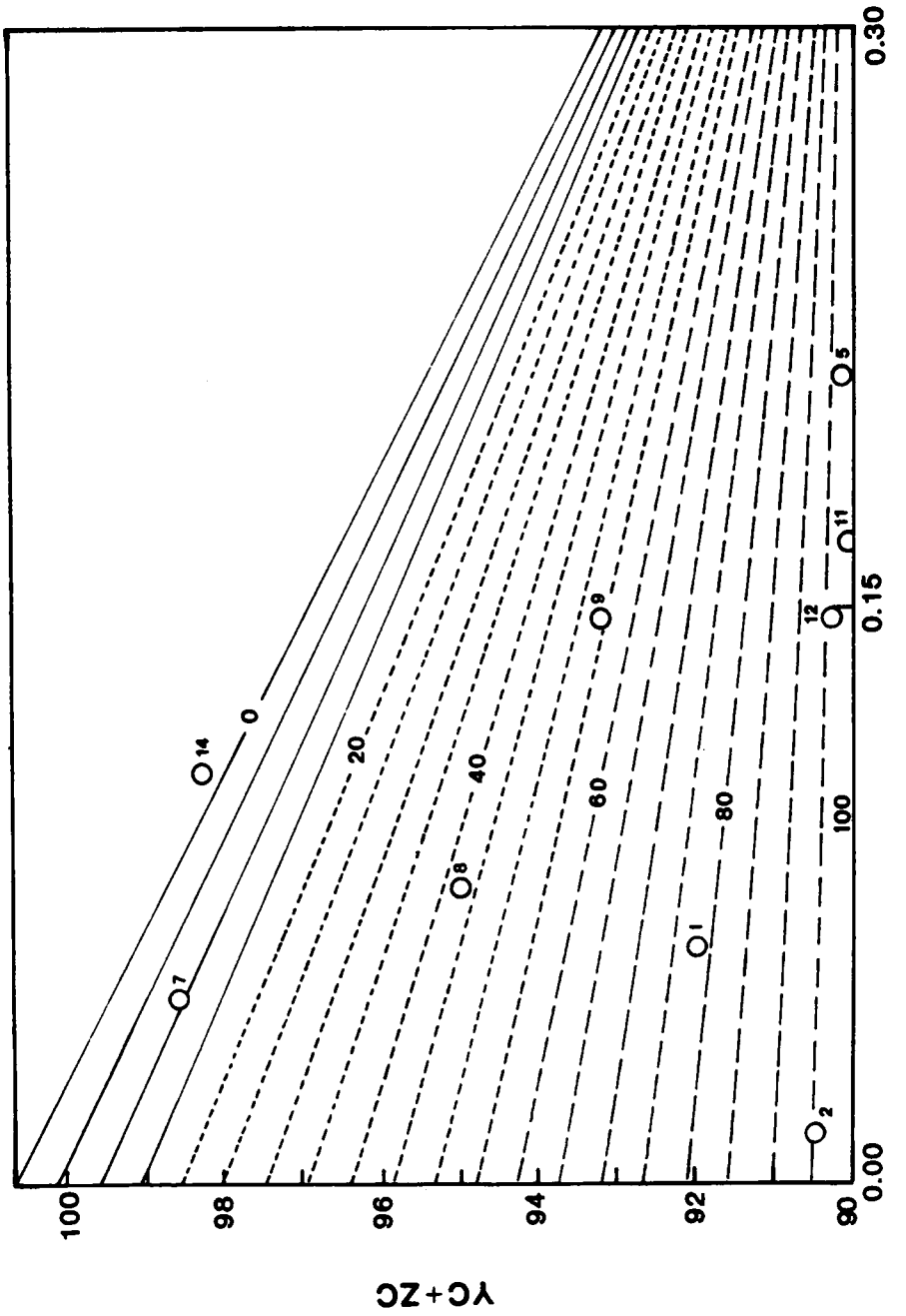

Fig. 3-15. Dependence of ($\angle$ Y ^ c*) + ($\angle$ Z ^ c*) on changes in chemical composition and polytypic composition. The samples are plotted according to the observed ($\angle \overline{Y}$ ^ c*) + ($\angle$ Z ^ c*) and Mg/(Mg + Fe + Mn) values. The plot is contoured according to percentage of $2M_2$ chloritoid, with a contour interval of 5%.

this plot are located according to their chemical composition and the sum of the orientation angles stated above.

The data used to generate these plots are not distributed evenly over the area represented in the plots; therefore, some areas of the plots are extrapolated and are not suitable for determinative purposes. The plots do, however, provide deeper insight into this relationship than has previously been available. They also provide a framework for further investigation of other types of polytypic and compositional effects on the optical properties of the chloritoids.

Summary

This study has developed a stepwise approach to the understanding of the dependence of the optical properties on the variation in both the chemical composition and the polytypic composition. The chloritoids used in the final models are concentrated along the Mg-Fe join and are polytypic intergrowths of the $2M_2$ and 1Tc forms.

First, the dependence of the optical properties on the variation in chemical composition can be determined once the polytypic composition is accounted for. This is best demonstrated by the correlation among the refractive indices and Mg/(Mg + Fe + Mn) values of $2M_2$ chloritoids. Halferdahl (1961) and Deer et al. (1981) did not find a quantitative correlation between the chemical composition and the refractive indices due most likely to the lack of consideration of the effects of the polytypic intergrowth.

Second, the optical orientation is very sensitive to small variations in the polytypic composition, especially orientation angles that have fixed values in $2M_2$ chloritoid. The first accurate determinations of the optical orientations of predominantly triclinic chloritoids are necessary for the understanding of the sensitivity of the optical orientations to polytypic intergrowth.

Third, the effects can be modeled using dielectric tensors which provide a physically meaningful interpretation of the observed trends. The model assumed that the $2M_2$ polytype can be formed by twinning the 1Tc polytype by a 2-fold rotation about [100] with an (001) composition plane. The general agreement of the observed relationships with the calculated relationships indicates that the model is representative of what is physically occurring. For example, both the observed data and the dielectric tensor calculations demonstrated the sensitivity of the optical orientation to variations in the polytypic composition.

A set of graphs have been constructed and presented that can be used to estimate the polytypic composition if the optical orientation and chemical composition are known. More data are required before the effects of other intergrowths, such as 1Tc and 2M1, 2M1 and 2M2, or 1Tc, 2M1, and 2M2, on the optical properties can be determined. Chloritoids having chemical compositions beyond the range studied here must be examined to extend the determinative capabilities of the plots shown in this chapter.

Ultimately, these plots will make it possible to estimate the polytypic composition and chemical composition with optical and X-ray

data. The polytypic composition could be determined with optical and chemical data. This approach has the potential of improving our understanding of polytypism in the chloritoids.

REFERENCES

Akizuki, M. (1970) Slip structure of heated sphalerite. American Mineralogist, 55, 1302-1312.

Akizuki, M. (1981) Investigation of phase transition of natural ZnS minerals by high resolution electron microscopy. American Mineralogist, 66, 1006-1012.

Akizuki, M. (1983) Investigation of phase transition of natural ZnS minerals by high resolution electron microscopy: reply. American Mineralogist, 68, 847-848.

Bailey, S.W. (1977) Report of the I.M.A.-I.U.Cr. joint committee on nomenclature. American Mineralogist, 62, 411-415.

Bence, A.E. and Albee, A.L. (1968) Empirical correction factors for the electron microanalysis of silicates and oxides. Journal of Geology, 76, 382-403.

Bloss, F.D. (1978) The spindle stage: a turning point for optical crystallography. American Mineralogist, 63, 433-447.

Bloss, F.D. (1981) The spindle stage: principles and practice. Cambridge University Press, Cambridge, England, 340 p.

Bloss, F.D. and Riess, D. (1973) Computer determination of 2V and indicatrix orientation from extinction data. American Mineralogist, 58, 1052-1061.

Bloss, F.D., Gunter, M., Su, S-C. and Wolfe, H.E. (1983) Gladstone-Dale constants: a new approach. Canadian Mineralogist, 21, 93-99.

Colby, J.W. (1971) MAGIC IV, a computer program for quantitative electron microprobe analysis. Bell Telephone Laboratories, Allentown, Pennsylvania.

Brindley, G.W. and Harrison, F.W. (1952) The structure of chloritoid. Acta Crystallographica, 5, 698-699.

Deer, W.A., Howie, R.A. and Zussman, J. (1981) Rock forming minerals: Vol. 1A, Orthosilicates (2nd edition). Longman, London.

De Grave, E., Vanleerberghe, R., Verdonck, L. and De Geyter, G. (1984) Mössbauer and infrared spectroscopic studies of Belgian Chloritoids. Physics and Chemistry of Minerals, 11, 85-94.

Faye, G.E., Manning, P.G. and Nickel, E.H. (1968) The polarized optical absorption spectra of tourmaline, cordierite, chloritoid and vivianite: ferrous-ferric electronic interaction as a source of pleochroism. American Mineralogist, 53, 1174-1201.

Fleet, M.E. (1977a) Structural transformations in natural ZnS. American Mineralogist, 62, 540-546.

Fleet, M.E. (1977b) The birefringence-structural state relation in natural zinc sulfides and its application to a schalenblende from Pribram. Canadian Mineralogist, 15, 303-308.

Fleet, M.E. (1983) Investigation of phase transition of natural ZnS minerals by high resolution electron microscopy: discussion. American Mineralogist, 68, 845-846.

Foley, N. (1980) Mineralogy and geochemistry of the Austinville-Ivanhoe district, Virginia. M.S. thesis, Virginia Polytechnic Institute and State Univeristy, Blacksburg, Virginia.

Foster, M.D. (1961) A critical review of analyses of chloritoid. U.S. Geological Survey Professional Paper 424-C, 306-309.

Fransolet, A-M., (1978) Données nouvelles sur l'ottrelite d'Ottré, Belgique. Bulletin de Minéralogie, 101, 548-557.

Geilikman, M.B. (1982) Mechanisms of polytype stabilization during the wurtzite-sphalerite transition. Physics and Chemistry of Minerals, 8, 2-7.

Hålenius, U. and Langer, K. (1980) Microscope-photometric methods for non-destructive Fe^{2+}-Fe^{3+} determination in chloritoids $(Fe^{2+},Mn^{2+},Mg)_2(Al,Fe^{3+})_4Si_2O_{10}(OH)_4$. Lithos, 13, 291-294.

Hålenius, U., Annersten, H. and Langer, K. (1981) Spectroscopic studies on natural chloritoids. Physics and Chemistry of Minerals, 7, 117-123.

Halferdahl, L.B. (1961) Chloritoid: its composition, X-ray and optical properties, stability and occurrence. Journal of Petrology, 2, 49-135.

Hanscom, R.H. (1975) Refinement of the crystal structure of monoclinic chloritoid. Acta Crystallographica, B31, 780-784.

Hanscom, R.H. (1980) The structure of triclinic chloritoid and chloritoid polymorphism. American Mineralogist, 65, 534-539.

Harrison, F.W. and Brindley, G.W. (1957) The crystal structure of chloritoid. Acta Crystallographica, 10, 77-82.

Hauser, J. and Wenk, H.-R. (1976) Optical properties of composite crystals (submicroscopic domains, exsolution lamellae, solid solutions). Zeitschrift für Kristallographie, 143, 188-219.

Helwig, J.T. and Council, K.A., eds. (1979) SAS User's Guide. SAS Institute Inc., Cary, North Carolina.

Hietanen, A. (1951) Chloritoid from Rawlinsville, Lancaster County, Pennsylvania. American Mineralogist, 36, 859-868.

Hurlbut, C.S. (1957) The wurtzite-greenockite series. American Mineralogist, 42, 184-190.

Jagodzinski, H. (1949) Eindimensionale Fehlordung in Kristallen und ihr Einfluss auf die Röntgeninterferenzen. I. Berechnung des Fehlordnungsgradesaus den Röntgenintensitäten. Acta Crystallographica, 2, 201-207.

Jefferson, D.A. and Thomas, J.M. (1977) Structural variation in chloritoid. E.C.M.-4 Proceedings (Oxford), 626-628.

Jefferson, D.A. and Thomas, J.M. (1978) High resolution electron microscopic and X-ray studies of non-random disorder in an unusual layered silicate (chloritoid). Proceedings of the Royal Society of London, A361, 399-411.

Lasaga, A.C. and Cygan, R.T. (1982) Electronic and ionic polarizabilities of silicate minerals. American Mineralogist, 67, 328-334.

Lindblom, S. (1980) Textural evidence of deformation in the Laisvall ore. In ORG-80, Annual Report of the Ore Research Group, Stockholm University, D. Rickard (Ed.).

Mandarino, J.A. (1976) The Gladstone-Dale relationship - Part I: Derivation of new constants. Canadian Mineralogist, 14, 498-502.

Mandarino, J.A. (1978) The Gladstone-Dale relationship - Part II: Trends among constants. Canadian Mineralogist, 16, 169-174.

Mandarino, J.A. (1979) The Gladstone-Dale relationship - Part III: Some general applications. Canadian Mineralogist, 17, 71-76.

Mandarino, J.A. (1981) The Gladstone-Dale relationship - Part IV: The compatibility concept and its application. Canadian Mineralogist, 19, 441-450.

Nelkowski, H. and Pfützen-Reuter, O. (1971) Kristallstruktur und Doppelbrechung fehlgeordneter ZnS einkristalle. Acta Crystallographica, A27, 296-298.

Pauling, L. (1945) Nature of the chemical bond. Cornell University Press, Ithaca, New York.

Plas, L. van der, Hügi, T., Mladeck, M.H., and Niggli, E. (1958) Chloritoid vom Hennensädel südlich Vals (nördliche Aduladecke). Schweizerische mineralogische und petrographische Mitteilungen, 38, 237-246.

Ramsdell, L.S. (1947) Studies on silicon carbide. American Mineralogist, 32, 64-82.

Ribbe, P.H. (1982) Chloritoid. Mineralogical Society of America Reviews in Mineralogy, 5, 155-169.

Roedder, E. (1968a) Temperature, salinity and origin of the ore-forming fluids at Pine(?) Point, Northwest Territories, Canada, from fluid inclusion studies. Economic Geology, 63, 439-450.

Roedder, E. (1968b) The noncolloidal origin of colloform textures in sphalerite ores. Economic Geology, 63, 451-471.

Scott, S.D. (1974) Experimental methods in sulfide synthesis. Mineralogical Society of America Reviews in Mineralogy, 1, p. S-1 - S-38.

Seal, R.R., II, Cooper, B.J. and Craig, J.R. (1985) Anisotropic sphalerite of the Elmwood-Gordonsville deposits, Tennessee. Canadian Mineralogist, 23, 83-88.

Solberg, T.N. and Speer, J.A. (1982) QALL, a 16-element analytical scheme for efficient petrologic work on an automated ARL-SEMQ: Application to mica reference samples. In K.F.J. Heinrich, Ed., Microbeam Analysis, p. 422-426, San Francisco Press, Inc., San Francisco.

Steinberger, I.T., Kiflawi, I., Kalman, Z.H. and Mardix, S. (1973) The stacking faults and partial dislocations in structure transformations of ZnS crystals. Philosophical Magazine, 27, 159-175.

Su, S.-C., Bloss, F.D. and Gunter, M. (1987) Procedures and computer programs to refine the double variation method. American Mineralogist, 72, 1011-1013.

Thompson, J.B.,Jr. (1981) Polytypism in complex crystals: contrasts between mica and classical polytypes. In Structure and Bonding in Crystals, Vol. II, p. 167-196, Academic Press, Inc., New York.

Tricker, M.J., Jefferson, D.A., Thomas, J.M., Manning, P.G. and Elliot, C.J. (1978) Mossbauer and analytical electron microscopic studies of an unusual orthosilicate: chloritoid. Journal of the Chemical Society Faraday Transactions II, 74, 174-181.

Verma, A. R. and Krishna, P. (1966) Polymorphism and polytypism in crystals. John Wiley and Sons, Inc., New York, New York.

Winchell, A.N. and Winchell, H. (1964) The Microscopical Characters of Artificial Inorganic Solid Substances: optical properties of Artificial Minerals. Academic Press, New York.

Wyckoff, R.W.G. (1948) Crystal Structures, Vol. I. Interscience Publishers, New York, New York.

APPENDIX A

A USER'S GUIDE FOR THE HAUSER-WENK PROGRAM

Introduction

This computer program was originally coded by Hauser and Wenk (1976). The program is used to calculate the optical properties of submicroscopically composite minerals using dielectric tensors. The theory behind the program is discussed in Hauser and Wenk (1976) and reviewed in Chapter One. Basically, the program is used to create a composite dielectric tensor, and subsequently decompose that tensor to give the refractive indices and the stereographic coordinates of the principal vibration directions.

The required input data include the refractive indices and stereographic coordinates of the principal vibration directions of each end member domain to be considered in the composite grain, and the volume fraction of each domain type in the composite grain (Table A-1).

The output has the general form shown in Table A-2. The volume fractions that were input, the refractive indices, stereographic coordinates of the principal vibration directions, the birefringence, the 2V, Euler angles of the indicatrix, and Goldschmidt angles of the optic axes are included in the printout. The last two parameters were used by Hauser and Wenk (1976) but were not used in the present study.

The following is a section-by-section description of the program defining the variables and stating what processes are taking place in

each part of the program. Please refer to the program listing that follows this description.

Section One: lines 1 through 19

This portion of the program defines and initializes the variables and arrays to be used in the program.

A(3,3) = the composite dielectric tensor

EIVU(3) = eigenvalues

EIVR(3) = eigenvectors

AR(3), BR(3), and GR(3) = vectors along the composite principal vibration directions.

E(6,3,3) = the dielectric tensors for up to 6 domains

R(3) = the ρ stereographic coordinate for the principal directions

P(3) = the ϕ stereographic coordinate for the principal directions

AL(3) = the three principal refractive indices

F(6) = the volume fractions of up to 6 domains

DOMTYP = a name for each specific domain type

T = 0.0174532925 = $\pi/180$ (degree to radian conversion)

Section Two: lines 20 through 100

In this portion of the program the indicatrix of each domain is

read into memory and processed (Table A-1). The first line of the input data includes the name of the domain type (columns 1-8), the stereographic coordinates, and refractive indices for each principal vibration direction (nine F7.5 regions). The second line of output for each domain type contains the 2V (columns 11-16). The "-1." at the end of the first part of the input is a flag indicating the end of the optical data.

After the optical data are input the program uses the 2V to decide whether to treat the data as uniaxial or biaxial, and checks the 2V by calculating it from the refractive indices (lines 27-38). The first write statement writes the titles and the second write statement writes the input data (Table A-2). The input data are orthogonalized (lines 47-78) to insure that the stereographic coordinates represent mutually perpendicular principal vibration directions. The third write statement writes the orthogonalized values of the input data immediately beneath the observed values (Table A-2).

This section ends with the calculation of the dielectric tensors of the individual domain types based upon the input data.

Section Three: lines 101 through 132

At this point in the program the volume fractions, and stereographic coordinates of the normal to the interface between the first two domains are read into memory. The normal is often specified as the z Cartesian axis and need not be stated. The volume fraction of

the first domain listed in the first section is typed in columns 1-10, the second domain in columns 11-20, etc. This part of the input is terminated with two flags, the second of which indicates the end of the entire data set. The matrix A is initialized to zero (lines 104-106), then the composite dielectric tensor is created (lines 108-113). The case where the interface is not perpendicular to z is treated in lines 114 through 132.

The Call Statement

The "CALL EA06C" statement on line 133 calls a subroutine package (lines 267-514) taken from the set of IMSL subroutines in the VPI&SU IMSL LIBRARY (original Hauser-Wenk program uses Harwell subroutines). This set of subroutines is used to calculate the eigenvalues and eigenvectors of the composite dielectric tensor.

Section Four: lines 134 through 266

This section takes the eigenvalues and eigenvectors sent back to the main program by the subroutines, and calculates the refractive indices (lines 142-143), determines which is α, β, and γ (lines 144-175), and gives the coordinates of the principal vibration directions associated with each refractive index (lines 199-227). Other calculated parameters include the 2V (lines 181-189), the Euler angles of the indicatrix (lines 233-240), the Goldschmidt angles of the optic axes (lines

244-258), and the Goldschmidt angles of the normal to the interface if that was specified in the input. The output is shown in Table A-2.

Table A-1. Input data for the dielectric tensor program

```
   TRI1    76.      30.    1.727    89.00 120.00 1.728   14.00     240.0 1.731
           60.
   TRI2    76.      90.    1.727    89.00 180.00 1.728   14.00     300.0 1.731
           60.
   TRI3    76.     150.    1.727    89.00 240.00 1.728   14.00       0.0 1.731
           60.
   TRI4    76.     210.    1.727    89.00 300.00 1.728   14.00      60.0 1.731
           60.
   TRI5    76.     270.    1.727    89.00   0.00 1.728   14.00     120.0 1.731
           60.
   TRI6    76.     330.    1.727    89.00  60.00 1.728   14.00     180.0 1.731
           60.
           -1.
1.0        0.0       0.0       0.0       0.0       0.0
0.0        1.0       0.0       0.0       0.0       0.0
0.0        0.0       1.0       0.0       0.0       0.0
0.0        0.0       0.0       1.0       0.0       0.0
0.0        0.0       0.0       0.0       1.0       0.0
0.0        0.0       0.0       0.0       0.0       1.0
0.5        0.0       0.0       0.0       0.0       0.5
0.5        0.0       0.5       0.0       0.0       0.0
0.166666670.166666670.166666670.166666670.166666670.16666665
0.333333340.0        0.333333330.0        0.333333330.0
0.0        0.333333340.0        0.333333330.0        0.33333333
0.0        0.5       0.0       0.0       0.5       0.0
0.0        0.0       0.5       0.5       0.0       0.0
0.0        0.0       0.0       0.0       0.0       0.5
0.0        0.0       0.0       0.5       0.5       0.0
0.5        0.0       0.0       0.0       0.0       0.5
           -1.
           -2.
```

Note: This is an actual printout of the data file. The first 12 lines are the domain types (first column), ρ and ϕ stereographic coordinates (columns 2, 3, 5, 6, 8, and 9), refractive indices (columns 4, 7, and 10), and the 2V on the second line of each pair of lines. The "-1." on line 13 is a flag indicating the end of the indicatrix data. The six-column lines following this flag are the volume fractions of each domain type in each composite crystal. The last two lines are flags indicating the end of the volume fraction data and the end of all of the data.

Table A-2. Output produced by the dielectric tensor program

INPUT PARAMETERS FIRST LINE IS DIRECT INPUT SECOND LINE IS ORTHOGONALIZED

DOMAIN	RHO(1)	PHI(1)	N(1)	RHO(2)	PHI(2)	N(2)	RHO(3)	PHI(3)	N(3)	2V
TRI1	76.00	30.00	1.7270	89.00	120.00	1.7280	14.00	240.00	1.7310	60.00
TRI1	76.00	30.00	1.7270	89.06	120.23	1.7280	14.03	214.00	1.7310	60.09
TRI2	76.00	90.00	1.7270	89.00	180.00	1.7280	14.00	300.00	1.7310	60.00
TRI2	76.00	90.00	1.7270	89.06	180.23	1.7280	14.03	274.00	1.7310	60.09
TRI3	76.00	150.00	1.7270	89.00	240.00	1.7280	14.00	0.0	1.7310	60.00
TRI3	76.00	150.00	1.7270	89.06	240.23	1.7280	14.03	334.00	1.7310	60.09
TRI4	76.00	210.00	1.7270	89.00	300.00	1.7280	14.00	60.00	1.7310	60.00
TRI4	76.00	210.00	1.7270	89.06	300.23	1.7280	14.03	34.00	1.7310	60.09
TRI5	76.00	270.00	1.7270	89.00	0.0	1.7280	14.00	120.00	1.7310	60.00
TRI5	76.00	270.00	1.7270	89.06	0.23	1.7280	14.03	94.00	1.7310	60.09
TRI6	76.00	330.00	1.7270	89.00	60.00	1.7280	14.00	180.00	1.7310	60.00
TRI6	76.00	330.00	1.7270	89.06	60.23	1.7280	14.03	154.00	1.7310	60.09

```
VOLUME FRACTIONS        1.000  0.0     0.0     0.0     0.0     0.0

        RHO         PHI             N       BIREFRINGENCE
A     75.99622     29.99997      1.72700   (B-A) = 0.00100
B     89.05697    120.23514      1.72800   (G-B) = 0.00300
G     14.03680    214.01013      1.73100   (G-A) = 0.00400
2V=    60.08612

EULER ANGLES OF INDICATRIX
  THETA=  75.99622PHI= 209.99997PSI=   1.33301
GOLDSCHMIDT ANGLES OF OPTIC AXES   RHO(1),PHI(1),RHO(2),AND PHI(2)          16.06434  26.95832  44.05679 211.20990

VOLUME FRACTIONS        0.0     1.000  0.0     0.0     0.0     0.0

        RHO         PHI             N       BIREFRINGENCE
A     75.99572     90.03073      1.72700   (B-A) = 0.00100
B     89.06658    180.26356      1.72800   (G-B) = 0.00300
G     14.03663    273.99980      1.73100   (G-A) = 0.00400
2V=    60.08613

EULER ANGLES OF INDICATRIX
  THETA=  75.99572PHI= 270.03073PSI=   1.29408
GOLDSCHMIDT ANGLES OF OPTIC AXES   RHO(1),PHI(1),RHO(2),AND PHI(2)          16.06333  87.02007  44.05710 271.22826
```

Note: This is an actual printout of the output file. The top portion includes the input data before and after orthogonalization. The other two sections shown here represent the kind of information output for each composite grain.

PROGRAM LISTING

```
      IMPLICIT REAL*8(A-H,O-Z)
      DIMENSION A(3,3),EIVU(3),EIVR(3,3),U(3),AR(3),BR(3),GR(3)
      DIMENSION E(6,3,3),R(3),P(3),AL(3),SR(3),SP(3),CR(3),CP(3),D(3),
     1F(6),AA(3),BB(3),UN(3),Q(3),QQ(3,3)
      DIMENSION DOMTYP(2),WK(20)
      REAL*8 LL,LLL
      DO 5 K=1,20
      WK(K)=0.0000
    5 CONTINUE
      T=0.0174532925
      IX=3
      NDIM=3
      N=3
   10 NUM=0
      DO 15 I1=1,6
      DO 15 I2=1,3
      DO 15 I3=1,3
      E(I1,I2,I3)=0.
   15 CONTINUE
   20 READ(5,22)DOMTYP,R(1),P(1),AL(1),R(2),P(2),AL(2),R(3),P(3),AL(3)
   22 FORMAT(2A4,2X,9F7.5)
      IF(R(1).EQ.-2.) STOP
      IF(R(1).EQ.-1.) GO TO 90
   24 READ(5,26)TVOBS
   26 FORMAT(10X,F6.3)
      NUM=NUM+1
      IF(AL(2).EQ.0.) GO TO 40
      IF(AL(2).EQ.AL(3)) GO TO 35
      Z=DSQRT((1./AL(1)**2.-1./AL(2)**2.)/(1./AL(2)**2.-1./AL(3)**2.))
      TV=2.*DATAN(Z)
      GO TO 45
   35 TV=0.
      GO TO 45
   40 TV=TV*T
      AL(2)=DSQRT((1.+DTAN(TV/2.)*DTAN(TV/2.))/(1./(AL(1)**2.)+DTAN(TV/
     12.)*DTAN(TV/2.)/(AL(3)**2.)))
   45 CONTINUE
      TV=TV/T
      IF(NUM.EQ.1) WRITE(6,50)
   50 FORMAT(1H1,24X,'INPUT PARAMETERS    FIRST LINE IS DIRECT INPUT   S
     1ECOND LINE IS ORTHOGONALIZED'//3X,6HDOMAIN,4X,6HRHO(1),6X,6HPHI(1)
     2,6X,4HN(1),8X,6HRHO(2),6X,6HPHI(2),6X,4HN(2),8X,6HRHO(3),6X,6HPHI(
     33),6X,4HN(3),9X,2HV)
      WRITE(6,55)DOMTYP,R(1),P(1),AL(1),R(2),P(2),AL(2),R(3),P(3),AL(3)
     1,TVOBS
   55 FORMAT(/,1X,2A4,2X,3(2(F7.2,5X),F7.4,5X),F7.2)
      U1=DSIN(R(1)*T)*DSIN(P(1)*T)
      U2=DSIN(R(1)*T)*DCOS(P(1)*T)
      U3=DCOS(R(1)*T)
      V1=DSIN(R(2)*T)*DSIN(P(2)*T)
      V2=DSIN(R(2)*T)*DCOS(P(2)*T)
```

```
      V3=DCOS(R(2)*T)
      T1=U2*V3-U3*V2
      T2=U3*V1-U1*V3
      T3=U1*V2-U2*V1
      S1=T2*U3-T3*U2
      S2=T3*U1-T1*U3
      S3=T1*U2-T2*U1
      LL=DSQRT(T1*T1+T2*T2+T3*T3)
      T1=T1/LL
      T2=T2/LL
      T3=T3/LL
      LLL=DSQRT(S1*S1+S2*S2+S3*S3)
      S1=S1/LLL
      S2=S2/LLL
      S3=S3/LLL
      R(2)=DARCOS(S3)/T
      P(2)=DATAN2(S1,S2)/T
      R(3)=DARCOS(T3)/T
      P(3)=DATAN2(T1,T2)/T
      DO 60 I=2,3
   60 IF(P(I).LT.0.) P(I)=360.+P(I)
      DO 65 I=2,3
      IF(R(I).EQ.0.) P(I)=0.0
      IF(R(I).GT.90.) P(I)=180.+P(I)
      IF(R(I).GT.90.) R(I)=180.-R(I)
   65 IF(P(I).GT.360.) P(I)=P(I)-360.
      WRITE(6,70)DOMTYP,R(1),P(1),AL(1),R(2),P(2),AL(2),R(3),P(3),AL(3)
     1,TV
   70 FORMAT(1X,2A4,2X,3(2(F7.2,5X),F7.4,5X),F7.2)
      DO 75 I=1,3
      SR(I)=DSIN(R(I)*T)
      CR(I)=DCOS(R(I)*T)
      SP(I)=DSIN(P(I)*T)
      CP(I)=DCOS(P(I)*T)
   75 D(I)=AL(I)**2.
      DO 80 K=1,3
      E(NUM,1,1)=E(NUM,1,1)+D(K)*SR(K)*SR(K)*SP(K)*SP(K)
      E(NUM,1,2)=E(NUM,1,2)+D(K)*SR(K)*SR(K)*SP(K)*CP(K)
      E(NUM,1,3)=E(NUM,1,3)+D(K)*SR(K)*CR(K)*SP(K)
      E(NUM,2,1)=E(NUM,1,2)
      E(NUM,2,2)=E(NUM,2,2)+D(K)*SR(K)*SR(K)*CP(K)*CP(K)
      E(NUM,2,3)=E(NUM,2,3)+D(K)*SR(K)*CR(K)*CP(K)
      E(NUM,3,1)=E(NUM,1,3)
      E(NUM,3,2)=E(NUM,2,3)
      E(NUM,3,3)=E(NUM,3,3)+D(K)*CR(K)*CR(K)
   80 CONTINUE
      GO TO 20
   90 CONTINUE
  100 READ (5,101)F(1),F(2),F(3),F(4),F(5),F(6),RN,PN
  101 FORMAT(8F10.5)
      IF(F(2).EQ.-1.) GO TO 10
      DO 105 JJ=1,3
      DO 105 JJJ=1,3
      A(JJ,JJJ)=0.
  105 CONTINUE
```

```
109          DO 110 J1=1,NUM
110          DO 110 J2=1,3
111          DO 110 J3=1,3
112          A(J2,J3)=A(J2,J3)+F(J1)*E(J1,J2,J3)
113      110 CONTINUE
114          IF(RN.EQ.0..AND.PN.EQ.0.) GO TO 150
115          UN(1)=DSIN(RN*T)*DSIN(PN*T)
116          UN(2)=DSIN(RN*T)*DCOS(PN*T)
117          UN(3)=DCOS(RN*T)
118          DO 115 I=1,3
119      115 Q(I)=0.
120          DO 120 I=1,3
121          DO 120 J=1,3
122      120 Q(I)=Q(I)+(E(1,I,J)-E(2,I,J))*UN(J)
123          DO 125 I=1,3
124          DO 125 J=1,3
125      125 QQ(I,J)=Q(I)*Q(J)
126          BO=0.
127          DO 130 I=1,3
128          DO 130 J=1,3
129      130 BO=BO+UN(I)*(F(1)*E(2,I,J)+F(2)*E(1,I,J))*UN(J)
130          DO 135 I=1,3
131          DO 135 J=1,3
132      135 A(I,J)=A(I,J)-F(1)*F(2)*QQ(I,J)/BO
133      150 CALL EA06C(A,EIVU,EIVR,N,NDIM,IX,WK)
134          DO 166 J=1,3
135          XX=DSQRT(EIVR(1,J)**2+EIVR(2,J)**2+EIVR(3,J)**2)
136          DO 160 I=1,3
137      160 EIVR(I,J)=EIVR(I,J)/XX
138          IF(EIVR(3,J))162,166,166
139      162 DO 164 I=1,3
140      164 EIVR(I,J)=-EIVR(I,J)
141      166 CONTINUE
142          DO 168 I=1,3
143      168 U(I)=DABS(EIVU(I))
144          IF(U(1)-U(2))200,210,210
145      200 IF(U(3)-U(2))220,240,240
146      210 IF(U(3)-U(1))230,250,250
147      220 IF(U(3)-U(1))260,270,270
148      230 IF(U(3)-U(2))280,290,290
149      240 N1=1
150          N2=2
151          N3=3
152          GO TO 300
153      250 N1=2
154          N2=1
155          N3=3
156          GO TO 300
157      260 N1=3
158          N2=1
159          N3=2
160          GO TO 300
161      270 N1=1
162          N2=3
163          N3=2
```

```
      GO TO 300
280   N1=3
      N2=2
      N3=1
      GO TO 300
290   N1=2
      N2=3
      N3=1
300   AS=U(N1)
      BS=U(N2)
      GS=U(N3)
      DO 305 I=1,3
      AR(I)=EIVR(I,N1)
      BR(I)=EIVR(I,N2)
      GR(I)=EIVR(I,N3)
305   CONTINUE
      IF(GS-BS)310,310,312
310   W=0.0
      A1=0.0
      A2=0.0
      A3=90.0
      GO TO 314
312   Z=DSQRT((GS*(BS-AS))/(AS*(GS-BS)))
      VV=2.*DATAN(Z)
      W=VV/T
      A1=DATAN2(BR(1),-BR(2))/T
      A2=DARSIN(BR(3))/T
      XXX=(-BR(2)*AR(1)+BR(1)*AR(2))/DSQRT(BR(1)**2+BR(2)**2)
      A3=DARCOS(XXX)/T
314   C1=DSQRT(AS)
      C2=DSQRT(BS)
      C3=DSQRT(GS)
      WRITE(6,320)F(1),F(2),F(3),F(4),F(5),F(6)
320   FORMAT(//' VOLUME FRACTIONS',5X,6F7.3/)
      RA=DARCOS(AR(3))/T
      RB=DARCOS(BR(3))/T
      RG=DARCOS(GR(3))/T
      IF(AR(1).EQ.0..AND.AR(2).EQ.0.) GO TO 330
      IF(BR(1).EQ.0..AND.BR(2).EQ.0.) GO TO 332
      IF(GR(1).EQ.0..AND.GR(2).EQ.0.) GO TO 334
      GO TO 336
330   PA=0.
      PB=DATAN2(BR(1),BR(2))/T
      PG=DATAN2(GR(1),GR(2))/T
      GO TO 340
332   PB=0.
      PA=DATAN2(AR(1),AR(2))/T
      PG=DATAN2(GR(1),GR(2))/T
      GO TO 340
334   PG=0.
      PA=DATAN2(AR(1),AR(2))/T
      PB=DATAN2(BR(1),BR(2))/T
      GO TO 340
336   PA=DATAN2(AR(1),AR(2))/T
      PB=DATAN2(BR(1),BR(2))/T
```

```
221          PG=DATAN2(GR(1),GR(2))/T
222       340 IF(PA.LT.0.) PA=360.+PA
223          IF(PB.LT.0.) PB=360.+PB
224          IF(PG.LT.0.) PG=360.+PG
225          PB11=(C2-C1)
226          PB12=(C3-C2)
227          PB13=(C3-C1)
228          WRITE(6,350)
229       350 FORMAT(8X,3HRHO,8X,3HPHI,12X,1HN,6X,13HBIREFRINGENCE)
230          WRITE(6,355)RA,PA,C1,PB11,RB,PB,C2,PB12,RG,PG,C3,PB13,W
231       355 FORMAT(1X,'A',3F12.5,3X,'(B-A) = ',F7.5/,1X,'B',3F12.5,3X,
232         1'(G-B) = ',F7.5/,1X,'G',3F12.5,3X,'(G-A) = ',F7.5/,'2V=',F12.5//)
233          PHI=PA-180.
234          IF(PHI.LT.0.) PHI=360.+PHI
235          THETA=RA
236          PSI=0.
237          IF(RA.EQ.0.) GO TO 360
238          CSP=(DCOS(RB*T)/DSIN(RA*T))/T
239          IF(CSP.GT.1.0) CSP=1.0
240          PSI=DARSIN(CSP)
241       360 WRITE(6,362)THETA,PHI,PSI
242       362 FORMAT(' EULER ANGLES OF INDICATRIX '/,3X,'THETA=',F10.5,'PHI=',
243         1F10.5,'PSI=',F10.5)
244          DO 370 I=1,3
245          AA(I)=AR(I)*DSIN(VV/2.)+GR(I)*DCOS(VV/2.)
246       370 BB(I)=-AR(I)*DSIN(VV/2.)+GR(I)*DCOS(VV/2.)
247          PAA=DATAN2(AA(1),AA(2))/T
248          IF(PAA.LT.0.) PAA=360.+PAA
249          PBB=DATAN2(BB(1),BB(2))/T
250          IF(PBB.LT.0.) PBB=360.+PBB
251          RAA=DARCOS(AA(3))/T
252          RBB=DARCOS(BB(3))/T
253          IF(RAA.GT.90.) PAA=180.+PAA
254          IF(PAA.GT.360.) PAA=PAA-360.
255          IF(RAA.GT.90.) RAA=180.-RAA
256          IF(RBB.GT.90.) PBB=180.+PBB
257          IF(PBB.GT.360.) PBB=PBB-360.
258          IF(RBB.GT.90.) RBB=180.-RBB
259          WRITE(6,380)RAA,PAA,RBB,PBB
260       380 FORMAT(' GOLDSCHMIDT ANGLES OF OPTIC AXES   RHO(1),PHI(1),RHO(2),A
261         1ND PHI(2)',10X,4F10.5)
262          IF(RN.GT.0..AND.PN.GT.0.) WRITE(6,390)RN,PN
263       390 FORMAT(' GOLDSCHMIDT ANGLES OF VECTOR NORMAL TO INTERFACE    RHO A
264         1ND PHI',13X,2F10.5)
265          GO TO 100
266          END
267          SUBROUTINEEA06C(A,VALUE,VECTOR,M,IA,IV,W)
268       C###### 18/05/70 LAST LIBRARY UPDATE
269          REAL*8A(IA,M),VALUE(M),VECTOR(IV,M),W(1)
270          M1=M+1
271          W(1)=A(1,1)
272          IF(M-2)60,10,15
273       10     W(2)=A(2,2)
274          W(4)=A(2,1)
275          GOTO60
```

```
277    15     CALLMC04B(A,W,W(M1),M,IA,W(M+M1))
278       60 CALLEA08C(W,W(M1),VALUE,VECTOR,M,IV,W(M+M1))
279          IF(M.LE.2)RETURN
280          DO56L=1,M
281          DO56I1=3,M
282          I=M-I1+1
283          IF(W(M1+I))57,56,57
284    57    PP=0.
285          I1=I+1
286          DO58K=I1,M
287    58    PP=PP+A(I,K)*VECTOR(K,L)
288          PP=PP/(A(I,I+1)*W(M1+I))
289          DO59K=I1,M
290    59    VECTOR(K,L)=VECTOR(K,L)+PP*A(I,K)
291    56    CONTINUE
292          RETURN
293          END
294          SUBROUTINEMC04B(A,ALPHA,BETA,M,IA,Q)
295    C###### 27/03/72 LAST LIBRARY UPDATE
296          IMPLICIT REAL*8(A-H,O-Z)
297          DIMENSIONA(IA,1),ALPHA(1),BETA(1),Q(1)
298          ALPHA(1)=A(1,1)
299          DO21J=2,M
300          J1=J-1
301          DO22I=1,J1
302          A(I,J)=A(J,I)
303    22    CONTINUE
304          ALPHA(J)=A(J,J)
305    21    CONTINUE
306          M1=M-1
307          M2=M-2
308          DO1I=1,M2
309          PP=0.0
310          I1=I+1
311          DO2J=I1,M
312          PP=PP+A(I,J)**2
313    2     CONTINUE
314          PP1=DSQRT(PP)
315          IF(A(I,I+1))3,5,5
316    5     BETA(I+1)=-PP1
317          GOTO6
318    3     BETA(I+1)=PP1
319    6     IF(PP)1,1,17
320    17    H=PP-BETA(I+1)*A(I,I+1)
321          A(I,I+1)=A(I,I+1)-BETA(I+1)
322          DO7KI=I1,M
323          QJ=0.0
324          DO8KJ=I1,KI
325          QJ=QJ+A(KJ,KI)*A(I,KJ)
326    8     CONTINUE
327          IF(KI-M)19,20,20
328    19    I2=KI+1
329          DO18KJ=I2,M
330          QJ=QJ+A(KI,KJ)*A(I,KJ)
331    18    CONTINUE
```

```
333   20      Q(KI)=QJ/H
334   7       CONTINUE
335           BIGK=0.0
336           DO9KJ=I1,M
337           BIGK=BIGK+A(I,KJ)*Q(KJ)
338   9       CONTINUE
339           BIGK=BIGK/(2.0*H)
340           DO10KJ=I1,M
341           Q(KJ)=Q(KJ)-BIGK*A(I,KJ)
342   10      CONTINUE
343           DO11KI=I1,M
344           DO12KJ=KI,M
345           A(KI,KJ)=A(KI,KJ)-Q(KI)*A(I,KJ)-Q(KJ)*A(I,KI)
346   12      CONTINUE
347   11      CONTINUE
348   1       CONTINUE
349           DO23I=2,M
350           H=ALPHA(I)
351           ALPHA(I)=A(I,I)
352           A(I,I)=H
353   23      CONTINUE
354           BETA(M)=A(M-1,M)
355           RETURN
356           END
357           SUBROUTINEEA08C(A,B,VALUE,VEC,M,IV,W)
358   C###### 12/01/76 LAST LIBRARY UPDATE
359           IMPLICIT REAL*8(A-H,O-Z)
360           REAL*8A(M),B(M),VALUE(M),VEC(1),W(1)
361           REALEPS/5.E-7/,A34/0./
362   C       THIS USES QR ITERATION TO FIND THE EIGENVALUES AND EIGENVECTORS
363   C   OF THE SYMMETRIC TRIDIAGONAL MATRIX WHOSE DIAGONAL ELEMENTS ARE
364   C   A(I),I=1,M AND OFF-DIAGONAL ELEMENTS ARE B(I),I=2,M.  THE ARRAY
365   C   W IS USED FOR WORKSPACE AND MUST HAVE DIMENSION AT LEAST 2*M.
366   C   WE TREAT VEC AS IF IT HAD DIMENSIONS (IV,M).
367           CALLEA09C(A,B,W(M+1),M,W)
368   C       SET VEC TO THE IDENTITY MATRIX.
369           DO5I=1,M
370           VALUE(I)=A(I)
371           W(I)=B(I)
372           K=(I-1)*IV+1
373           L=K+M-1
374           DO3J=K,L
375   3       VEC(J)=0.
376   5       VEC(K+I-1)=1.
377           K=0
378           IF(M.EQ.1)RETURN
379           DO200N3=2,M
380           N2=M+2-N3
381   C       EACH QR ITERATION IS PERFORMED OF ROWS AND COLUMNS N1 TO N2
382           ROOT=W(M+N2)
383           DO190ITER=1,20
384           BB=(VALUE(N2)-VALUE(N2-1))*0.5
385           CC=W(N2)*W(N2)
386           A22=VALUE(N2)
387           IF(CC.NE.0.0)A22=A22+CC/(BB+(1.0/BB)*BB*DSQRT(BB*BB+CC))
```

```
      DO125I=1,N2
      IF(DABS(ROOT-A22).LE.DABS(W(M+I)-A22))GOTO125
      ROOT=W(M+I)
      W(M+I)=W(M+N2)
      W(M+N2)=ROOT
  125 CONTINUE
      DO130II=2,N2
      N1=2+N2-II
      IF(DABS(W(N1)).LE.(DABS(VALUE(N1-1))+DABS(VALUE(N1)))*EPS)GOTO140
  130 CONTINUE
      N1=1
  140 IF(N2.EQ.N1)GOTO200
      N2M1=N2-1
      IF(ITER.GE.3)ROOT=A22
      K=K+1
      A22=VALUE(N1)
      A12=A22-ROOT
      A23=W(N1+1)
      A13=A23
      DO180I=N1,N2M1
      A33=VALUE(I+1)
      IF(I.NE.N2M1)A34=W(I+2)
      ZZ=DSQRT(A12*A12+A13*A13)
      IF(A12.EQ.0.) GO TO 333
      S=(A12*ZZ)/A12
      IF(S.NE.0.) GO TO 332
  333 CONTINUE
      S=1.0
  332 SI=A13/S
      CO=A12/S
      JK=I*IV+1
      J1=JK-IV
      J2=J1+MINO(M,I+K)-1
      DO160JI=J1,J2
      V1=VEC(JI)
      V2=VEC(JK)
      VEC(JI)=V1*CO+V2*SI
      VEC(JK)=V2*CO-V1*SI
  160 JK=JK+1
      IF(I.NE.N1)W(I)=S
      A11=CO*A22+SI*A23
      A12=CO*A23+SI*A33
      A13=SI*A34
      A21=CO*A23-SI*A22
      A22=CO*A33-SI*A23
      A23=CO*A34
      VALUE(I)=A11*CO+A12*SI
      A12=-A11*SI+A12*CO
      W(I+1)=A12
  180 A22=A22*CO-A21*SI
  190 VALUE(N2)=A22
      WRITE(6,195)
  195 FORMAT(48H1CYCLE DETECTED IN SUBROUTINE EA08 -STOPPING NOW)
      STOP
  200 CONTINUE
```

```
445   C      RAYLEIGH QUOTIENT
446          DO220J=1,M
447          K=(J-1)*IV
448          XX=VEC(K+1)**2
449          XAX=XX*A(1)
450          DO210I=2,M
451          XX=XX+VEC(K+I)**2
452   210    XAX=XAX+VEC(K+I)*(2.*B(I)*VEC(K+I-1)+A(I)*VEC(K+I))
453   220    VALUE(J)=XAX/XX
454          RETURN
455          END
456          SUBROUTINEEA09C(A,B,VALUE,M,OFF)
457          IMPLICIT REAL*8(A-H,O-Z)
458   C###### 16/12/75 LAST LIBRARY UPDATE
459          REAL*8A(M),B(M),VALUE(M),OFF(M)
460          REALA34/0./,EPS/5.0E-7/
461          VALUE(1)=A(1)
462          IF(M.EQ.1)RETURN
463          DO10I=2,M
464          VALUE(I)=A(I)
465   10     OFF(I)=B(I)
466   C      EACH QR ITERATION IS PERFORMED OF ROWS AND COLUMNS N1 TO N2
467          MAXIT=10*M
468          DO90ITER=1,MAXIT
469          DO45N3=2,M
470          N2=M+2-N3
471          DO30II=2,N2
472          N1=2+N2-II
473          IF(DABS(OFF(N1)).LE.(DABS(VALUE(N1-1))+DABS(VALUE(N1)))*EPS)GOTO40
474   30     CONTINUE
475          N1=1
476   40     IF(N2.NE.N1)GOTO50
477   45     CONTINUE
478          RETURN
479   C      ROOT  IS THE EIGENVALUE OF THE BOTTOM 2*2 MATRIX THAT IS NEAREST
480   C      TO THE LAST MATRIX ELEMENT AND IS USED TO ACCELERATE THE
481   C      CONVERGENCE
482   50     BB=(VALUE(N2)-VALUE(N2-1))*0.5
483          CC=OFF(N2)*OFF(N2)
484          SBB=1.
485          IF(BB.LT.0.)SBB=-1.
486          ROOT=VALUE(N2)+CC/(BB+SBB*DSQRT(BB*BB+CC))
487          N2M1=N2-1
488   75     A22=VALUE(N1)
489          A12=A22-ROOT
490          A23=OFF(N1+1)
491          A13=A23
492          DO80I=N1,N2M1
493          A33=VALUE(I+1)
494          IF(I.NE.N2M1)A34=OFF(I+2)
495          S=DSQRT(A12*A12+A13*A13)
496          SI=A13/S
497          CO=A12/S
498          IF(I.NE.N1)OFF(I)=S
499          A11=CO*A22+SI*A23
```

```
501           A12=CO*A23+SI*A33
502           A13=SI*A34
503           A21=CO*A23-SI*A22
504           A22=CO*A33-SI*A23
505           A23=CO*A34
506           VALUE(I)=A11*CO+A12*SI
507           A12=-A11*SI+A12*CO
508           OFF(I+1)=A12
509    80     A22=A22*CO-A21*SI
510    90     VALUE(N2)=A22
511           WRITE(6,100)
512      100  FORMAT(39H1LOOPING DETECTED IN EA09-STOPPING NOW )
513           STOP
514           END
```

APPENDIX B

THE DERIVATION OF THE EQUATIONS FOR THE DETERMINATION OF THE VOLUME FRACTIONS OF MULTIDIRECTIONAL INTERGROWTHS

Introduction

The equations to be derived in this appendix are used to determine the volume fraction (percentage of the total volume) of the host domain, H, and of those twin domains, T, that may occur within a composite crystal of zinc sulfide. The twin axes are parallel to <111> directions within the host sphalerite. The basic assumption made in this derivation is that the ratio of the intensities of two diffraction maxima is an approximate measure of the ratio of the volume fractions of the domains contributing to the intensity of the diffraction maxima.

If we let H be the volume fraction of the host domain (domain with the largest volume fraction) and T_i be the volume fraction of the "ith" twin domain, then the ratio of the volume fraction of a twin domain to the sum of the twin volume fraction plus the host volume fraction is:

$$\frac{T_i}{T_i + H} \quad . \qquad \text{(B-1)}$$

If we let g_i be the intensity of a 111 type reflection which is the result of diffraction from a twin volume fraction, T_i, only; and if h_i represents the intensity of a 111 type reflection along the twin axis which is the result of diffraction from the twin volume fraction and the

host volume fraction; then

$$\frac{g_i}{h_i} = \frac{T_i}{T_i + H} = K_i \quad ,$$

because the domains have essentially the same chemical composition and short range crystal structure.

The sum of the host volume fraction and the twin volume fractions will equal one,

$$H + \Sigma T_i = 1.$$

Therefore,

$$H + T_i = 1 - \Sigma T_{j \neq i} \quad . \tag{B-2}$$

This implies that H can be eliminated from (B-1) by substituting (B-2),

$$\frac{T_i}{T_i + H} = \frac{T_i}{1 - \Sigma T_{j \neq i}} = K_i \quad . \tag{B-3}$$

This implies that $T_i = K_i - K_i \Sigma T_{j \neq i}$,

which implies $T_i + K_i \Sigma T_{j \neq i} = K_i$. (B-4)

In the case of the zinc sulfides twinning may occur along four symmetry equivalent <111> directions creating a possibility of four

different twin domains. Applying equation (B-4) to this case:

$$T_1 + K_1T_2 + K_1T_3 + K_1T_4 = K_1 \qquad \text{(B-5)}$$

$$K_2T_1 + T_2 + K_2T_3 + K_2T_4 = K_2 \qquad \text{(B-6)}$$

$$K_3T_1 + K_3T_2 + T_3 + K_3T_4 = K_3 \qquad \text{(B-7)}$$

$$K_4T_1 + K_4T_2 + K_4T_3 + T_4 = K_4, \qquad \text{(B-8)}$$

four simultaneous equations obtain which can be solved for T_1, T_2, T_3, and T_4 in terms of K_1, K_2, K_3, and K_4 which can be determined from the intensity measurements.

For example, to determine the volume fraction, T_1, the four simultaneous equations could be solved to obtain

$$T_1 = \frac{K_1 - K_1K4}{[(1 - K1K4) - \underline{K3(1 - K4)(1 - K1)} - \underline{K2(1 - K4)(1 - K1)}]}, \qquad (K3 - 1) \qquad (K2 - 1)$$

which is expressed in terms of measureable quantities.

The vita has been removed from the scanned document